



Technische  
Universität  
Braunschweig

Master Thesis

# Data-Driven Turbulence Modeling for Correcting Unsteady Transonic Predictions

Henrik Lange  
Matriculation Number 5331730

First Examiner: **Prof. Dr. Stefan Görtz**  
Institute of Aircraft Design and Lightweight Structures  
Technische Universität Braunschweig  
*and*  
Institute of Aerodynamics and Flow Technology  
German Aerospace Center (DLR)

Second Examiner: **Prof. Dr.-Ing. Lorenz Tichy**  
Institute of Aircraft Design and Lightweight Structures  
Technische Universität Braunschweig  
*and*  
Institute of Aeroelasticity  
German Aerospace Center (DLR)

Scientific Supervisor: **Dr. Philipp Bekemeyer**  
Institute of Aerodynamics and Flow Technology  
German Aerospace Center (DLR)

Published: **September 2024**

DLR e. V. Institut für Aerodynamik und Strömungstechnik  
Lilienthalplatz 7, 38108 Braunschweig

Ihr Gesprächspartner Prof. Dr. S. Görtz

Telefon 0531  
Telefax 0531 295-3357  
E-Mail stefan.goertz@dlr.de

18 March 2024

## Description of Master Thesis

### Data-Driven Turbulence Modeling for Correcting Unsteady Transonic Predictions

**Student Name:** Henrik Lange  
**Enrollment number:** 5331730  
**Duration:** 18.03.2024 – 18.09.2024  
**First Examiner:** Prof. Dr. Stefan Görtz  
**Second Examiner:** Prof. Dr. Lorenz Tichy  
**Scientific Supervisor:** Dr. Philipp Bekemeyer

When comparing aerodynamic data (pressure measurements, lift/moment per spanwise station) from flight tests to theoretical/numerical models, deviations can be observed. One of the sources that can cause such differences is the turbulence model employed when solving the Reynolds-Averaged Navier-Stokes (RANS) equations. Recently, several pathways have been proposed to adopt and enhance turbulence models once measured data (e.g. from flight test or wind tunnel investigations) is available. One of these pathways is the so-called Field Inversion and Machine Learning (FIML) approach. The idea of this approach is to introduce a local correction factor to the turbulence model production term that can be obtained by solving an inverse problem, the so-called field inversion step, at a few operating points, e.g. at different angles of attack. Once such local correction sets are available as a function of Cartesian coordinates, a generalized model can be derived by relating local flow features to the corrections using machine learning methods. Previously, this method has been successfully employed at DLR to improve results at subsonic flow conditions with a special focus on cases featuring trailing edge separation due to adverse pressure gradients. The aim of this thesis is to investigate if this methodology is capable of correcting turbulence models such that improved predictions at steady transonic flow conditions including shocks are obtained, and how this affects a subsequent unsteady response analysis. The ambition is to define representative transonic cases for which numerical and experimental (or synthetic higher fidelity) data is available together with unsteady information to answer the abovementioned research question. Results should be compared to responses without turbulence model correction and potentially also to linearized frequency domain solutions. Models that have been trained for one test case should be used for a similar test case or the same test case but for different flow conditions to check how the corrected model generalizes.

Moreover, it is to be investigated, at what level of unsteadiness the correction that was learned based on steady data fails, requiring an unsteady correction procedure.

Description of Work	Duration in weeks
Review of data-driven turbulence modeling techniques with a focus on the Field Inversion and Machine Learning (FIML) approach	2
Familiarization with existing FIML capabilities in the DLR SMARTy package	3
Definition and initial investigation of at a representative use case	2
Obtaining correction fields using the FI step for several selected operating conditions and evaluation of accuracy improvements	3
Trainings of machine learning models to generalize the correction fields including selection of appropriate flow features	4
Unsteady response analysis with and without FIML enhanced turbulence model with comparison to reference data	5
Extension to larger-scale application case to investigate scalability (optional depending on initial investigations)	4
Writing of master thesis	3
<b>Sum</b>	<b>26</b>

Prof. Dr. Stefan Görtz

# Declaration of Independence

I hereby declare, that I am the sole author and composer of my thesis and that no other sources or learning aids, other than those listed, have been used. Furthermore, I declare that I have acknowledged the work of others by providing detailed references of said work. I also hereby declare that my thesis has not been prepared for another examination or assignment, either in its entirety or excerpts thereof.

A handwritten signature in blue ink that reads "Henrik Lange". The signature is written in a cursive style and is positioned above a horizontal line.

---

Braunschweig, 18<sup>th</sup> September 2024

# Abstract

Numerical simulations with high accuracy are a fundamental part of modern aircraft design. The current industry standard for the simulation of aerodynamic flows are RANS simulations that require modeling of unresolved turbulence. The underlying assumptions of RANS equations and the corresponding turbulence models exhibit inadequacies that lead to errors. *Field inversion and machine learning* (FIML) is a data-driven turbulence modeling approach that introduces a spatially varying correction term in the turbulence model by using high-fidelity numerical or experimental reference data. Within this thesis the production term of the negative Spalart-Allmaras (SA) model is corrected.

Using the RAE 2822 two-dimensional airfoil two test cases, one with numerical and one with experimental reference data, are designed to incorporate transonic flow effects such as shocks. The FIML approach is trained and applied on multiple steady cases with varying angles of attack  $\alpha$ , aiming to yield good corrections for steady transonic simulations and implicitly learning the change of the correction field  $\beta$  with the angle of attack  $d\beta/d\alpha$ . In a second step, the trained model is applied to unsteady dual-time stepping simulations with a pitching airfoil at varying reduced frequencies and excitation amplitudes.

The field inversion approach delivers good corrections of the reference quantity and related quantities for inadequacies caused by the SA turbulence model in transonic flow fields including shocks using a realistic number of reference points. Therefore, investigations regarding the number of reference points, the correction of non-reference variables, and varying free-stream conditions are conducted.

Applying a fully-connected neural network with selected locally available flow features to a limited area of the flow field yields good results for the correction of steady simulations. For the application to unsteady simulations, the ML correction model shows ambiguous results regarding the accuracy and convergence issues for flow conditions including strong non-linear effects. Applying a steady correction field which is the result of the field inversion or a corrected steady simulation yields improved convergence and promising correction results at excitation amplitudes smaller than one degree. Testing the ML approach on the second test case with experimental reference data shows issues regarding generalizability. Finally, multiple ideas regarding further work and improvements are presented.

# Kurzfassung

Numerische Simulationen mit hoher Genauigkeit sind ein wichtiger Bestandteil im heutigen Flugzeugentwurf. Industrieller Standard ist die Verwendung von Simulationen basierend auf den RANS Gleichungen. Dafür ist eine Modellierung nicht aufgelöster Turbulenz notwendig. Die den RANS Gleichungen und den dazugehörigen Turbulenzmodellen zugrundeliegenden Annahmen weisen Ungenauigkeiten auf und führen zu Fehlern. Der datengetriebene Turbulenzmodellierungsansatz *Field Inversion and Machine Learning* (FIML) führt einen räumlich variierenden Korrekturterm im Turbulenzmodell ein, indem höherwertige numerische Simulationen oder experimentelle Daten genutzt werden. Innerhalb dieser Arbeit wird der Produktionsterm des negativen Spalart-Allamaras (SA) Turbulenzmodells korrigiert.

Zwei Testfälle, einer mit numerischen und einer mit experimentellen Referenzdaten, basierend auf dem RAE 2822 Flügelprofil sind so ausgelegt, dass transonische Strömungseffekte inklusive Stößen enthalten sind. FIML wird verwendet um eine Korrektur von stationären transonischen Strömungen bei variierendem Anstellwinkel  $\alpha$  zu ermöglichen. Dabei soll implizit die Änderung des Korrekturfaktors  $\beta$  mit dem Anstellwinkel  $d\beta/d\alpha$  gelernt werden. In einem zweiten Schritt wird das trainierte Modell zur Korrektur instationärer *dual-time stepping* Simulationen mit einem harmonisch nickenden Profil bei verschiedenen reduzierten Frequenzen und Amplituden verwendet.

Mit einer realistischen Anzahl an Referenzpunkten liefert die Feldinversion gute Korrekturergebnisse in transonischer Strömung bezüglich der Referenzgrößen und verwandter Größen für Fehler die durch das Turbulenzmodell verursacht werden. Dafür werden Untersuchungen bezüglich der Anzahl der Referenzpunkt, des Einflusses der Korrektur auf verschiedene Variablen und des Verhaltens bei Fehlern in den Anströmbedingungen durchgeführt.

Unter Verwendung eines vollvernetzten neuronalen Netzwerkes mit ausgewählten lokal verfügbaren Eingangsgrößen in einem beschränkten Bereich des Strömungsfelds können gute Korrekturergebnisse für stationäre Simulationen erzielt werden. Die Anwendung selbigen Korrekturmodells in instationären Simulationen liefert uneindeutige Ergebnisse bezüglich der Genauigkeit und weist zudem Konvergenzprobleme auf, wenn ausgeprägte nichtlineare Effekte vorhanden sind. Eine Korrektur instationärer Simulationen mithilfe von stationären Korrekturfeldern, welche das Ergebnis der Feldinversion oder stationärer korrigierter Simulation sind, zeigt bessere Ergebnisse hinsichtlich Genauigkeit und Konvergenz für Amplituden bis zu einem Grad. Angewendet auf den zweiten, experimentellen Testfall zeigt das trainierte Korrekturmodell Probleme hinsichtlich der Generalisierbarkeit. Schlussendlich werden Ideen zu Verbesserungsmöglichkeiten und weiteren Untersuchungen aufgezeigt.

# Contents

<b>Nomenclature</b>	<b>vii</b>
<b>1 Introduction</b>	<b>1</b>
1.1 Related Work . . . . .	2
1.2 Research Objective . . . . .	3
1.3 Outline . . . . .	4
<b>2 Problem Background</b>	<b>5</b>
2.1 Transonic Flows . . . . .	5
2.2 Unsteady Flows . . . . .	6
2.3 RANS Equations . . . . .	7
2.4 Turbulence Modeling . . . . .	8
2.5 Resulting Task . . . . .	11
<b>3 Field Inversion and Machine Learning</b>	<b>12</b>
3.1 Idea . . . . .	12
3.2 FIML Classic . . . . .	12
3.3 Field Inversion . . . . .	13
3.4 Machine Learning . . . . .	14
3.5 Application of Correction Model . . . . .	17
3.6 Current Implementations . . . . .	18
<b>4 Numerical Test Case</b>	<b>19</b>
4.1 Case Description and Preparation . . . . .	19
4.2 Field Inversion on Steady Simulations . . . . .	23
4.3 Machine Learning . . . . .	33
4.4 Application to Steady Simulations . . . . .	44
4.5 Unsteady Case Description and Preparation . . . . .	46
4.6 Correction of Unsteady Simulations . . . . .	50
4.7 Findings . . . . .	58
<b>5 Experimental Test Case</b>	<b>60</b>
5.1 Case Description and Preparation . . . . .	60
5.2 Field Inversion . . . . .	63
5.3 Machine Learning and Application to Steady Simulation . . . . .	65
5.4 Exemplary Unsteady Simulation . . . . .	69
5.5 Findings . . . . .	69
<b>6 Conclusions and Outlook</b>	<b>71</b>
6.1 Conclusions . . . . .	71
6.2 Outlook . . . . .	73
<b>Bibliography</b>	<b>80</b>
<b>List of Figures</b>	<b>83</b>
<b>List of Tables</b>	<b>84</b>
<b>A Appendix</b>	<b>85</b>

# Nomenclature

## Latin

$b$	Bias
$\mathbf{b}$	Bias vector
$c$	Chord length
$c_d$	Drag coefficient
$c_f$	Skin friction coefficient
$c_l$	Lift coefficient
$c_{my}$	Pitching moment coefficient
$c_p$	Pressure coefficient
$c_{z,\text{inertial}}$	Coefficient of force in inertial z-direction
$D$	Turbulence model destruction term
$e$	Thermodynamic internal energy
$f$	Frequency
$f(\cdot)$	Functional relationship
$\mathbf{f}$	Body force vector
$g(\cdot)$	Activation function
$\mathbf{h}$	Hidden layer
$\mathbf{I}$	Identity matrix
$\mathcal{I}$	Cost function
$k$	Reduced frequency
$\tilde{k}$	Heat conduction coefficient
$\mathbf{k}$	Turbulent kinetic energy vector
$l$	Length
$M$	MACH number
$\tilde{M}$	Number of reference data points
$n$	Amount of substance
$N$	Number of cells
$\mathbf{o}$	Generic vector
$p$	Pressure
$P$	Turbulence model production term
$q$	Reference value
$Q$	Heat source
$r$	Correlation coefficient
$R$	Ideal gas constant
$\mathbf{R}$	REYNOLDS stress tensor
$R^2$	Coefficient of determination
$Re$	REYNOLDS number
$\mathbf{S}$	Strain rate tensor
$t$	Time

$T$	Temperature
$\mathbf{u}$	Velocity vector
$\bar{\mathbf{u}}$	Mean part of velocity vector
$\mathbf{u}'$	Fluctuating part of velocity vector
$\mathbf{U}$	Mean flow variables
$V$	Volume
$\mathbf{w}$	Weight vector
$\mathbf{W}$	Weight matrix
$x$	Cartesian coordinate in x-direction (corresponding to the aircraft roll axis)
$\mathbf{x}$	Cartesian coordinate vector
$y$	Cartesian coordinate in y-direction (corresponding to the aircraft pitch axis)
$z$	Cartesian coordinate in z-direction (corresponding to the aircraft yaw axis)

## Greek

$\alpha$	Angle of attack
$\bar{\alpha}$	Mean angle of attack
$\beta$	Correction term
$\eta$	Feature
$\theta$	Pitch angle
$\hat{\theta}$	Pitch amplitude
$\lambda$	Regularization parameter
$\nu$	Kinematic viscosity
$\nu_t$	Turbulent kinematic viscosity
$\mu_t$	Dynamic eddy viscosity
$\tilde{\nu}$	Spalart-Allmaras viscosity
$\rho$	Density
$\boldsymbol{\tau}$	Deviatoric stress tensor
$\varphi$	Generic flow variable
$\bar{\varphi}$	Mean component of generic flow variable
$\varphi'$	Fluctuating component of generic flow variable
$\phi$	Radial basis function
$\chi$	Dimensionless Spalart-Allmaras viscosity
$\Omega$	Vorticity

## Indices

0	equilibrium
$\infty$	free-stream
crit	critical
max	maximum
opt	optimal
ref	reference
tot	total

## Abbreviations

AI	<u>A</u> rtificial <u>I</u> ntelligence
CFD	<u>C</u> omputational <u>F</u> luid <u>D</u> ynamics
CFL	<u>C</u> OURANT- <u>F</u> RIEDRICHS- <u>L</u> EWY
DL	<u>D</u> eep <u>L</u> earning
DLR	<u>D</u> eutsches Zentrum für <u>L</u> uft- und <u>R</u> aumfahrt (German Aerospace Center)
DNS	<u>D</u> irect <u>N</u> umerical <u>S</u> imulation
FCNN	<u>F</u> ully- <u>C</u> onected <u>N</u> eural <u>N</u> etwork
FFT	<u>F</u> ast <u>F</u> OURIER <u>T</u> ransform
FI	<u>F</u> ield <u>I</u> nversion
FIML	<u>F</u> ield <u>I</u> nversion and <u>M</u> achine <u>L</u> earning
FRF	<u>F</u> requency <u>R</u> esponse <u>F</u> unction
HPO	<u>H</u> yper <u>P</u> arameter <u>O</u> ptimization
LES	<u>L</u> arge <u>E</u> ddy <u>S</u> imulation
MAE	<u>M</u> ean <u>A</u> bsolute <u>E</u> rror
ML	<u>M</u> achine <u>L</u> earning
MLP	<u>M</u> ulti- <u>L</u> ayer <u>P</u> erceptron
MSE	<u>M</u> ean <u>S</u> quared <u>E</u> rror
RANS	<u>R</u> EYNOLDS- <u>a</u> veraged <u>N</u> AVIER- <u>S</u> TOKES
RBF	<u>R</u> adial <u>B</u> asis <u>F</u> unction
RSM	<u>R</u> EYNOLDS <u>S</u> tress <u>M</u> odel
SA	<u>S</u> PALART- <u>A</u> LLMARAS
SA-neg	<u>N</u> egative <u>S</u> PALART- <u>A</u> LLMARAS
SMARTy	<u>S</u> urrogate <u>M</u> odeling for <u>A</u> eRo data <u>T</u> oolbox in <u>P</u> ython
SWBLI	<u>S</u> hock <u>W</u> ave <u>B</u> oundary <u>L</u> ayer <u>I</u> nteraction
PDE	<u>P</u> artial <u>D</u> ifferential <u>E</u> quation

# Chapter 1

## Introduction

Future aircraft design of new, disruptive layouts, aims to incorporate processes such as certification by analysis and virtual flight testing to reduce the number and the cost of physical tests such as wind tunnel or flight tests. Thus, numerical tools with high accuracy across the entire flight envelope are required [1]. Even though numerous future aircraft concepts aim to achieve laminar flow to reduce drag, most commercial aircraft that fly at high REYNOLDS numbers are subjected to turbulent flows. When flying at typical cruise speeds in the transonic regime, the flow is significantly influenced by shocks. An accurate prediction of the interaction between shocks and other flow phenomena, e.g. the boundary layer, is mandatory to ensure a safe and efficient flight. Steady-state simulations are sufficient to analyse a variety of flight conditions, e.g. cruise. In addition, time-dependent flows must be considered in the aeroelastic analysis or when an aircraft is subjected to gusts [2]. This requires accurate simulations of unsteady aerodynamics.

A straightforward solution to numerically compute turbulent flows is to resolve the governing equations at all spatial and temporal scales, using direct numerical simulation (DNS). However, being computationally very expensive with current resources DNS is unfeasible to be applied to industrial problems. Compared to DNS, large eddy simulations (LES) and methods based on REYNOLDS-averaged NAVIER-STOKES (RANS) equations are of lower fidelity, as they do not resolve the flow at all scales and are therefore computationally less expensive [3, 4]. Both approaches decompose the flow into a resolved and an unresolved part: LES filters the physical scales while the RANS approach separates the flow into mean and fluctuating components. LES is of higher fidelity, however, still computationally too expensive to be applied to industrial problems. For most industrial applications, solving the RANS equations is the highest fidelity approach that is computationally feasible.

Turbulence models are necessary to achieve a closed form of the RANS equations and describe the relationship between the resolved mean flow and the unresolved fluctuating components. Each model relies on assumptions that might be empirical, mathematical, or based on physical considerations. A large variety of turbulence models with a wide range of complexity and different target applications is available. Regardless of the complexity, all models and the RANS approach itself exhibit inadequacies: information is lost by separating a flow into mean and fluctuating components, the modeling assumptions and the resulting functional relationships are imperfect, and lastly turbulence models are calibrated using canonical test cases that only reflect selected flow characteristics. Quantifying and mitigating the errors of turbulence models is necessary for the models to deliver reliable results across all flight conditions. Especially turbulence modeling for unsteady flow is less mature than steady RANS turbulence models. This area is identified as one technology gap that needs to be improved in future CFD codes [5].

The steady improvement of computational resources allows to processing of larger amounts of data, increasing the popularity of data-driven approaches such as machine learning

(ML). Experimental and numerical investigations in fluid dynamics research produce large amounts of data, making this field attractive for data-driven methodologies [6]. Parish and Duraisamy as well as Duraisamy *et al.* introduce the *field inversion and machine learning* (FIML) approach that makes use of available high fidelity data to improve existing turbulence models [7, 8]. Investigations of the FIML approach on steady aerodynamic problems show promising results as the literature review in the next section shows. Thus, an investigation regarding unsteady flows is of interest.

The text above gives a motivation for this thesis. Subsequently, related work is reviewed in section 1.1 before a research objective is defined in section 1.2. Finally, the structure of this work is outlined in section 1.3.

## 1.1 Related Work

Various data-driven turbulence modeling approaches are described in the literature. In this section, publications regarding general considerations and approaches are reviewed before papers concerning the FIML approach are considered.

In a review paper Brunton *et al.* give an overview of ML methods for fluid dynamics. The historical relationship between statistical learning methods and the physical problem of fluid dynamics, especially turbulence, is described. Recognizing underlying structures in complex data is a strength of ML models. Turbulence is characterised by complex structures that are hard to describe analytically. Thus, the paper argues that ML is suitable for turbulence closure modeling [6].

Multiple publications aim to employ data-driven approaches to replace (parts of) the RANS turbulence models. Ling and Templeton make a first step towards data-driven turbulence modeling by training different ML approaches on canonical test cases, comparing RANS solutions to corresponding higher fidelity solutions. The resulting models can classify, but not quantify regions of high uncertainty [9]. Wang *et al.* learn discrepancies in RANS modeled REYNOLDS stresses as a function of mean flow features using supervised ML techniques based on random forests [10]. This approach is extended by Wu *et al.* introducing a comprehensive framework that can predict mean flow velocities based on the ML predicted REYNOLDS stress tensor [11]. Instead of learning the entire REYNOLDS stresses, Ling *et al.* introduce a deep neural network with embedded physical properties to only predict the anisotropy tensor. Improvements over baseline turbulence models are achieved [12].

Data-driven turbulence modeling is not exclusive to the RANS approach. Gamahara and Hattori train an artificial neural network to establish a functional relationship between subgrid-scale stresses and grid-scale flow quantities in LES. Using DNS training data, the model can find functions with high correlation to existing models [13]. Similarly, Beck *et al.* introduce a rigorous framework to derive subgrid closure models using neural networks [14].

All of the previously mentioned publications aim to introduce a data-driven approach that can replace (parts of) a closure model. The FIML approach, first introduced by Parish and Duraisamy and further described by Duraisamy *et al.*, has the objective of correcting existing turbulence models instead of replacing them. Thus, physical considerations and constraints from the original closure models are preserved. In the first step, using statist-

ical inference methods, the so-called field inversion, a spatially distributed correction term is introduced into a RANS closure model by harnessing reference data from higher-fidelity simulations or experiments. Subsequently, the relationship between the correction term and mean flow variables is learned using ML methodologies [7, 8]. This approach is not fully data-driven, but data-informed: data is used to improve an existing model that is based on physical considerations. Multiple publications further investigate the FIML approach. Jäckel performs a sensitivity analysis with a focus on the field inversion (FI) step using the SPALART-ALLMARAS (SA) turbulence model. The influence of regularization, grid resolution, and a spatially restricted application of the approach is investigated [15]. Grabe *et al.* investigate the FIML on transonic flows including shock-induced separation. The work sets an emphasis on the selection of input features for the ML model and finds features that lead to improved outcomes [16].

Holland *et al.* argue that the two-step *FIML Classic* approach might exhibit an inconsistency between the correction that is derived in the FI step and the correction that is predicted by an imperfectly trained ML model. A physics-consistent one-step approach, also called *FIML Direct*, that integrates the ML model training within the inverse problem of the inference step is proposed and tested. The resulting approach shows improved results regarding the ability to generalize, however, with the cost of decreased numerical stability [17]. Jäckel implements the FIML Direct with the SA turbulence model and shows improved flow predictions on separated flows [18].

The available research on FIML for unsteady RANS simulations is limited. Fidkowski does not apply the FIML approach within unsteady simulations, however, a design optimization loop consisting of unsteady simulations, FIML and steady adjoint-based shape optimization is investigated. The proposed optimization accounts for unsteady effects and leads to an improvement in gradient-based shape optimization [19]. A recent publication by Fang and He develops a FIML framework for time-accurate unsteady flow. The authors propose to use a coupled FIML approach, similar to FIML Direct, to correct the flow within the inner loop of each physical time step of an unsteady time marching simulation based on time-dependent flow features. Improved results over the baseline SA-turbulence model, with the limitation of a computationally very challenging and expensive problem that involves a highly non-linear neural network model and a CFD solver, are observed [20].

## 1.2 Research Objective

The main research objective for this is given by the following quote from the description of the master thesis, which can be found in the front matter:

«The aim of this thesis is to investigate if this methodology is capable of correcting turbulence models such that improved predictions at steady transonic flow conditions including shocks are obtained and how this affects a subsequent unsteady response analysis.»

Following the task description and the main research objective, several sub-objectives may be stated:

- Correction fields for steady-state RANS simulations in the transonic regime are to be obtained using field inversion. The results must be evaluated.

- An investigation of ML approaches to predict correction fields based on mean flow quantities must be performed. This includes a feature selection and an evaluation regarding the generalizability.
- The correction model trained on steady data shall be applied to unsteady simulations. Different levels of unsteadiness must be investigated to determine the limitations of the approach.

While the first and second sub-objectives are not entirely new and build on existing publications, the author is not aware of any work similar to the third sub-objective. Thus, the investigation of the application of a FIML correction model trained on steady data to unsteady simulations is an extension of the current state of research.

## 1.3 Outline

This chapter gives motivation for this thesis and surveys related research. In chapter 2, the physical background to transonic and unsteady flows is described. Also, numerical approaches to solve the physical problems and the corresponding challenges are stated. Subsequently, in chapter 3, the FIML approach is described. Then, two test cases are investigated: in chapter 4 the FIML approach is investigated by using steady high-fidelity reference data and by applying the derived correction model to unsteady simulations. While the first test case contains several smaller investigations, the second test case in chapter 5 is narrower in scope. The findings from the first test case are tested using experimental reference data to evaluate the generalizability of the approach. Finally, the results are summarised, conclusions are drawn, and an outlook for further work is given in chapter 6.

# Chapter 2

## Problem Background

Two types of physical flow phenomena are of interest for this thesis: section 2.1 introduces transonic flows and section 2.2 introduces unsteady flows. Using the REYNOLDS-averaged NAVIER-STOKES (RANS) equations, given in section 2.3, in combination with a turbulence model, explained section 2.4, allows to compute the flow phenomena numerically. Section 2.5 reasons how inadequacies in the current computational approach relate to the objective of this thesis.

### 2.1 Transonic Flows

Transonic flows are a crucial physical phenomenon influencing aircraft design significantly and are introduced in subsection 2.1.1. Thus, understanding challenges in the computational simulation of transonic flows stated in subsection 2.1.2 is important.

#### 2.1.1 Physical Phenomena

Modern commercial aircraft typically fly at speeds close to, but below,  $M = 1$ . Above the airfoil-specific critical MACH number  $M_{\text{crit}}$ , the flow on the airfoil, typically on the upper side, is accelerated to  $M \geq 1$  even though the free-stream velocity is below the speed of sound. The supersonic flow is usually terminated by a shock wave which slows the flow to subsonic flow conditions. Said flow condition with regions of sub- and supersonic flow is referred to as transonic flow.

With increasing free-stream MACH number, the shock moves backwards on the airfoil. The shock may also move forward with an inverse shock motion. Additionally, a shock wave on the lower side of the airfoil may emerge. The shock wave results in an increase in static pressure and interacts with the boundary layer. With increasing MACH number, the shock gets stronger. It affects the boundary layer in a way that adverse pressure gradients and separation may occur if the boundary layer's kinetic energy is too small to withstand the shock. The interaction of the shock wave and the boundary is mutual and referred to as shock wave boundary layer interaction (SWBLI). In addition to separation, oscillations can occur [21, 22].

#### 2.1.2 Challenges in Computational Solution

As the position of the shock and the interaction with the boundary layer significantly influence quantities of interest such as lift, drag and pitching moment, correctly computing the phenomena is of great importance.

This poses a significant challenge since solving the mathematical problem of transonic flow is a non-linear problem corresponding to an elliptic mathematical problem in subsonic flow

and a hyperbolic problem in supersonic flow. Using CFD to solve the RANS equations, given in section 2.3, allows to make predictions on transonic flows [23].

The quality of transonic CFD computations is limited by the underlying assumptions of the equations. Particularly the chosen turbulence model exhibits restrictive assumptions and influences the result, as stated in section 2.4. As a baseline comparison and model to be corrected, the SPALART-ALLMARAS turbulence model is used in this thesis. This model is known to under-predict boundary layer separation, i.e. over-predict the turbulent kinetic energy in the boundary layer in some cases, affecting the shock position. Thus, it is desirable to correct the turbulence model to achieve more precise results.

## 2.2 Unsteady Flows

Unsteady aerodynamics occur when time-dependent processes are present in a flow. Understanding the physical phenomena and how to compute unsteady flows is described in the following sections.

### 2.2.1 Physical Phenomena

Unsteadiness in a flow may be caused by the motion of a body in the flow, e.g. a harmonically pitching airfoil, external disturbances such as gusts, or time-dependent interactions of flow phenomena, e.g. SWBLI. An interaction between multiple effects is also possible. The interaction of aerodynamic forces with a structure is the subject of investigation of aeroelasticity [24, 25].

This thesis investigates unsteady aerodynamics caused by the harmonic pitching motion of an airfoil. Given a mean angle of attack  $\bar{\alpha}$  the airfoil pitches with a harmonic frequency  $f$  and a pitch amplitude  $\hat{\theta}$  around a reference point at 1/4-th chord length. The resulting angle of attack is a function of time  $t$ :

$$\alpha(t) = \bar{\alpha} + \theta(t) = \bar{\alpha} + \hat{\theta} \cdot \sin(2\pi f \cdot t). \quad (2.1)$$

Introducing a dimensionless parameter, the reduced frequency  $k$ , allows a comparison of unsteady effects in different flow cases:

$$k = \frac{2\pi f l_{\text{ref}}}{|\mathbf{u}_{\infty}|}, \quad (2.2)$$

with  $f$  the harmonic frequency,  $l_{\text{ref}}$  a reference length, e.g. the chord length, and  $|\mathbf{u}_{\infty}|$  the free-stream velocity. Faster changes, i.e. larger reduced frequencies, may lead to a phase shift between the excitation and the response. For  $k \rightarrow 0$  the problem becomes quasi-steady [24].

### 2.2.2 Numerical Computation

Multiple methodologies are available to compute unsteady aerodynamics. The Doublet-Lattice method as introduced by Albano and Rodden assumes small perturbations and is a powerful method to predict unsteady aerodynamic forces in compressible, inviscid flow [26]. Since viscous effects are not covered by this method, effects such as shock waves, or boundary layer separation are not predicted correctly and require correction.

Using CFD methods based on the NAVIER-STOKES equations is computationally more expensive, but leads to more precise results. The unsteady computations in this thesis are done using the dual-time stepping method by Jameson that is implemented in the DLR-TAU code [27, 28, 29]. The dual time stepping method uses a backward differentiation scheme to solve the RANS equations for a subsequent time step. Each physical time step is treated as a steady state problem that is solved in *inner* iterations using a pseudo time variable and an implicit RUNGE-KUTTA. In contrast to an explicit scheme, the implicit scheme is numerically stable for arbitrarily large time steps. Thus, the time step size is only limited by accuracy requirements [27]. To be concise, the mathematical formulation is not reproduced in this thesis and can be found in the referenced publications.

## 2.3 RANS Equations

The NAVIER-STOKES equations describe the motion of viscous fluids and can be used to describe transonic and unsteady flows. These equations form a system of non-linear partial differential equations. Solving the equations in a discretised space is the subject of computational fluid dynamics (CFD). The following partial differential equations are derived based on finite control volumes fixed in space and fully describe a compressible fluid flow [4].

The conservation of mass in vector notation can be written as

$$\frac{\partial \rho}{\partial t} + \nabla \cdot (\rho \mathbf{u}) = 0 \quad (2.3)$$

where  $\rho$  is the density,  $t$  is the time,  $\nabla \cdot$  is the divergence operator, and  $\mathbf{u}$  is the vector of flow velocities.

Based on NEWTONS second law the conservation of momentum is given by the equation

$$\frac{\partial \rho \mathbf{u}}{\partial t} + \nabla \cdot (\rho \mathbf{u} \mathbf{u}) = -\nabla p + \nabla \cdot \boldsymbol{\tau} + \rho \mathbf{f} \quad (2.4)$$

with pressure  $p$ , the deviatoric stress tensor  $\boldsymbol{\tau}$ , and  $\mathbf{f}$  the body force vector.

Finally, the total energy equation is given by

$$\frac{\partial}{\partial t} \left[ \rho \left( e + \frac{1}{2} |\mathbf{u}|^2 \right) \right] + \nabla \cdot \left[ \rho \left( e + \frac{1}{2} |\mathbf{u}|^2 \right) \mathbf{u} \right] = \nabla \cdot (\tilde{k} \nabla T) + \nabla \cdot (-p \mathbf{u} + \boldsymbol{\tau} \cdot \mathbf{u}) + \rho \mathbf{u} \cdot \mathbf{f} + \mathcal{Q} \quad (2.5)$$

where  $e$  is the thermodynamic internal energy,  $\tilde{k}$  is the heat conduction coefficient,  $T$  is the temperature, and  $\mathcal{Q}$  is a heat source. The fluid flow is fully described, using equations 2.3–2.5 together with an equation of state as the ideal gas law that is stated in the subsequent formula:

$$pV = nRT \quad (2.6)$$

with  $V$  the volume,  $n$  the amount of substance, and  $R$  the ideal gas constant.

Solving the NAVIER-STOKES equations in discretised volumes that resolve all temporal and spatial scales yields a physically accurate solution. However, due to the large range of scales in a turbulent flow, this requires an enormous computational effort. By assuming a statistically stationary flow, the REYNOLDS decomposition can be applied to the flow

equations 2.3-2.5 [30]. A generic flow variable  $\varphi(\mathbf{x}, t)$  can be decomposed into a mean time-independent component  $\bar{\varphi}(\mathbf{x})$  and a fluctuating time-dependent component  $\varphi'(\mathbf{x}, t)$ :

$$\varphi(\mathbf{x}, t) = \bar{\varphi}(\mathbf{x}) + \varphi'(\mathbf{x}, t) \quad (2.7)$$

Applying the REYNOLDS decomposition to the momentum equation (eq. 2.4), while assuming a NEWTONIAN fluid and a constant density, results in the following mean flow momentum equation:

$$\frac{\partial \bar{\mathbf{u}}}{\partial t} + \nabla \cdot (\bar{\mathbf{u}}\bar{\mathbf{u}}) = -\nabla \bar{p} + \nabla \cdot (\nu (\nabla \bar{\mathbf{u}} + \nabla \bar{\mathbf{u}}^\top) - \overline{\mathbf{u}'\mathbf{u}'}) \quad (2.8)$$

where  $\nu$  is the kinematic viscosity. Equation 2.8 shows that the REYNOLDS stress tensor  $\mathbf{R} = -\overline{\mathbf{u}'\mathbf{u}'}$  needs to be defined. This closure problem is often referred to as turbulence modeling and is further described in section 2.4. To keep this thesis concise, a simple form of the REYNOLDS-averaged momentum equation is presented. More general forms, e.g. for compressible flows, can be found in the literature, e.g. [30].

## 2.4 Turbulence Modeling

Many approaches of different complexity, aiming to achieve a closed system of equations starting from the REYNOLDS-averaged NAVIER-STOKES (RANS) equations, are available and can be described in two different main categories. The first category is based on the BOUSSINESQ hypothesis, assuming the deviatoric part of the REYNOLDS stresses to be proportional to the mean rate of deformation [30]:

$$\mathbf{R} = \nu_t 2\mathbf{S} - \frac{2}{3}k\mathbf{I} \quad (2.9)$$

with  $\nu_t$  the turbulent eddy viscosity, the mean strain rate tensor  $\mathbf{S} = \frac{1}{2}(\nabla \bar{\mathbf{u}} + \nabla \bar{\mathbf{u}}^\top)$ , the turbulent kinetic energy  $k = -\text{tr}(\mathbf{R})$ , and the identity matrix  $\mathbf{I}$ .

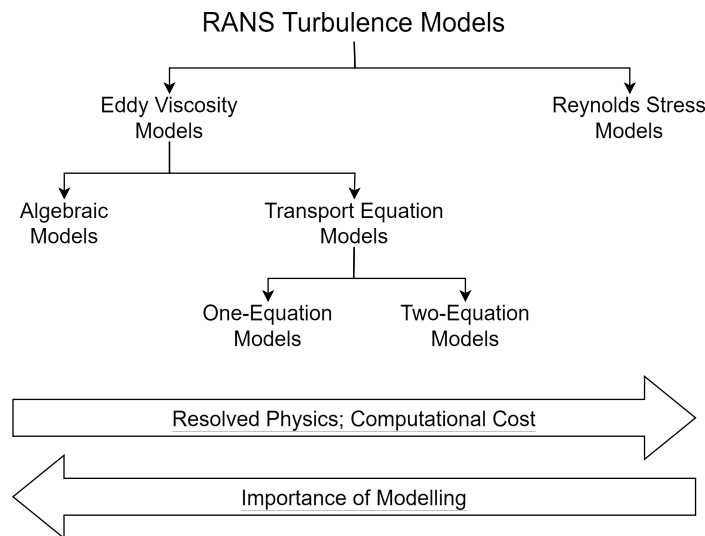


**Figure 2.1:** Schematic overview of the most common RANS turbulence modeling approaches.

The turbulent kinetic energy and the turbulent eddy viscosity must be determined using approaches such as algebraic models or transport equations of different variables. The second category of RANS closure models contains REYNOLDS stress models (RSMs) that model the individual components of the REYNOLDS stress tensor. These models are the most general form of RANS models. However, they come with an additional cost, are less validated, and are less numerically robust. Figure 2.1 gives an overview of RANS turbulence modeling approaches. The figure illustrates the trade-off between resolving the actual physical behaviour which comes with an increase in computational cost and the need for correct modeling assumptions. However, it must be noted that an increase in modeling efforts can not always mitigate deficiencies in the overall model structure. This is further elaborated in section 2.4.3.

### 2.4.1 Spalart-Allmaras One-Equation Model

The SPALART-ALLMARAS (SA) turbulence model is a one-equation turbulence model describing the transport of turbulent eddy viscosity [31]. When dealing with external aerodynamics such as an airfoil flow, this model is a popular and well-validated choice. The turbulent kinetic energy is given by

$$\nu_t = \tilde{\nu} f_{v1} \quad (2.10)$$

$$\text{with } f_{v1} = \frac{\chi^3}{\chi^3 + C_{v1}^3} \quad (2.11)$$

$$\text{and } \chi = \frac{\tilde{\nu}}{\nu} \quad (2.12)$$

where  $\nu$  is the molecular kinematic viscosity and  $\tilde{\nu}$  is the SA variable. The transport of the SA variable is given by the following equations:

$$\frac{D\tilde{\nu}}{Dt} = P - D + T \text{ with} \quad (2.13)$$

$$\frac{D\tilde{\nu}}{Dt} = \frac{\partial \tilde{\nu}}{\partial t} + \mathbf{u} \nabla \tilde{\nu}, \quad (2.14)$$

$$P = C_{b1} [1 - f_{t2}], \quad (2.15)$$

$$D = \left[ C_{w1} f_w - \frac{C_{b1}}{\kappa^2} \right] \left( \frac{\tilde{\nu}}{d} \right)^2 \text{ and} \quad (2.16)$$

$$T = \frac{1}{\sigma} \{ \nabla \cdot [(\nu + \tilde{\nu}) \nabla \tilde{\nu}] + C_{b2} |\nabla \tilde{\nu}|^2 \} \quad (2.17)$$

$P$  denotes the production of turbulence,  $D$  is turbulence destruction, and the term  $T$  represents the diffusive transport. Explanations regarding all variables can be found in the original publication [31] and are not further discussed to keep this text concise.

In this thesis, the negative SA (SA-neg) model which is implemented in DLR TAU-code is used [28, 32]. This variation of the model has improved numerical robustness over the original SA model by introducing a term which applies when  $\nu_t$  is negative, which can be found in the referenced publication.

#### Assessment of the SA Model

The advantages of the SA model are being a simple and numerically robust model with wide usage and validation. The model delivers a complete closure with just one equation.

In contrast to two-equation models it is simpler, but delivers equally good results in many applications. The model is superior to simpler algebraic models.

Known disadvantages are a reduced accuracy for incompressible flows with adverse pressure gradients or shock-induced separation. As these kinds of flows are critical in aerospace design it is of interest to mitigate the resulting errors [30].

### 2.4.2 Reynolds Stress Model

In contrast to the SA model, REYNOLDS stress models (RSMs) do not rely on the BOUSSINESQ hypothesis (eq. 2.9). Instead, RSMs describe the individual parts of the REYNOLDS stress tensor:

$$\mathbf{R} = -\overline{\mathbf{u}'\mathbf{u}'} = - \begin{pmatrix} \overline{u'_x u'_x} & \overline{u'_x u'_y} & \overline{u'_x u'_z} \\ \overline{u'_y u'_x} & \overline{u'_y u'_y} & \overline{u'_y u'_z} \\ \overline{u'_z u'_x} & \overline{u'_z u'_y} & \overline{u'_z u'_z} \end{pmatrix} \quad (2.18)$$

As equation 2.18 shows, the tensor is symmetric with six unknown components that need to be determined by solving six additional partial differential equations (PDEs).

#### Assessment of the RSM Model

RSMs are the most general approach to turbulence modeling for RANS equations. Furthermore, an improved accuracy in some flows can be observed. However, this comes with the cost of solving six additional PDEs. In addition, RSMs are less validated and less numerically robust when compared to eddy viscosity models [30].

#### Specifications used in this Thesis

An RSM is used in this thesis as a higher fidelity numerical comparison to the SA model. Whenever this model is used, the following specifications are used. Further details may be found in the cited references:

- The pressure-strain correlation is handled according to the SSG/LRR- $\ln(\omega)$  model [30, 33].
- According to Rotta, the dissipation is assumed isotropic [34].
- The simple gradient diffusion hypothesis is used [35].
- As length scale equation, the  $\ln(\omega)$ -equation according to the Menter baseline model is used [36].

### 2.4.3 Uncertainties due to Simplification

The assumptions introduced by the process of REYNOLDS-averaging and turbulence modeling are well reasoned, nevertheless, the resulting inadequacies must be noted. Duraisamy *et al.* describe four levels of simplifications [8]:

- Level 1: The process of averaging leads to a fundamentally irrecoverable loss of information.
- Level 2: Closure models are developed to relate the macroscopic state of the flow to the microscopic state, which is not resolved. The underlying assumptions about

which independent variables to choose lead to uncertainties in the functional and operational representation of the REYNOLDS stresses.

- Level 3: The functional representation that is chosen to relate the chosen variables leads to further uncertainties.
- Level 4: Finally, a given model has uncertainties based on the coefficients that are chosen to calibrate the model.

## 2.5 Resulting Task

The previous sections state the physical problem of transonic and unsteady flows, explain how this problem can be solved using RANS equations in combination with the SA turbulence model, and describe the shortcomings of the described approach. Given these inadequacies, a methodology to improve the prediction quality of RANS equations is of interest.

Reference data stemming from experiments or higher fidelity simulations can be used to quantify this error. Consequently, the overall goal of this thesis is to improve RANS simulations with the SA model in such a way that the error between a predicted quantity  $q$  and a reference quantity  $q_{\text{ref}}$  stemming from experiments or an RANS simulation with the RSM model is minimised.

# Chapter 3

## Field Inversion and Machine Learning

Field inversion and machine learning (FIML) is a data-driven turbulence modeling approach that utilizes higher fidelity reference data to improve RANS simulations. Thus, the FIML approach is fitting to the problem described in section 2.5.

If not indicated differently, the content of this chapter is based on these publications [8, 15, 18, 33].

### 3.1 Idea

The main idea of the FIML approach, proposed by Duraisamy *et al.*, is to alter a given turbulence model by introducing a spatially and possibly temporally distributed correction term  $\beta$  [8]. Introducing the correction term into the SA turbulence model as stated in equation 2.13 results in the following equation:

$$\frac{D\tilde{\nu}}{Dt} = \beta P - D + T \quad (3.1)$$

In equation 3.1, the correction is only applied to the production term. Since  $\beta$  can also be negative, the corrected turbulence model can increase the turbulence destruction. While it is also possible to apply a term to the diffusive transport term, this is not done in this thesis, since equation 3.1 is implemented in the DLR TAU-code [28]. Furthermore, different publications show that this version of the altered turbulence model can correct simulations in separated and transonic flows [16, 18].

The values of the correction term are unknown. However, it is assumed that an unknown functional relationship between  $\beta$  and the flow state  $(\mathbf{U}, \tilde{\nu})$  exists.  $\mathbf{U}$  contains all the mean flow variables. The goal of the ML part of the approach is to find a data-driven model  $f_\beta$  that describes the functional relationship:

$$f_\beta: \eta_1(\mathbf{U}, \tilde{\nu}), \dots, \eta_n(\mathbf{U}, \tilde{\nu}) \mapsto \beta \quad (3.2)$$

with  $\eta_1 \dots \eta_n$  flow features depending on the flow state  $(\mathbf{U}, \tilde{\nu})$ . The steps to find a functional relationship according to equation 3.2 are explained in sections 3.3 and 3.4.

### 3.2 FIML Classic

The FIML Classic methodology is a two-step approach which first builds a database containing the results of multiple field inversions (FIs), as presented in section 3.3 [8]. In the second step, in section 3.4, a machine learning (ML) model is built using the field inversion results. Finally, the resulting correction model is applied within a RANS solver, as given in section 3.5. This workflow is visualised in Figure 3.1. The individual parts are explained in detail in the following sections.

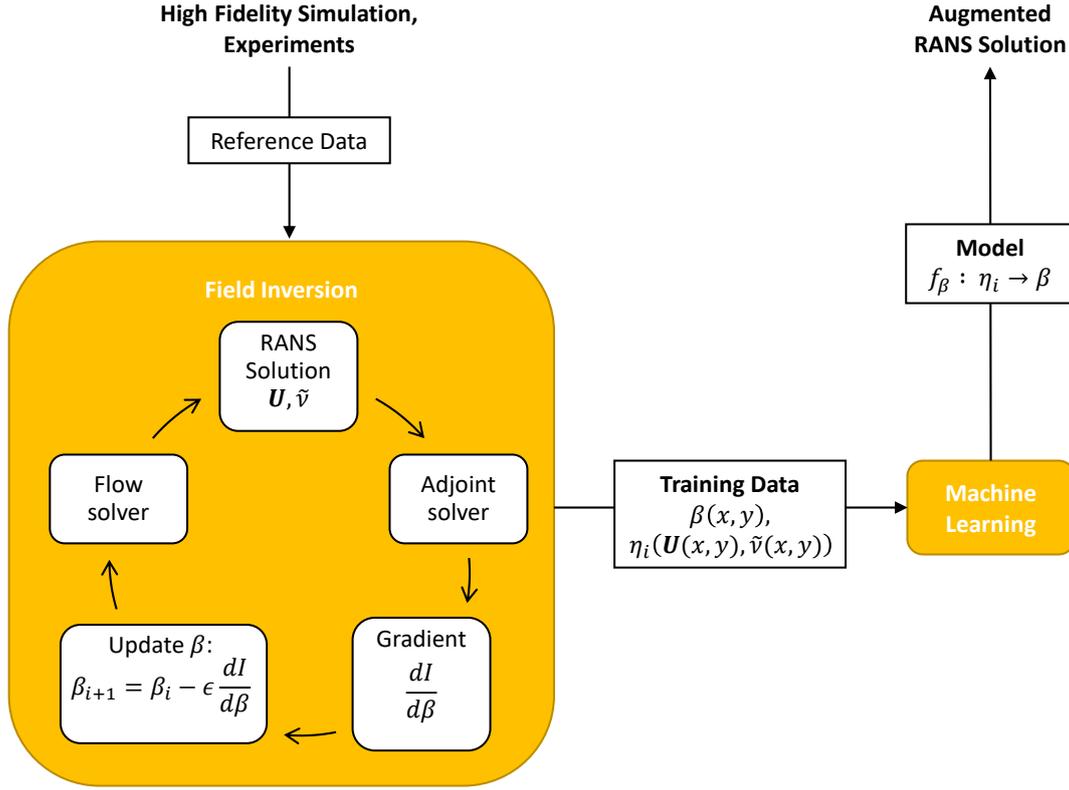


**Figure 3.1:** Workflow of FIML Classic as in [18].

### Assessment

For the FIML Classic approach, each FI is performed separately and allows gaining insights into the correction results before training a machine learning model. Furthermore, the database containing the inversion results can be extended if needed. Another advantage is that the ML training can be done offline using established methods. However, performing the FI and ML steps separately exhibits two error sources: next to an imperfect FI the ML model might be inconsistent with training data.

For completeness, the FIML Direct approach must be mentioned here. Holland *et al.* introduced a closed-loop form of the FIML approach by integrating the ML model training into the FI step, further information can be found in the publication [17].

## 3.3 Field Inversion

The goal of the field inversion is to find spatially distributed values for  $\beta$  such that the corrected RANS solution according to equation 3.1 matches a reference solution. The reference solution might be experimental data or a higher fidelity numerical solution. The comparison of the corrected RANS simulation and the reference solution is done by comparing the reference quantities  $q(\beta)$  and  $q_{\text{ref}}$ :

$$q(\beta) \stackrel{!}{=} q_{\text{ref}} \quad (3.3)$$

The reference variables can be global values as the coefficient of lift  $c_l$ , scalar field values as pressure  $p$ , or vectorial field values as the flow velocities  $\mathbf{u}$ . The number of reference

variables can be sparse, i.e. smaller than the number of the corresponding quantities in the RANS solution.

Equation 3.3 states an inverse problem that can be iteratively solved by minimising a cost function  $\mathcal{I}$ :

$$\mathcal{I} = \underbrace{\frac{1}{2V_{\text{tot}}} \sum_i^N V_i (q_{i,\text{ref}} - q_i(\beta))^2}_{\mathcal{I}_1} + \lambda \underbrace{\frac{1}{2\tilde{M}} \sum_j^{\tilde{M}} (\beta_j - \beta_0)^2}_{\mathcal{I}_2} \quad (3.4)$$

The first term  $\mathcal{I}_1$  is the mean squared error (MSE) between the reference and the RANS solution at each of the  $N$  nodes where a reference solution is available. For field reference values, the squared differences are weighted according to the cell volume  $V_i$ . With  $N$  the number of reference data points usually being smaller than  $\tilde{M}$  degrees of freedom the inverse problem is *ill-posed*. To ensure smoothness of the numerical simulation, the term  $\mathcal{I}_2$  is a TIKHONOV regularisation penalising strong correction terms [37, 38].  $\tilde{M}$  is the number of overall nodes in the computational domain.  $\beta_0$  refers to the correction field that leads to an unchanged turbulence model, i.e. according to equation 3.1 for the given SA model it is  $\beta_0 = 1$ . By altering the value of the regularisation parameter  $\lambda$  the influence of the regularisation term can be controlled.

Being influenced by the RANS equations, the cost function is non-linear and is solved iteratively, this can be done using a gradient-based method. Consequently, the computation of the gradient of the cost function with respect to the correction term  $d\mathcal{I}/d\beta$  is required. Different approaches can be used to evaluate the gradient. For high-dimensional aerodynamic optimisation problems, the adjoint method is very efficient, as the number of function evaluations scales with the number of cost functions and not the number of unknown variables, i.e.  $\beta$  at each node [39]. Furthermore, this method is implemented in the DLR TAU-code [28].

After computing the gradient, a line-search backtracking optimisation in the direction of the steepest descent can be performed for a set number of iterations or until an AMRIJO-GOLDSTEIN condition is reached [40, 41]. This concludes the FI and the resulting  $\beta$ -field can be used for machine learning as explained in section 3.4.

## 3.4 Machine Learning

Comparing a baseline solution with reference data in an FI delivers a RANS solution and a corresponding  $\beta$ -field (see section 3.3). The goal of the machine learning step is to find a functional relationship between features based on mean flow variables of the RANS solution and the  $\beta$ -field.

In subsection 3.4.1, the general idea of data-driven methods is introduced. Then, the task of ML in the context of FIML is explained in subsection 3.4.2. Subsequently, the specific machine learning approaches used in this thesis are explained in subsection 3.4.4.

### 3.4.1 Data-Driven Methods

Traditional modeling of physical systems is achieved by describing the underlying physical phenomena using equations based on the knowledge of the physical system. This has the

clear advantage that the results are explainable. However, it requires deep insight and a sufficient understanding of the physical system. Furthermore, solving the resulting systems of equations can be very expensive.

As stated by MOORES law computational resources become more powerful and the creation and processing of large amounts of data becomes cheaper [42]. These technical advancements enable the growing popularity and accessibility of data-driven methods that make use of data, aiming to find structures that can be generalised to make predictions.

ML is a data-driven method and an artificial intelligence (AI) approach. Classical ML such as regression models use hand-designed input features to generate an output. As a more powerful form of ML, deep learning (DL) approaches use several mapping layers to generate abstract mappings of the input features. Consequently, DL models are capable of describing highly non-linear input-output, or *feature-target* relationships. The approaches can be used for a variety of tasks, in this thesis regression models are of interest [43, 44].

### 3.4.2 Purpose of ML in FIML

To complete the FIML approach a model  $f_\beta$  that describes the functional relationship between the local flow features  $\eta_i(\mathbf{U}(\mathbf{x}), \tilde{\nu}(\mathbf{x}))$  and the target quantity  $\beta(\mathbf{x})$  as stated in equation 3.2 is required. By supplying a database containing data for different global conditions, the goal is to train an ML model that learns the underlying structures and can generalize on previously unseen data.

### 3.4.3 Feature Selection

The features must be included in or be computable from the mean flow variables that are obtained from a RANS simulation. Possible features can be found in the literature. By evaluating the SPEARMAN's rank correlation [45] between possible features and the target value, as well as by performing a sequential feature selection [46], five features are determined in [16]. Similar features are also used in [17] and [18], and implemented in the DLR Surrogate Modeling for Aero-Data Toolbox in python (SMARTy) [47]:

- $\eta_1 = \frac{P}{D}$ : ratio of turbulent production to destruction.
- $\eta_2 = \chi$ : non-dimensionalised Spalart-Allmaras viscosity.
- $\eta_3 = \frac{|\mathbf{S}|}{|\boldsymbol{\Omega}|}$ : ratio of the magnitudes of strain to vorticity.
- $\eta_4 = \frac{\mu_t |\mathbf{S}|}{\tau_w}$ : ratio of the local turbulent stresses to the wall shear stresses at the closest wall.
- $\eta_5 = \overline{\Omega} = \frac{d^2}{(\nu + \tilde{\nu})|\Omega|}$ : the non-dimensionalised magnitude of the vorticity tensor.

Based on the value range a logarithm is applied to some of the features in the literature. The feature selection is case-dependent. Subsequently, requirements and correlation metrics to evaluate possible features are described.

### Requirements

Features must be locally available: the information required to compute a feature must be available at each mesh point. However, as  $\eta_4$  shows, it is possible to make unavailable information accessible, e.g. if a value is only available at walls, the closest value might be

used. Machine learning models process data regardless of their dimension. However, to ensure dimensional consistency, the input features should be dimensionless. Furthermore, turbulence models typically assume GALILEAN invariant features: a possible feature must be the same in all inertial reference frames. The latter two requirements are favourable, though the main objective is to obtain a satisfactory ML model [16].

### Correlation Metrics

The correlation between a feature and the target value can give insights into whether a feature is useful to describe the target. Three correlation coefficients are used in this thesis to compare two generic vectors  $\mathbf{o}_1, \mathbf{o}_2$ :

- PEARSON's correlation coefficient  $r_p$  measures the linear relationship, where  $r_p = \pm 1$  is a perfected (inverse) correlation and  $r_p = 0$  indicates no correlation [48]. Given the mean values  $\bar{\mathbf{o}}_1$  and  $\bar{\mathbf{o}}_2$  it can be computed by

$$r_p = \frac{\sum (\mathbf{o}_1 - \bar{\mathbf{o}}_1) (\mathbf{o}_2 - \bar{\mathbf{o}}_2)}{\sqrt{\sum (\mathbf{o}_1 - \bar{\mathbf{o}}_1)^2 \sum (\mathbf{o}_2 - \bar{\mathbf{o}}_2)^2}}. \quad (3.5)$$

- SPEARMAN's rank correlation coefficient  $r_s$  measures the monotonicity of the relationship between two vectors and can take the same values as  $r_p$  [45, 48]. With the ranks  $R(\mathbf{o}_1)$  and  $R(\mathbf{o}_2)$  as well as the standard deviation of the ranked variables  $\sigma_{R(\mathbf{o}_1)}$  and  $\sigma_{R(\mathbf{o}_2)}$  it can be computed as

$$r_s = \frac{\text{cov}(R(\mathbf{o}_1), R(\mathbf{o}_2))}{\sigma_{R(\mathbf{o}_1)}, \sigma_{R(\mathbf{o}_2)}}. \quad (3.6)$$

- Grabe *et al.* proposed to use a correlation coefficient that can capture non-monotonous relationships [16]. The distance correlation  $r_d$  describes the relationship between two vectors using the distance of observations in an EUCLIDEAN space. Using the distance covariance  $\text{dCov}(\cdot)$ , and distance variance  $\text{dVar}(\cdot)$ , it can be evaluated by

$$r_d = \sqrt{\frac{\text{dCov}^2(\mathbf{o}_1, \mathbf{o}_2)}{\sqrt{\text{dVar}^2(\mathbf{o}_1) \text{dVar}^2(\mathbf{o}_2)}}}. \quad (3.7)$$

The resulting value of  $r_d$  is similar to the other correlation coefficients, but cannot be negative. Further information can be found in the publication [49].

#### 3.4.4 Methods

Two ML approaches of different complexity are used in this thesis: a regression model based on radial basis functions, and a fully-connected neural network.

##### Radial Basis Function Regression

The radial basis function (RBF) regression uses radial basis functions centred at the bases of a high-dimensional dataset to approximate the target value at non-base points. The influence of each base diminishes with distance from the centre [50].

Given a vector of features  $\boldsymbol{\eta} \in \mathbb{R}^n$ ,  $n$  RBFs  $\phi_i$  can be described as

$$\phi_i(\boldsymbol{\eta}) = \varphi(\|\boldsymbol{\eta} - \boldsymbol{\eta}_i\|), i = 1, \dots, n \quad (3.8)$$

where the function  $\varphi$  can be chosen. Four different types of RBFs are implemented in SMARTy [47].

### Fully-Connected Neural Network

Inspired by the structure of the brain, a *perceptron* multiplies an input vector  $\boldsymbol{\eta} \in \mathbb{R}^n$  with a weight vector  $\mathbf{w} \in \mathbb{R}^n$  and adds a bias  $b \in \mathbb{R}$ . The result is passed through a non-linear activation function  $g(\cdot): \mathbb{R} \rightarrow \mathbb{R}$  to produce an output. In accordance with the target quantity the output is called  $\beta \in \mathbb{R}$  [51]:

$$\beta = g(\mathbf{w}^\top \boldsymbol{\eta} + b) \quad (3.9)$$

Arranging multiple *neurons* as in equation 3.9 in  $l$  layers results in a multi-layer perceptron (MLP), also known as a fully-connected neural network (FCNN). The information from each of the  $q$  neurons in the  $i$ -th layer  $\mathbf{h}^{(i)} \in \mathbb{R}^q$  is passed to each of the  $p$  neurons in the  $(i+1)$ -th layer  $\mathbf{h}^{(i+1)} \in \mathbb{R}^p$ . The weights in each layer are gathered in a weight matrix  $\mathbf{W}^{(i)} \in \mathbb{R}^{(p,q)}$  and the biases are organised in a bias vector  $\mathbf{b}^{(i)} \in \mathbb{R}^q$ :

$$\mathbf{h}^{(i)} = g^{(i)}(\mathbf{W}^{(i)}\mathbf{h}^{(i-1)} + \mathbf{b}^{(i)}) \quad (3.10)$$

The dimension of the first layer is defined by the dimension of the feature vector  $\mathbb{R}^n$ , while the dimension of the last layer is given by the dimension of the target  $\mathbb{R}$ . The dimensions of the *hidden* layers, i.e. the layers between the first and the last layer, can be chosen and influence the model's behaviour. The models in this thesis use the ReLU activation function as in [52], are trained iteratively using backpropagation according to [53], and are implemented in SMARTy [47], using the PyTorch backend [54].

According to the *Universal Approximation Theorem* for each arbitrarily complex function, a neural network exists that approximates the function [55]. Consequently, neural networks are a potent tool. Nevertheless, the challenge of finding a satisfactory representation remains.

## 3.5 Application of Correction Model

Once a correction model is trained it can be applied by coupling the resulting ML model with a RANS solver. Thus, the application of the trained model is a solver intrusive correction procedure. Consequently, the entry barrier to applying the correction model is high, because the RANS solver must be capable of processing the predicted correction term. This requires compatibility of the ML model and the CFD code.

For steady simulations, the evaluation period of the correction model defines the number of inner iterations after which the turbulence model is evaluated. The correction term is obtained by evaluating the model based on the resulting values of the last inner iteration of the RANS solver and passing the resulting  $\beta$ -field as an input to the subsequent inner iteration. Varying the number of inner iterations between the evaluation of the correction model may affect the stability and convergence speed of the RANS solver.

Unsteady simulations augmented with a correction model are run for multiple sub-iterations within each physical time step. Each subiteration runs for a given number of inner iterations, as explained in subsection 2.2.2. The evaluation of the correction model is done before each subiteration. Thus, the correction model's evaluation period equals the number of inner iterations within each subiteration. By running multiple subiterations per

physical time step the correction model can be evaluated multiple times until a converged state is reached. Similar to the steady simulation, the number of inner iterations and subiterations may influence the stability and convergence speed.

Figure 3.2 visualises the application of the correction model for steady and unsteady simulations that are described in the text above.

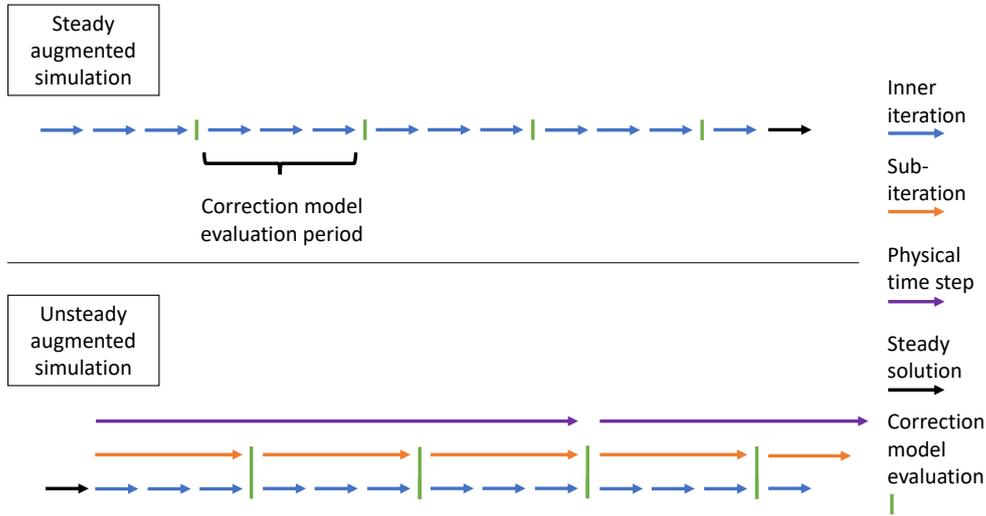


**Figure 3.2:** Application of turbulence model correction model within RANS solver for steady and unsteady simulations.

## 3.6 Current Implementations

This thesis uses the DLR’s software infrastructure including the node-centred, unstructured flowsolver TAU and the Surrogate Modeling for AeRo data Toolbox Python package (SMARTy) [28, 47]. SMARTy contains multiple data-driven capabilities and an interface to TAU. Two versions of the FIML approach are implemented: FIML Classic according to [7] and FIML Direct according to [17]. SMARTy contains the optimisation and ML capabilities that are required to perform an FI and train an ML model.

The application of correction models is possible using the SMARTy TAU interface. Currently, only a correction of the production term of the SA turbulence model is supported. Publications using both approaches, FIML Classic and FIML Direct, to correct steady simulations using the DLR software infrastructure are available [15, 16, 18]. Furthermore, an interface for correction models for unsteady simulations is implemented within SMARTy. However, no research work using this capability is available. Using and expanding this capability lies within the scope of this thesis.

Regarding the flowsolver TAU two capabilities are especially important for FIML. First, the flowsolver is capable of processing a correction term. However, as stated above only for the production term of the SA turbulence model. Furthermore, TAU contains an adjoint solver that can be used to compute the gradients that are necessary for the FI.

# Chapter 4

## Numerical Test Case

The objective of this chapter is to apply the concepts introduced in the preceding text to a test case with numerically computed reference data. Using the RAE 2822 two-dimensional airfoil case, as described in subsection 4.1.1, baseline data using the SA turbulence model, and higher fidelity reference data using the RSM turbulence model are produced in subsection 4.1.2. Given these steady aerodynamic data points, FIs are computed in section 4.2, before an ML model is trained in section 4.3. The resulting model is applied to steady simulations in section 4.4 as well as unsteady simulations in section 4.6.

### 4.1 Case Description and Preparation

First, this section describes the selected test case in subsection 4.1.1. Afterwards, the generation of numerical data is described in subsection 4.1.2.

#### 4.1.1 RAE 2822 Airfoil

The RAE 2822 airfoil is a rear-loaded, sub-critical airfoil with a roof-top type pressure distribution at design conditions  $M_{\infty, \text{Design}} = 0.66$ ,  $c_{l, \text{Design}} = 0.56$  [56]. Figure 4.1 presents the geometry of the airfoil.

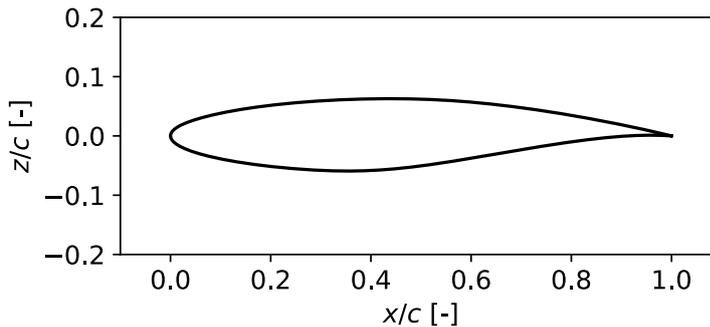


**Figure 4.1:** RAE 2822 airfoil geometry.

For this airfoil, experimental data from measurements by Cook *et al.* [57] is available. Furthermore, the author has access to the AIRBUS RWC.01 database from a measurement campaign in the European Transonic Wind Tunnel. Given the availability of experimental data, the RAE 2822 airfoil is a common validation case for turbulence modeling, e.g. proposed as such a validation case by NASA [58]. Regarding data-driven turbulence modeling using the FIML approach, the airfoil has been used in previous studies [16, 18].

Additionally, the author has access to differently sized computational meshes for the airfoil as used in [59]. Given the legacy as a test case and the data availability, the RAE 2822 is selected to be used in this thesis.

### 4.1.2 Data Generation

Using the RAE 2822 airfoil, steady simulations are conducted to cover transonic effects, especially shocks.

#### Flow Conditions

The free-stream flow conditions, i.e. MACH and REYNOLDS number, for the generation of reference and baseline data, are fixed while the angle of attack is varied due to the following two considerations:

1. Because experimental measurements in wind tunnels or flight tests are often done by fixating the free stream conditions, i.e. MACH and REYNOLDS number, and varying the angle of attack, a similar approach is chosen for the numerical data.
2. The goal is to apply the correction model, which is trained using results of FIs on steady data, to unsteady simulations with a harmonically pitching airfoil, i.e. a changing  $\alpha$ . The idea is to implicitly learn how the correction field changes with the angle of attack  $d\beta/d\alpha$ .

The reasoning fits the objective of this thesis, but it must be noted that fixing  $M$  and  $Re$  comes with a reduced generalizability towards other flow conditions.

The following simulations are done with  $M = 0.75$  and  $Re = 6.0 \cdot 10^6$ . These flow conditions produce a transonic flow including a shock. The angle of attack is varied in the range  $\alpha \in [0^\circ, 15^\circ]$  in steps of size  $0.5^\circ$ , resulting in 31 simulations.

#### Mesh

To run a CFD simulation a mesh is necessary to describe a spatial discretisation of the computational domain into finite volumes (or cells) [4]. The refinement of the cells influences the CFD simulation. For each cell of the mesh, the RANS equations must be solved. Consequently, the number of degrees of freedom and therefore the computational effort grows with the number of cells. Thus, looking at the computational effort it is favorable to have a small number of large cells. However, larger mesh cells resolve fewer physical effects that must be modeled to get an accurate solution. A trade-off between resolving as many physical effects as possible while confining the computational cost is the purpose of a mesh dependency study.

Even though the FIML approach is not only able to correct errors caused by the turbulence model but also discretisation errors as shown in [15], the focus of this thesis lies on errors caused by the turbulence model. Consequently, the chosen mesh should not exhibit large discretisation errors.

Several meshes for the RAE 2822 are compared in [59]. Based on these results for this thesis a mesh with 512 nodes on the airfoil and 256 nodes in normal direction is chosen. The pressure distribution as well as the global coefficients on the airfoil computed using this mesh show only small deviations to results computed with a finer mesh, thus, mesh convergence is assumed to be reached. The selected mesh is depicted in Figure 4.2.

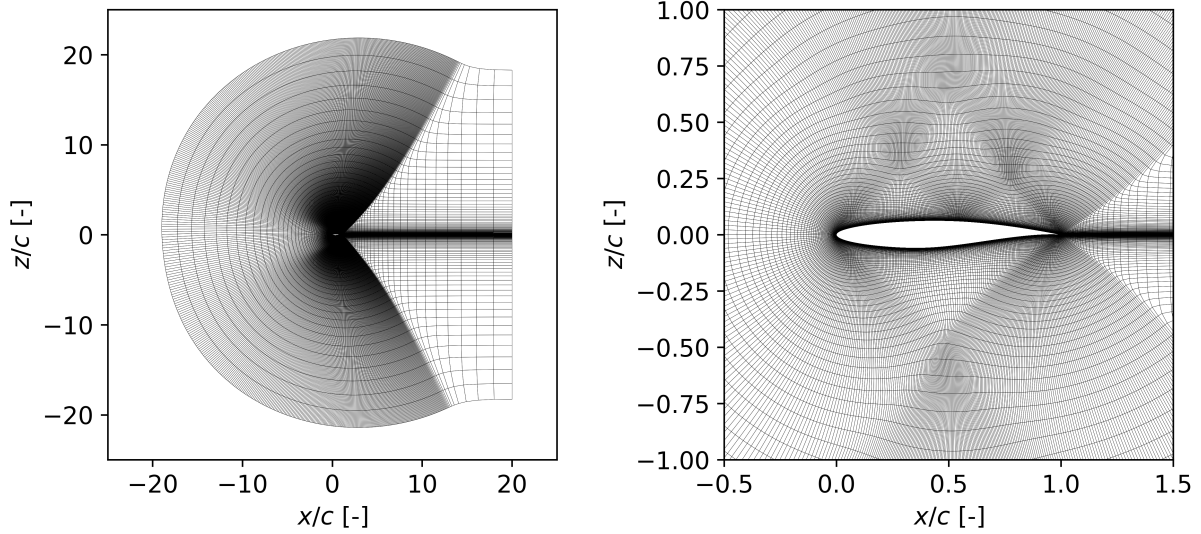


**Figure 4.2:** Mesh used in this study. Left: full domain. Right: zoom on the airfoil.

### Baseline Data

As a baseline comparison, the RANS simulations are executed using the SA turbulence model as introduced in subsection 2.4.1. Before using the flow conditions stated above, the integrity of the mesh is validated by reevaluating case 9 from [59] and comparing the resulting global coefficients  $c_l$ ,  $c_d$ , and  $c_{my}$ . This is done using the DLR TAU code [28].

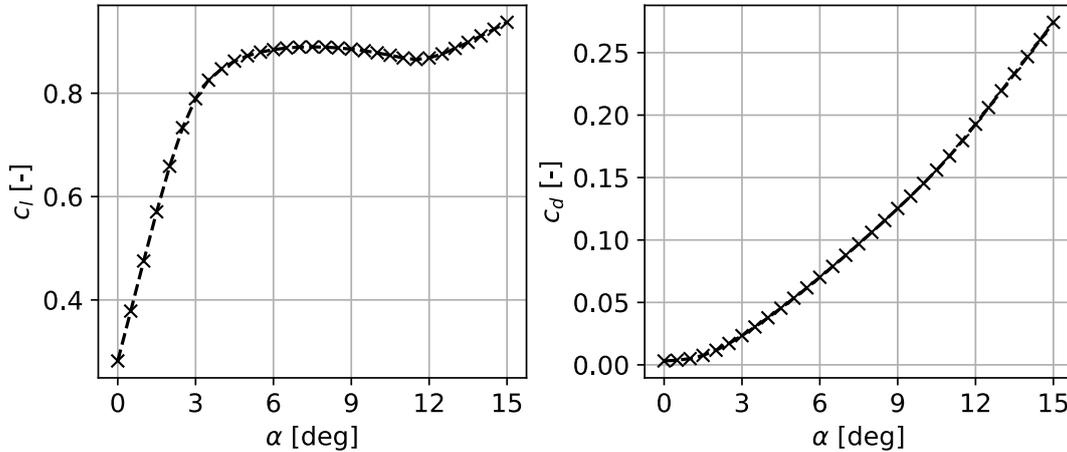


**Figure 4.3:**  $c_l$  (left) and  $c_d$  (right) over  $\alpha$  for  $M = 0.75$   $Re = 6.0 \cdot 10^6$  using the SA turbulence model.

Subsequently, the simulations at  $M = 0.75$  and  $Re = 6.0 \cdot 10^6$  are executed. A COURANT-FRIEDRICHS-LEWY (CFL) number of 5 leads to converging simulations for all selected angles of attack. Figure 4.3 presents the resulting coefficient of lift and drag. Up to approximately  $\alpha = 2.5^\circ$ , a linear relationship between lift and angle of attack can be seen. Beyond that point the relationship is non-linear. At  $\alpha = 7.5^\circ$   $c_{l,max} \approx 0.89$  can be found, indicating the beginning of the stall region. Contrary to an expected lift curve, beyond  $\alpha = 12^\circ$  the lift is increasing again.

## Reference Data

RANS simulations using the RSM turbulence model as introduced in subsection 2.4.2 serve as higher fidelity reference data for this test case. In comparison to the SA model, the RSM is more complex and resolves the acting physical effects to a higher degree. However, this comes with the cost of reduced numerical stability. With a CFL number of 1.5, simulations up to  $\alpha = 6^\circ$  converge. Varying the CFL number and settings regarding the turbulence model, e.g. the selected diffusion model, influences the numerical computation. However, for higher angles of attack, no converged results are obtained.

Figure 4.4 shows the results. The coefficient of lift for  $\alpha = 6^\circ$  is an outlier compared to the other values. Even though the simulation did converge, it is neglected for further analysis. Again, a linear dependency of  $\alpha$  and  $c_l$  can be found up to 2.5 degrees angle of attack.  $c_{l,max} \approx 0.85$  is located at  $\alpha = 5.0^\circ$ .

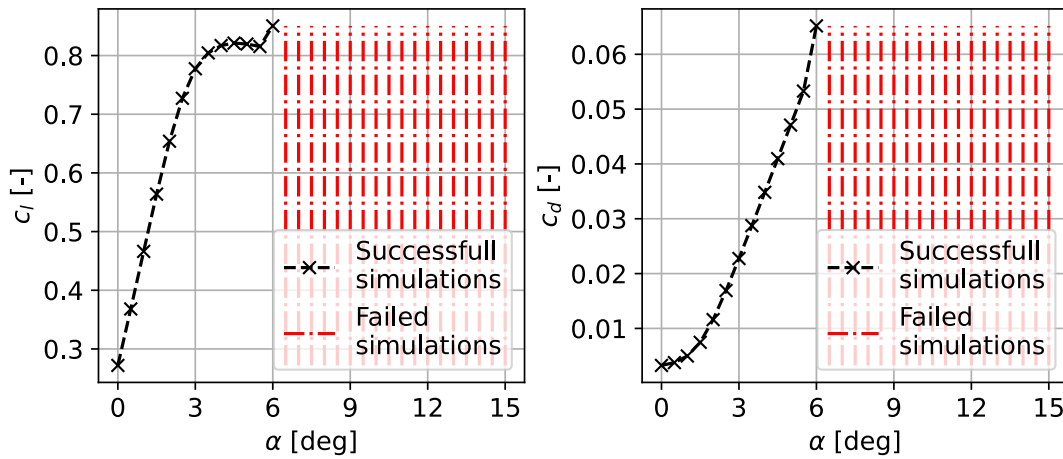


**Figure 4.4:**  $c_l$  (left) and  $c_d$  (right) over  $\alpha$  for  $M = 0.75$ ,  $Re = 6.0 \cdot 10^6$  using the RSM turbulence model.

## Data Comparison

Comparing the baseline data obtained using the SA model to the reference data obtained using the RSM model allows to identify differences that might be corrected using the FIML approach. This comparison can only be done up to  $\alpha = 5.5^\circ$  because, for higher angles of attack, no reference results exist. Figure 4.5 confirms a good match of SA and RSM in the linear range up to 2.5 degrees. Beyond that point, the results for  $c_l$ ,  $c_d$ , and  $c_{my}$  deviate. SA predicts higher values for both: drag and lift. The maximum lift, indicating the beginning of the stall region, occurs at a smaller angle of attack for RSM than SA. Thus, the differences between the results are not only quantitative but also qualitative. For  $c_{my}$  the predicted values of RSM are higher than SA. Again a qualitative difference for  $\alpha > 3^\circ$  can be found: for RSM  $\frac{dc_{my}}{d\alpha} > 0$ , whereas for SA  $\frac{dc_{my}}{d\alpha} \approx 0$ . This difference is significant for the longitudinal stability.

To get further insights into the differences the distributions of the pressure coefficient  $c_p$  at the airfoil surface are compared. Figure 4.6a presents a good match of SA and RSM at  $\alpha = 1.5^\circ$ . At  $x/c \approx 0.55$ , a significant increase in pressure, indicating a shock, is present. The shock is the only region in the  $c_p$  distribution exhibiting a small deviation between the two turbulence models. Since the lift of the airfoil can be computed by integrating

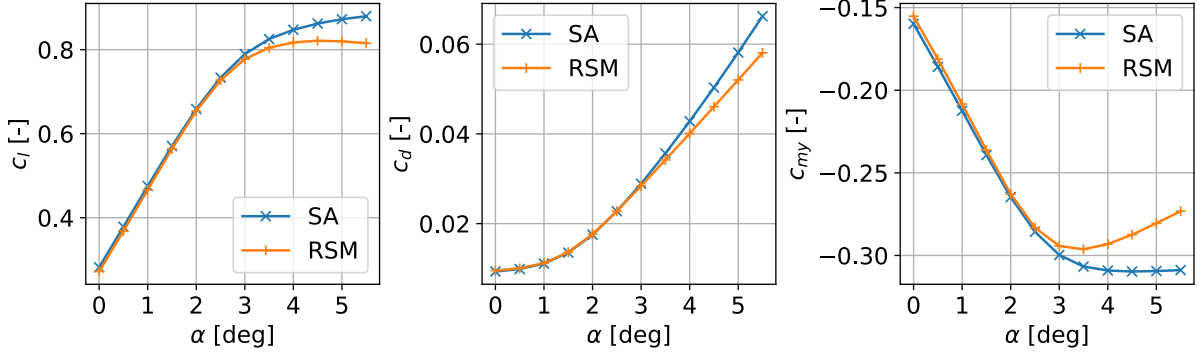


**Figure 4.5:**  $c_l$  (left),  $c_d$  (middle), and  $c_{my}$  (right) over  $\alpha$  for  $M = 0.75$   $Re = 6.0 \cdot 10^6$  comparing SA and RSM.

the pressure over the airfoil surface, it becomes obvious that for  $\alpha = 1.5^\circ$  the lift values are very close as described previously. It must be noted that the drag is also significantly influenced by skin friction. At  $\alpha = 4.5^\circ$  larger differences can be seen. As Figure 4.6b indicates, a mismatch between SA and RSM can be seen behind the shock at  $x/c \approx 0.55$ .

Even though one might expect larger deviations for reference data stemming from experiments, the presented differences to the higher fidelity RANS simulations significantly influence the resulting forces, making it a suitable initial test case.

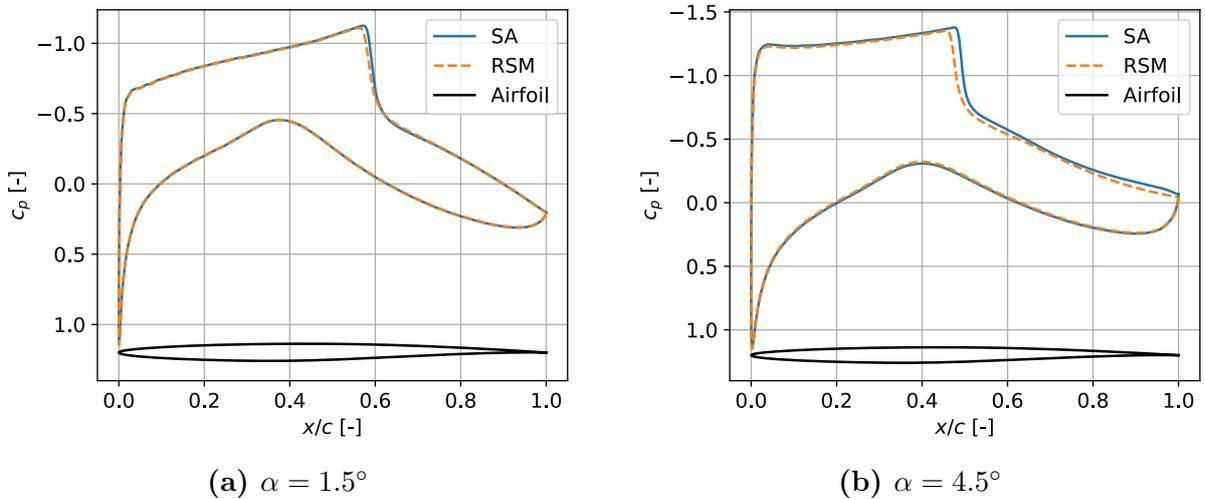


**Figure 4.6:**  $c_p$ -distribution on airfoil surface for  $M = 0.75$ ,  $Re = 6.0 \cdot 10^6$  comparing SA and RSM.

## 4.2 Field Inversion on Steady Simulations

Using the reference data obtained in section 4.1, a field solution containing correction values  $\beta$  can be computed by executing a field inversion as introduced in section 3.3. Therefore, in subsection 4.2.1, several investigations regarding the process of FI are conducted before in subsection 4.2.2 the resulting correction fields for the given data are discussed.

### 4.2.1 Considerations and Investigations

Before executing the field inversions to be used for machine learning some questions must be clarified:

- Which variable to use as reference data?
- How many reference data points must be used?
- What is the effect on variables that are not used as reference data?
- What are the limitations of the approach?

The stated questions are discussed considering a realistic application scenario.

#### Reference Quantity

As explained in section 3.3, global values, scalar field values, as well as vectorial field values might be used as reference quantity  $q_{\text{ref}}$ .

Duraisamy *et al.* state that even very limited experimental reference data as the coefficient of lift can lead to a considerable improvement of the entire flow field [8]. The measurement of global force coefficients is standard practice in wind tunnel measurements. However, in flight tests, these forces are usually not measured directly.

Using the flow velocity as a vectorial reference value delivers large informational content. However, these measurements require advanced techniques, e.g. particle image velocimetry (PIV) [60], that are expensive and not standard procedure for both wind tunnel measurements and flight tests.

Pressure measurements, especially on the airfoil surface are common practice, most often done using pressure taps on the airfoil surface. In addition, measurements using pressure-sensitive paint (PSP) are being advanced [61]. In contrast, measuring the pressure in the flow field around the airfoil requires far more effort and is not standard practice.

Considering the discussed possibilities the pressure on the airfoil surface is chosen as the reference quantity for this test case. As it is standard practice to use the dimensionless pressure coefficient instead of pressure when analysing the flow around an airfoil this quantity is used:

$$q_{\text{ref}} = c_p = \frac{p - p_{\infty}}{\frac{1}{2}\rho_{\infty}|\mathbf{u}_{\infty}|^2} \quad (4.1)$$

with static pressure  $p$ , free-stream static pressure  $p_{\infty}$ , free-stream air (or fluid) density  $\rho_{\infty}$ , and free-stream flow velocity  $|\mathbf{u}_{\infty}|$ .

#### Number of Reference Points

The pressure coefficient  $c_p$  is available at 512 locations on the surface of the airfoil corresponding to the number of mesh nodes on the surface, as in explained subsection 4.1.2. Assuming that the higher the amount of reference data, the better the resulting  $\beta$ -field, the idea must be to use all of the 512 data points. However, this number of measurement points might be unfeasible in an experiment. Moreover, a higher number of reference points leads to an increased computational effort and might impede the convergence of

the field inversion. Consequently, it is of interest to investigate how smaller numbers of reference points affect accuracy and computational cost.

Multiple field inversions are computed for the  $\alpha = 5.5^\circ$  case. The regularisation parameter  $\lambda$  is case-dependent and must be determined individually. The final values are determined in subsection 4.2.2. For the investigations in this subsection, it is set to  $\lambda = 10^{-12}$ , corresponding to high trust in the reference data. The minimum residual for the flow solution is set to  $10^{-8}$ . The adjoint solver minimum residual is set to  $10^{-5}$ . Both the flow and the adjoint solution are computed using the DLR TAU code [28]. The line search along the steepest gradient is conducted until the ARMIJO-GOLDSTEIN condition with a control parameter of  $10^{-16}$  is fulfilled. Overall, 150 FI iterations are set as an upper bound to limit computational cost.

The number of reference points is varied for each FI. Table 4.1 defines the investigated cases. For each case, the reference points are spread evenly over the airfoil surface, e.g. for the 25% case, every 4<sup>th</sup>  $c_p$  value of the full reference solution is used.

Figure 4.7 presents the results of this investigation. The bars correspond to the number of FI iterations. A clear trend can be seen: fewer iterations are necessary for smaller numbers of reference points. The FIs using 512, 256 and 128 reference points do not reach convergence within 150 iterations. It is unknown whether convergence would be reached within a higher number of iterations. The lines present various errors comparing the RSM reference data and the RANS solution with the SA turbulence model that is augmented using the correction term  $\beta$ . As an overall trend, errors decrease for a larger number of reference points. Especially for 3.12% reference points and less a very strong increase in errors can be seen. A small spike can be seen at 25%, but since this FI did not converge this spike can be disregarded.

Percentage [%]	100.00	50.00	25.00	12.50	6.25	3.12	1.56	0.78	0.39
Number of points	512	256	128	64	32	16	8	4	2

**Table 4.1:** Numbers of investigated reference points

The individual errors are not just influenced by the number of reference points, but also by their placement. Figure 4.8 compares three  $c_p$  distributions on the airfoil surface to gain further insights.

As visible in Subfigure 4.8a, four reference points are too sparse to produce a good correction. Three of the four points reference points are at locations with minimal differences between baseline and reference. Consequently, only the difference at one reference point significantly influences the FI's cost function. Since FI is an ill-posed mathematical problem, as stated in section 3.3, more than one solution for the  $\beta$ -field exists. Chances are low that using only one significant reference point does lead to a good correction of  $c_p$  at locations other than the reference point.

The 12.50% case in Subfigure 4.8b exhibits more reference points in the post-shock area with strong differences. However, no reference point is located at the shock itself. The inversion result is close to the reference solution, but not perfect: a small difference at the rear ( $x/c \approx 0.9$ ) and the shock can be seen.

With a reference point at the shock the inversion result for the 50.00% case in Subfigure 4.8c matches the reference the best, even though the inversion did not converge.

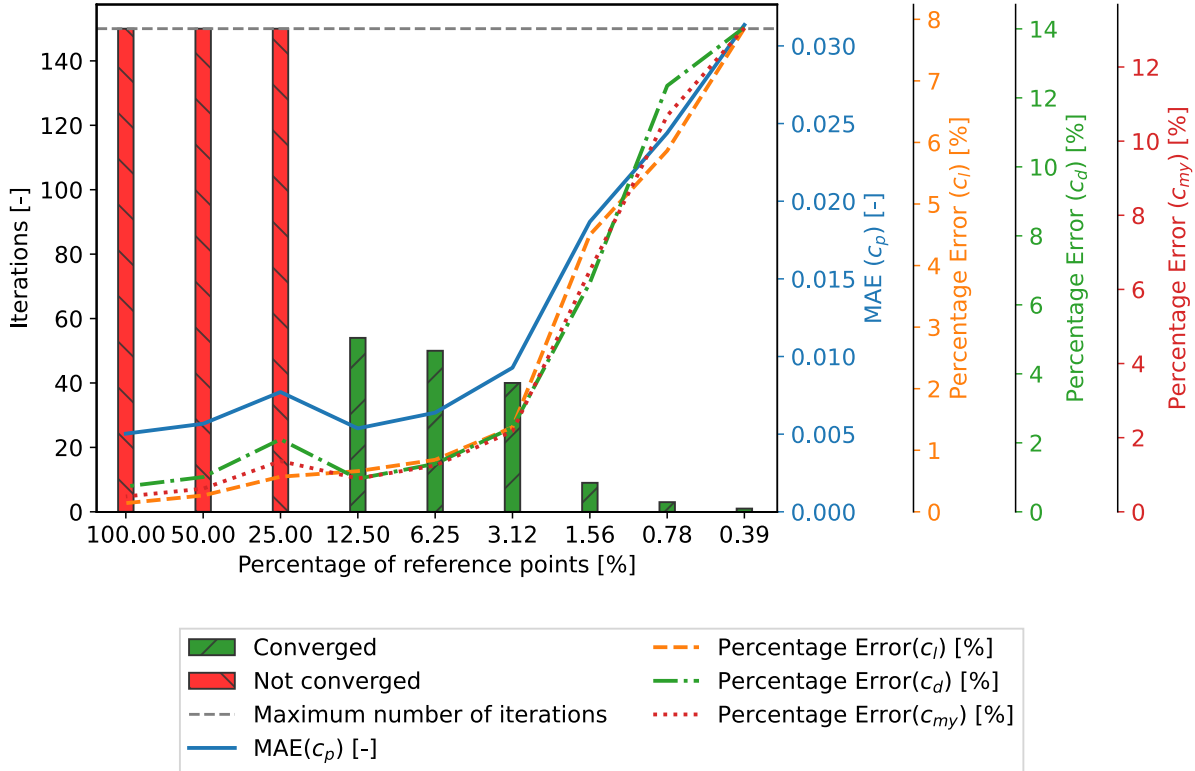


**Figure 4.7:** Influence of the number of reference points used for field inversion on a numerical test case (baseline: SA; reference: RSM) with flow conditions  $M = 0.75$ ,  $\alpha = 5.5^\circ$ ,  $Re = 6 \cdot 10^6$ , and regularisation  $\lambda = 10^{-12}$ . 512 reference points correspond to 100%.

Looking at a realistic application case the reference points are fixed in position for all angles of attack and therefore can not be adapted to a specific shock position. Furthermore, prior knowledge about the shock position can not be assumed in all cases. Concluding from the results of this investigation, the 12.50% case with 64 reference points is a good compromise between cost and accuracy. The next smaller case with 32 reference points exhibits similar error values (see Figure 4.7). The number of pressure taps in an experimental setting might lie in this range. Based on these findings 64 reference points are used in the further progress of this thesis.

### Effect on other Quantities

The prior investigation has proven that an FI with  $c_p$  as reference quantity can lead to an improved  $c_p$  distribution and an improvement of the values that are most strongly affected by  $c_p$ , e.g. the coefficient of lift. Thus, the question arises how other quantities are affected. As  $c_d$  is also influenced by the skin friction coefficient  $c_f$  this variable is of interest and makes a suitable example.

Subfigure 4.9b presents the skin friction coefficient around the airfoil for the baseline, the reference, and the inversion at  $\alpha = 5.0^\circ$ . The baseline and reference solutions show a mismatch regarding the shock position and the upper surface skin friction coefficient behind the shock. The FI can correct the position of the shock. However, behind the shock, the FI result matches the baseline solution. For both, baseline and reference

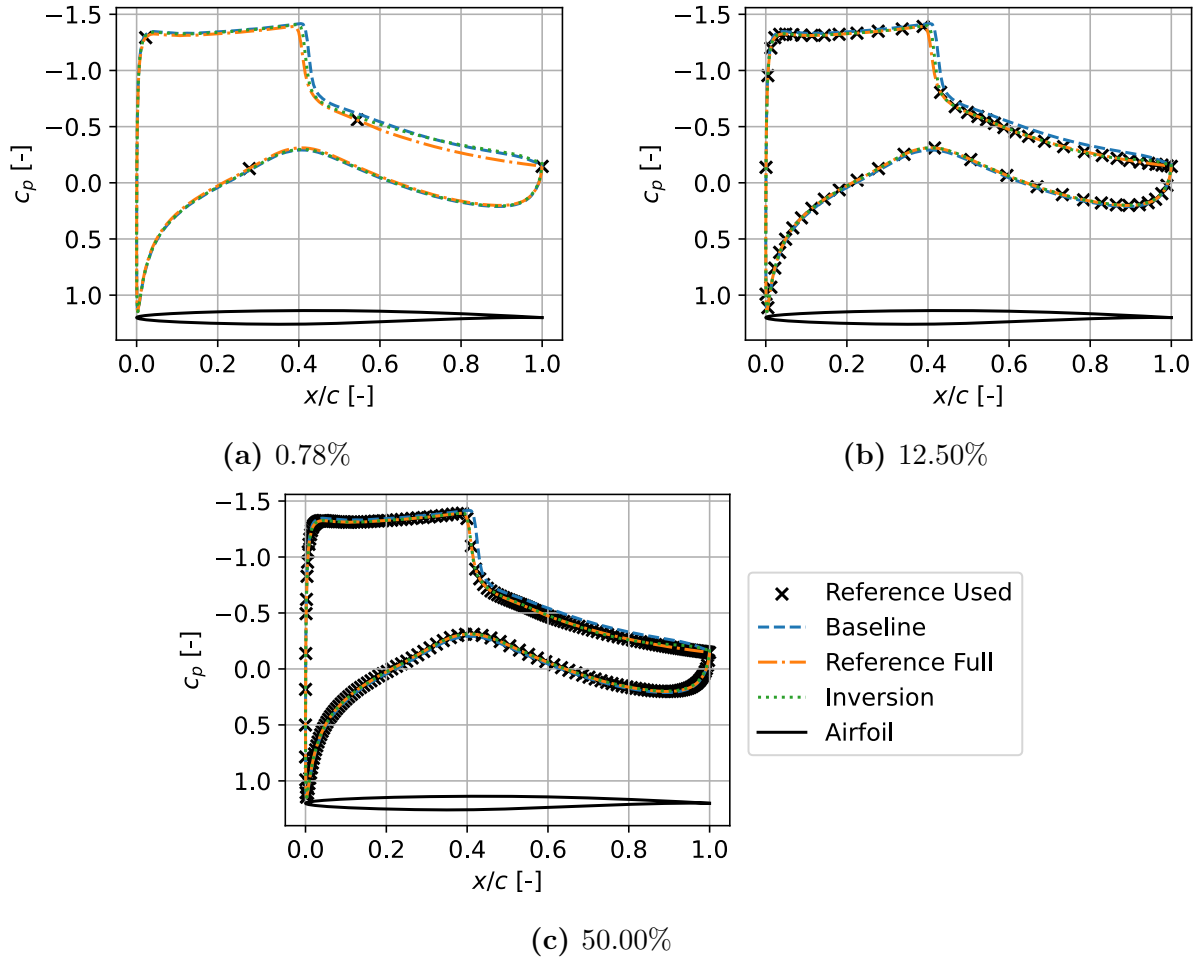


**Figure 4.8:**  $c_p$ -distributions on airfoil surface comparing FIs with different numbers of reference points at  $\alpha = 5.5^\circ$ . The legend of Subfigure 4.8c applies to all three cases.

solution  $c_f \leq 0$  can be observed behind the shock and corresponds to a separated flow. Thus, the FI result is quantitatively wrong but qualitatively right.

At  $\alpha = 3^\circ$ , the reference solution exhibits a small, reattaching flow separation at  $x/c \approx 0.6$ , whereas the baseline solution is fully detached after the shock. Again, the FI correctly shifts the shock position forward. As previously, the FI result matches the baseline solution behind the shock. Consequently, in this case, the result is wrong quantitatively and qualitatively.

Depending on the purpose of an FIML model, these findings must be paid attention to. A possible mitigation of the unsatisfying results could be to use  $c_f$  as an additional reference quantity. However,  $c_f$  is typically not measured in experiments.

### Further Findings and Limitations

The previously investigated cases only show small differences. Furthermore, the shock is moved forward in all cases. So the question arises of how the FI handles cases with larger differences and cases where the shock in the reference lies behind the baseline. Two synthetic test cases are designed to investigate these questions. For case 1, an SA simulation at  $\alpha = 3.5^\circ$  is corrected with an RSM simulation at  $\alpha = 5.5^\circ$ . In this case, the

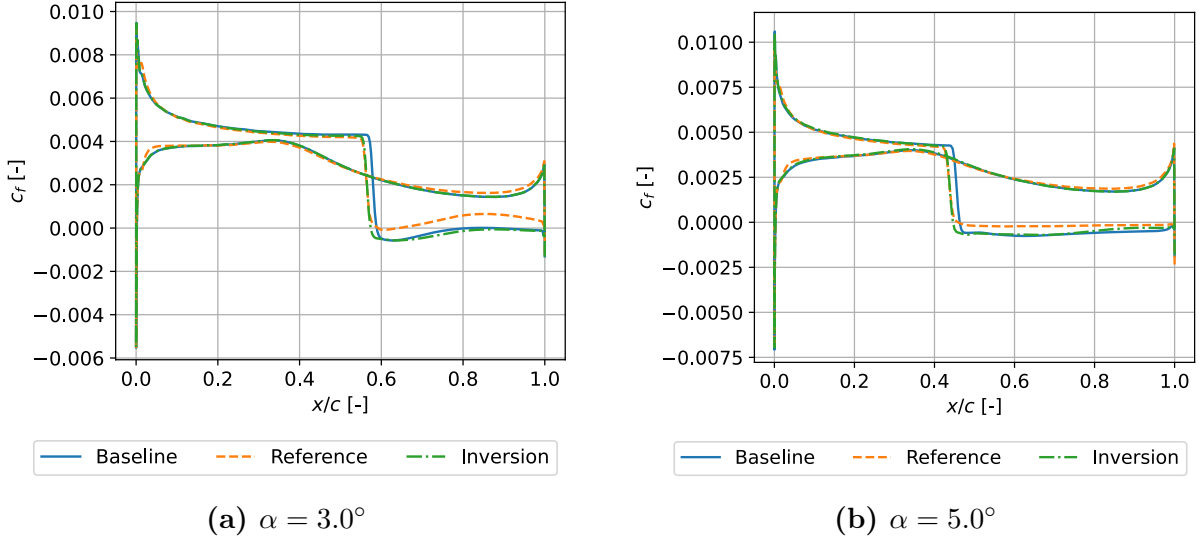
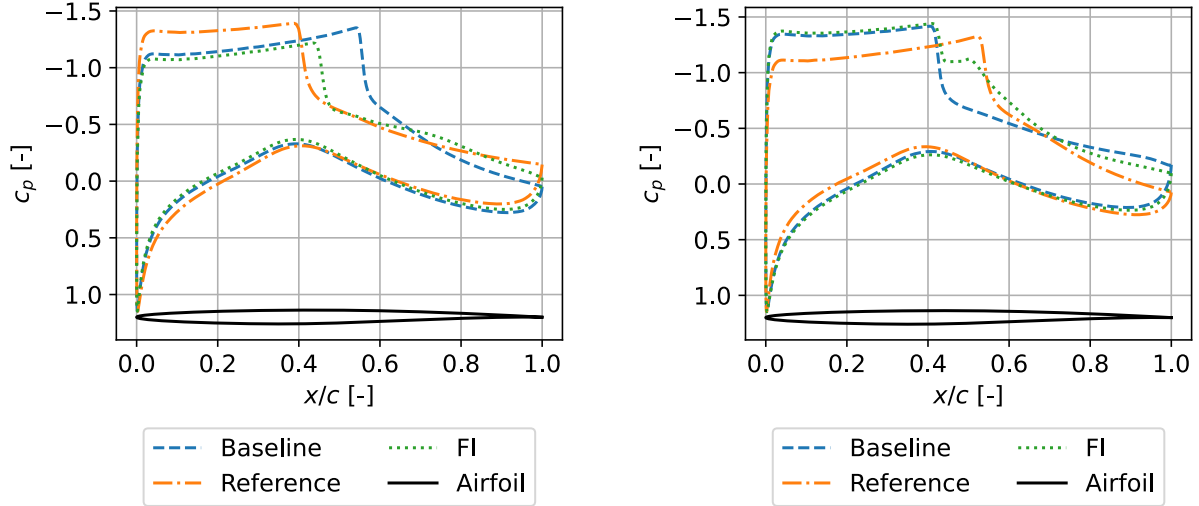


**Figure 4.9:**  $c_f$ -distributions on airfoil surface comparing SA (baseline) and RSM (reference) and FI result.

shock must be moved forward. Case 2 uses an SA simulation at  $\alpha = 5.5^\circ$  as the baseline that is corrected with an RSM at  $\alpha = 3.5^\circ$  as reference. To limit computational effort, for both cases, the FI is limited to 100 iterations. While case 1 reached convergence, case 2 did not. Nevertheless, the results are investigated.



**(a)** Case 1: Baseline is SA at  $\alpha = 3.5^\circ$  and reference is RSM at  $\alpha = 5.5^\circ$ . **(b)** Case 2: Baseline is SA at  $\alpha = 5.5^\circ$  and reference is RSM at  $\alpha = 3.5^\circ$ .

**Figure 4.10:** Synthetic test cases with baseline and reference solution from different angles of attack.

Figure 4.10 presents the resulting  $c_p$ -distributions of the FIs for both cases. FI is capable to move the shock forward and handle larger differences. As Subfigure 4.10b shows the FI approach can also handle a shock in the reference solution that is placed further to the rear. The pressure distribution for this case exhibits a kink at the location of the shock in the baseline solution. A limitation of the FI approach that becomes clear is that no correction of the pre-shock pressure plateau is possible. The  $\beta$  correction is only influencing the

production term  $P$  of the SA turbulence model. The production of the baseline SA solution in Figure 4.11 can only be found at  $x/c > 0.45$  (compare Subfigure 4.10a). This corresponds to the post-shock region. In a subsonic flow, information can travel upstream, so it is still possible to influence the pre-shock region. However, the influence seems to be negligible. Consequently, the FI approach is not suitable for correcting differing stagnation pressures, e.g. caused by differing free-stream conditions.

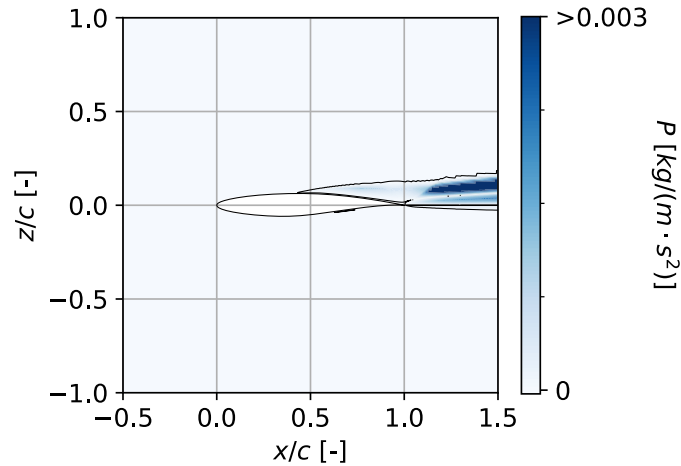


**Figure 4.11:** SA-production  $P$  for SA at  $\alpha = 5.5^\circ$ .

Another finding concerns the placement of reference points at selected locations only. Figure 4.12 presents a case at  $\alpha = 5.5^\circ$  with reference points at the rear end only. The FI result leads to a perfect result at the reference points. However, the shock is unlike the reference data located behind the baseline solution. The correction of isolated parts of the flow, e.g. the airfoil outflow, leads to diverging interests. This means that cases with strongly disagreeing interests regarding the correction variable must lead to strong local corrections.

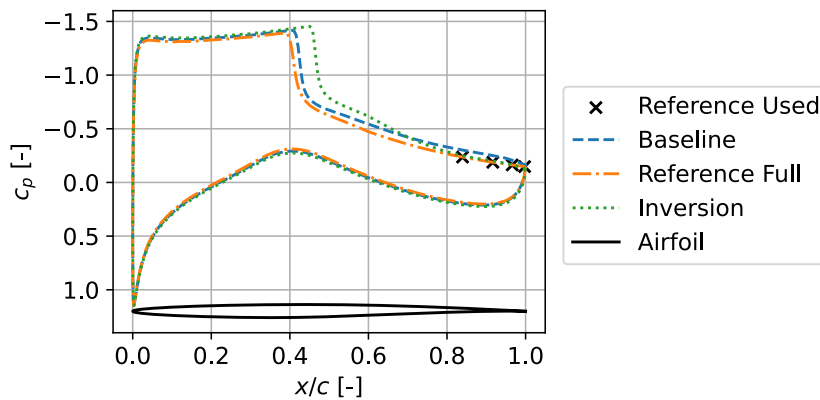


**Figure 4.12:**  $c_p$ -distributions on airfoil surface comparing FI with reference points at rear only to baseline and reference solutions.

## 4.2.2 Resulting Correction Fields

Based on the findings from subsection 4.2.1 FIs are executed. Therefore, the regularisation parameter  $\lambda$  must be chosen. Subsequently, the resulting correction fields can be analysed.

### Regularisation

The regularisation parameter  $\lambda$  defines the influence of the  $l_2$ -regularisation term  $\mathcal{I}_2$  in the cost function  $\mathcal{I}$  (see equation 3.4) and therefore the trust in the reference solution. A small  $\lambda$  reduces the influence of the regularisation and represents a high confidence in the reference solution.

An optimal value for the regularisation parameter can be determined using the L-curve criterion [62]. By plotting  $\mathcal{I}_1$  and  $\mathcal{I}_2$  in a log-log plot,  $\lambda_{\text{opt}}$  can be found at the curves inflection or elbow point. For  $\lambda < \lambda_{\text{opt}}$  the difference of the FI result to the reference ( $\mathcal{I}_1$ ) does not decrease significantly, whereas the modifications due to large  $\beta$ -values ( $\mathcal{I}_2$ ) increases strong and vice versa for  $\lambda > \lambda_{\text{opt}}$  [15].

Subfigure 4.13a presents the L-curve for  $\alpha = 2.5^\circ$  and Subfigure 4.13b the corresponding  $c_p$ -distributions for different  $\lambda$  values. According to the L-curve criterion  $\lambda_{\text{opt},2.5^\circ} = 10^{-10}$  is chosen. Baseline and reference solution as well as the solutions for different regularisations are close together when comparing the pressure distributions. However, the selected regularisation does lead to a good match of the reference points.

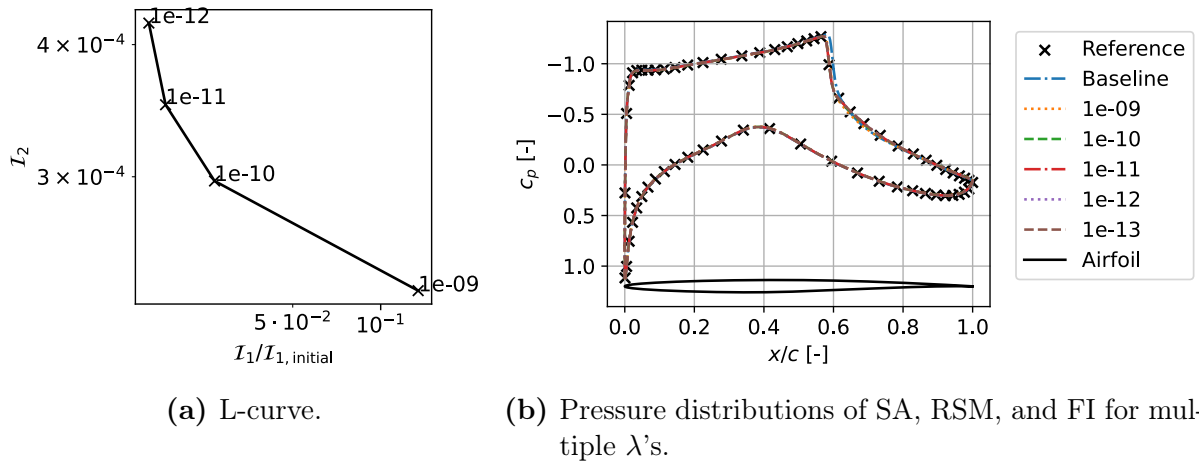


**Figure 4.13:** Selection criteria of regularisation at  $\alpha = 2.5^\circ$ .

In contrast to the previously depicted angle of attack, the L-curve criterion does not lead to a result for  $\alpha = 4.0^\circ$  as Subfigure 4.14a shows. Consequently, the optimal regularisation is chosen by a visual inspection of the  $c_p$ -distributions in Subfigure 4.14b.  $\lambda_{\text{opt},4.0^\circ} = 10^{-12}$  is chosen as no visual improvement can be seen for the next smaller value. Thus, the selected value yields a good compromise between matching the reference while still being regularised as much as possible.

Table 4.2 gives the resulting regularisation parameters at each angle of attack. It also denotes whether the values are selected by the L-curve criterion (L) or, in case this does not deliver clear results, whether the values are selected by comparing the  $c_p$ -distributions for multiple values of  $\lambda$ .

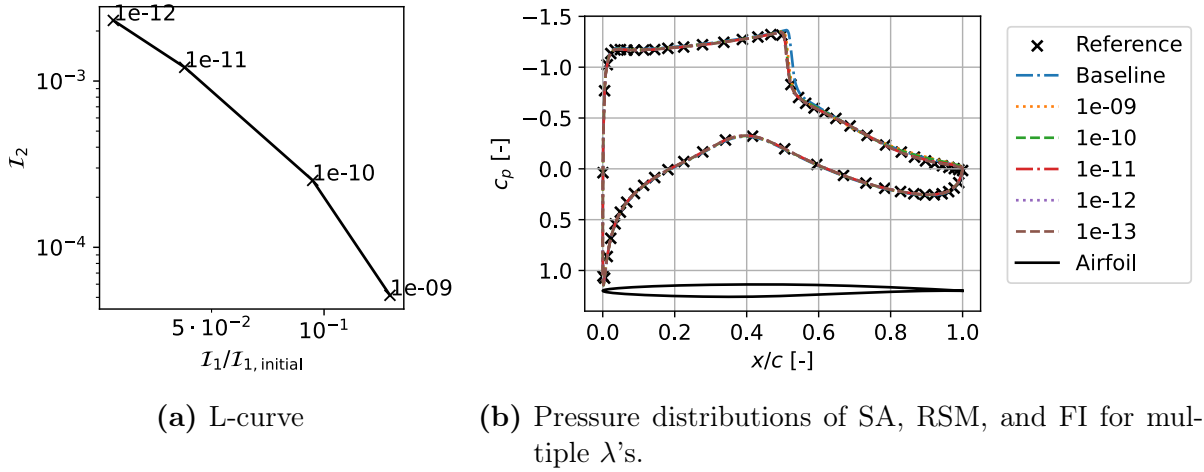


**Figure 4.14:** Selection criteria of regularisation at  $\alpha = 4.0^\circ$ .

$\alpha$ [deg]	0.0	0.5	1.0	1.5	2.0	2.5
$\lambda$ [-]	$10^{-12}$	$10^{-12}$	$10^{-12}$	$10^{-12}$	$10^{-12}$	$10^{-10}$
	S	S	S	S	S	L
$\alpha$ [deg]	3.0	3.5	4.0	4.5	5.0	5.5
$\lambda$ [-]	$10^{-10}$	$10^{-10}$	$10^{-12}$	$10^{-12}$	$10^{-12}$	$10^{-12}$
	L	L	S	S	S	S

**Table 4.2:** Selected values for  $\lambda$ . The letters in the last row denote selection by L-curve criterion (L) or selection by comparing  $c_p$ -distributions (S).

A further refinement of the tested values for  $\lambda$  would be possible and might lead to improved results. However, creating an L-curve is very costly as it requires computing multiple FIs. The resulting values in Table 4.2 are close together. Thus, when the investigation is repeated on another test case, it might be worth considering only choosing the optimal regularisation on a subset of angles of attack and choosing a default value that is applied to all cases.

## Analysis

Figure 4.15 presents the resulting correction field, a close-up of the correction field, and the distribution of the pressure coefficient on the airfoil surface for the FI results at  $\alpha = 1.5^\circ$  and  $\alpha = 4.5^\circ$ . Subfigures 4.15a and 4.15b show that most of the computational domain is not corrected by the FI, resulting in  $\beta \approx 1$ . Deviations from the baseline SA model can be found close to the airfoil, especially on the rear upper surface, and in the wake. The wake exhibits a periodic structure with alternating correction values above and below unity. The  $c_p$ -distributions in subfigures 4.6a and 4.6b exhibit matching reference, baseline, and FI solutions on the entire lower surface and the upper surface before the shock. At both angles of attack, the shock is correctly moved forward by the FI. As for  $\alpha = 1.5^\circ$ , no further deviations than the shock location are present between the baseline and the reference solution, the entire corrections must belong to the correction of the shock. Subfigure 4.15c visualizes that  $\beta < 1$  behind the shock: the turbulence production is decreased. A more complex  $\beta$ -field can be seen for  $\alpha = 4.5^\circ$  in Subfigure 4.15d. At this angle of attack, a mismatch between reference and baseline solution in the entire

post-shock region can be seen. The FI gives a good correction except very close to the trailing edge, where it falls back to the baseline surface pressure distribution. However, the more complex correction field at this angle of attack is due to the larger differences.

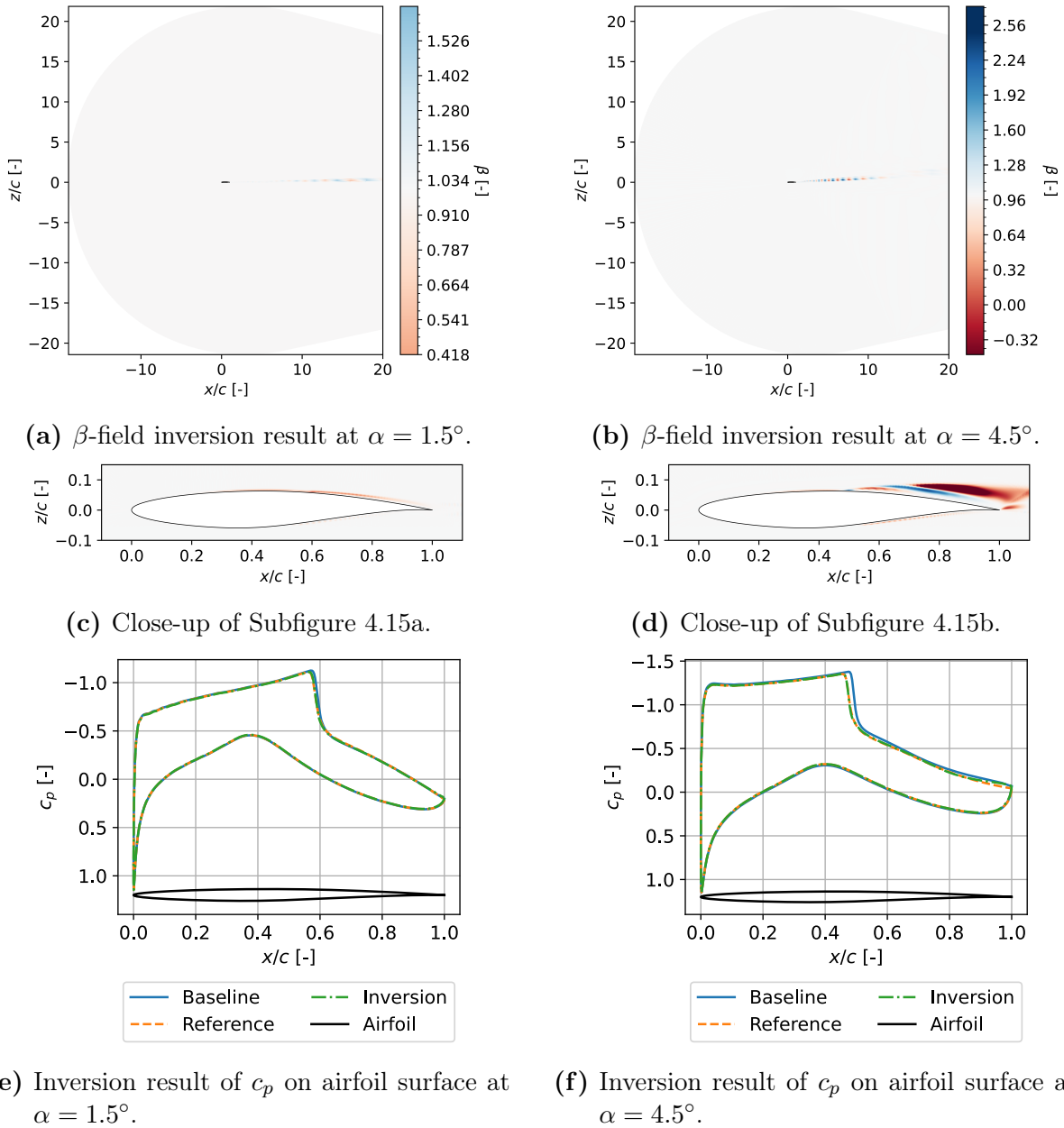


**Figure 4.15:** Inversion results at  $\alpha = 1.5^\circ$  and  $\alpha = 4.5^\circ$ . The  $\beta$ -fields use the same colour range. For the close-ups, the colours are amplified.

Figure 4.16 depicts how the correction affects the global force coefficients  $c_l$ ,  $c_d$ , and  $c_{my}$ . A good correction can be seen at all angles of attack for all three coefficients. It must be noted that even though the drag is influenced by the skin friction, which is according to Figure 4.9 not corrected by the FI, the corrected values are very close to the reference solution. While the correction of the drag coefficient only leads to a quantitative improvement, lift and moment coefficients show a qualitative and quantitative correction. For the baseline solution lift is increasing monotonously with the angle of attack, while for the reference solution a slight decline of lift for large  $\alpha$  can be seen. Thus, the maximum lift  $c_{l,\max}$  that defines the beginning of the stall region can be found. The longitudinal

stability of an aircraft is decisively influenced by the derivative by  $dc_{my}/d\alpha$ . While the SA model predicts a non-positive derivative at all angles of attack, the FI correctly leads to a change in gradient similar to the RSM solution.

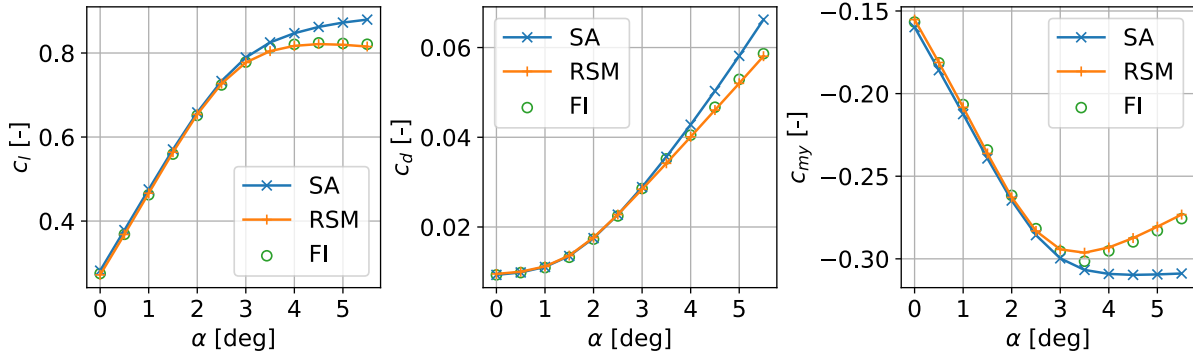


**Figure 4.16:**  $c_l$  (left),  $c_d$  (middle), and  $c_{my}$  (right) over  $\alpha$  for  $M = 0.75$   $Re = 6.0 \cdot 10^6$  comparing SA, RSM, and FI.

## 4.3 Machine Learning

In section 4.2 the FI produces correction fields that improve RANS simulations by multiplying the correction term  $\beta$  with the production term  $P$  of the SA turbulence model. This section aims to establish a functional relationship of the mean flow variables to the correction term enabling a prediction on unseen cases.

First, the dataset is described and investigated in subsection 4.3.1. Subsequently in subsection 3.4.3, possible flow features are evaluated. Using generic models, different considerations regarding the dataset and the features are compared in subsection 4.3.3. Finally, the hyperparameters of the best model are optimised in subsection 4.3.4.

### 4.3.1 Dataset

For 12 angles of attack, a correction field with  $\beta$  as a spatially distributed variable is available. With 82 624 nodes in the mesh this results in 991 488 data points. The histogram in Figure 4.17 presents the number of occurrences of values for  $\beta$ . It becomes clear that  $\beta \approx 1$  is severely overrepresented. This finding can be confirmed by looking at the correction fields in 4.2.2:  $\beta \neq 1$  values are only present in certain areas on the airfoil surface and the wake.

An integral part of ML models is minimizing a loss function between true and predicted values. However, if one value is strongly overrepresented the ML model *learns* that predicting the overrepresented value, e.g.  $\beta \approx 1$ , results in a small value for the loss function. Thus, strategies to mitigate this problem must be found. One option is to use a problem-specific cost function that applies weight to underrepresented values. However, in this thesis two different ways to manipulate the dataset are taken into account: an areal selection of certain mesh nodes, and a reduction of values close to  $\beta = 1$ .

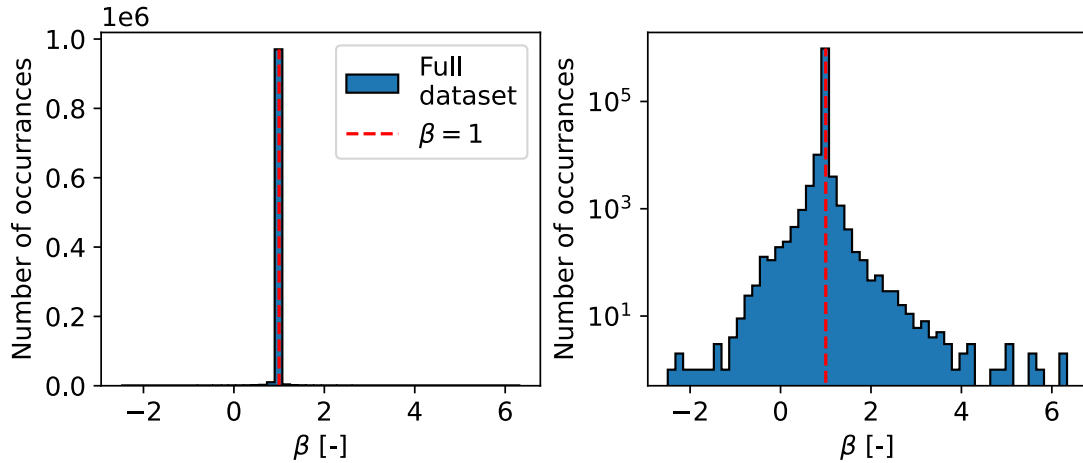
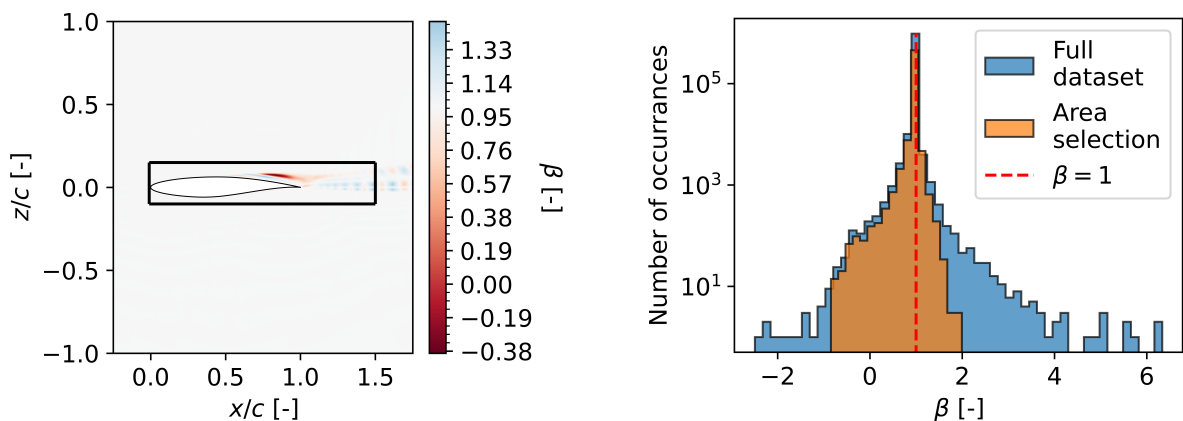


**Figure 4.17:** Number of occurrences of  $\beta$  in the available data (left). Same figure with the logarithmic y-axis (right).

### Area Selection

The FI results in a correction term for each node in the computational domain. However, Jäckel concludes that the quantities of interest, i.e.  $c_p$ ,  $c_l$ ,  $c_d$ , and  $c_{my}$ , are mostly influenced by the corrections in certain areas [15]. Whereas the referenced study distinguishes different areas on the airfoil, here a more robust selection is done: based on a visual investigation of the available data, a rectangular area with  $-0.01 \leq x/c \leq 1.5$  and  $-0.1 \leq z/c \leq 0.15$  is defined. Nodes located in the defined area are selected for the ML model training. Figure 4.18 gives a visual representation of this approach and shows the resulting number of  $\beta$  occurrences for  $\alpha = 4.5^\circ$ . The selected area contains 47.5% of all nodes. It becomes clear that this approach does not only result in a reduction of values close to 1 but also removes the most extreme values. The highest correction values can be found in the wake outside the selected area.



(a) Correction field with selected area for  $\alpha = 4.5^\circ$ . (b) Resulting occurrences of  $\beta$  when applying area selection to entire dataset.

**Figure 4.18:** Visual representation and the result of area selection.

To evaluate the influence of the selection, the results of steady simulations using the full and the selected correction field are compared. The mean absolute percentage error

(MAPE) of the integral force and moment coefficients  $c_l$ ,  $c_d$ , and  $c_{my}$  is computed:

$$\begin{aligned} \text{MAPE}(c_l) &= 9.89 \cdot 10^{-5}\% \\ \text{MAPE}(c_d) &= 1.43 \cdot 10^{-3}\% \\ \text{MAPE}(c_{my}) &= 12.86 \cdot 10^{-4}\% \end{aligned}$$

Only very small deviations are caused by the area selection approach. Furthermore, training an ML model with less data are faster. Consequently, the approach is considered for further work in this thesis.

### Reduction of $\beta \approx 1$

Adaptive sampling is another strategy proposed in multiple publications concerning the FIML approach that might be used to mitigate the problem of imbalanced datasets [16, 63]. Based on the  $\beta$  value of a sample the likelihood of being included in the dataset is determined. In this thesis, a simple approach is used: only a given percentage of the values in the range  $0.99 \leq \beta \leq 1.01$  is included. Figure 4.19 presents the resulting  $\beta$ -distributions for three percentages.

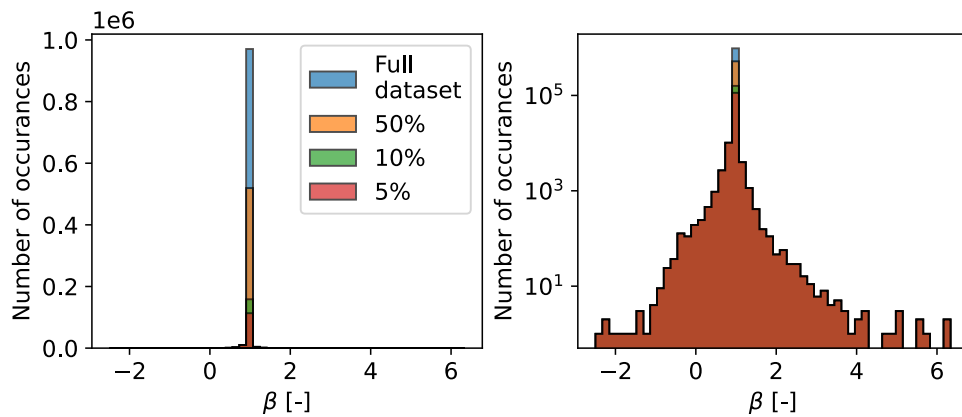


**Figure 4.19:** Number of occurrences of  $\beta$  after reducing the values  $0.99 < \beta < 1.01$  (left). Same figure with the logarithmic y-axis (right).

### 4.3.2 Feature Selection

In section 3.4.3 five features are introduced. These features are investigated as initial features regarding their value range and correlation. As tests on a generic model in subsection 4.3.3 show, the initial features are not sufficient, further features are selected and also investigated.

For the subsequent evaluations the data from all angles of attack, except  $\alpha = 1.5^\circ$  and  $\alpha = 4.5^\circ$ , are aggregated and analysed. The excluded cases are later used as test cases and therefore should not influence the feature selection.

#### Initial Features

As other studies have shown, the feature values might span over multiple orders of magnitude [16]. This is unfavourable for many ML models because the features are usually scaled before being used in most ML approaches. Consequently, a large portion of the

samples would concentrate on a similar feature value. Applying a logarithm to a feature with such a distribution can mitigate this issue. Figure 4.20 shows the distribution of  $\eta_1$  before and after the application of a logarithm. However, the logarithm does not return finite values for all sample points. In the case of  $\log(\eta_1)$  17.7% of the values are infinite and unusable for an ML model. Thus, these sample points are removed from the dataset. However, this also leads to a loss of information.

Similar results can be seen for the remaining features. For conciseness, the distributions are not shown. The logarithm is applied to all of the five initial features.

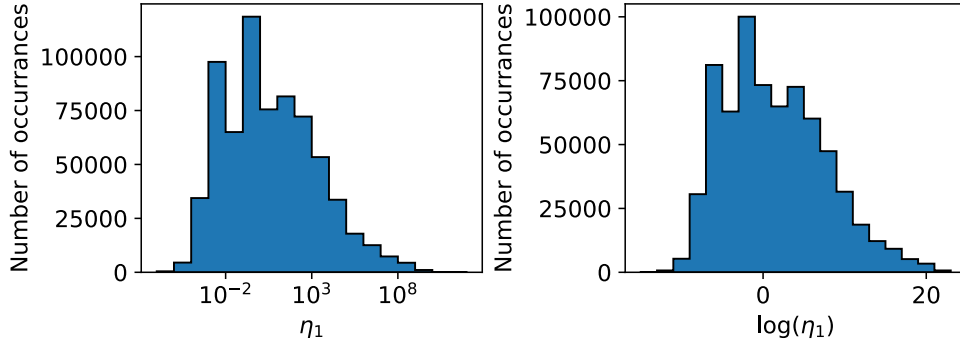


**Figure 4.20:** Distribution of  $\eta_1$  before (left) and after (right) applying a logarithm.

### Further Features

Further features are investigated. The listed features are chosen due to their availability in the field solution. Three differently important requirements are stated in subsection 3.4.3. The local availability is mandatory, as the ML model expects a fixed number of inputs. Dimensionless features are not necessary for ML models, but this way consistency of dimensions is ensured. Non-dimensional features can be ensured by dividing the selected variable with the free-stream variables of the same dimension. GALILEAN invariance is the most restrictive requirement, as it prohibits many variables. With GALILEAN invariance ensured, the model can be applied regardless of the inertial reference frame. This is not true for features that contain a velocity, since the velocity would be different in a steadily moving reference frame. However, the main goal of this thesis is not to build a model that is applicable in all conditions but to investigate whether the model can be applied to unsteady simulations. Thus, not all of the features satisfy this requirement. The investigated features are listed below:

- $\eta_6 = \frac{\rho}{\rho_\infty}$ : ratio of density to free-stream density.
- $\eta_7 = \frac{\mu_t}{\mu}$ : ratio of dynamic eddy viscosity to dynamic viscosity.
- $\eta_8 = M$ : local MACH number.
- $\eta_9 = c_p$ : pressure coefficient.
- $\eta_{10} = \frac{p_t}{p_\infty}$ : ratio of total pressure to free-stream pressure.
- $\eta_{11} = \frac{u_\tau}{|\mathbf{u}_\infty|}$ : ratio of friction velocity at nearest wall point to free-stream velocity.
- $\eta_{12} = \frac{u_x}{|\mathbf{u}_\infty|}$ : ratio of velocity in x-direction to free-stream velocity.
- $\eta_{13} = \frac{u_z}{|\mathbf{u}_\infty|}$ : ratio of velocity in z-direction to free-stream velocity.

- $\eta_{14} = \frac{\rho u_x}{\rho_\infty |\mathbf{u}_\infty|}$ : ratio of x-momentum to free-stream momentum.
- $\eta_{15} = \frac{\rho u_z}{\rho_\infty |\mathbf{u}_\infty|}$ : ratio of z-momentum to free-stream momentum.
- $\eta_{16} = \left| \frac{dp}{dx} \right| / \frac{p_\infty}{l_{\text{ref}}}$ : magnitude of pressure gradient in x-direction non-dimensionalised with pressure over REYNOLDS reference length.
- $\eta_{17} = \left| \frac{dp}{dz} \right| / \frac{p_\infty}{l_{\text{ref}}}$ : magnitude of pressure gradient in z-direction non-dimensionalised with pressure over REYNOLDS reference length.

Features  $\eta_{16}$  and  $\eta_{17}$  exhibit numerous negative values. Thus, the magnitude is used to be able to apply a logarithm without losing too many samples.

### Summary and Evaluation

Table 4.3 summarizes all features and shows whether a feature satisfies GALILEAN invariance, whether, based on a visual inspection, a logarithm should be applied, and how many samples must be removed due to the application of the logarithm. Each sample that contains a non-finite feature is removed. Overall, 17.7% of the samples are removed.

Feature	$\eta_1$	$\eta_2$	$\eta_3$	$\eta_4$	$\eta_5$	$\eta_6$	$\eta_7$	$\eta_8$	$\eta_9$
Galilean invariance	✓	✓	✓	✓	✓	✓	✓	X	X
log	✓	✓	✓	✓	✓	X	✓	X	X
Removed samples [%]	17.7	1.5	0	1.5	0.8	0	1.5	0	0

Feature	$\eta_{10}$	$\eta_{11}$	$\eta_{12}$	$\eta_{13}$	$\eta_{14}$	$\eta_{15}$	$\eta_{16}$	$\eta_{17}$
Galilean invariance	X	X	X	X	X	X	X	X
log	X	X	X	X	X	X	✓	✓
Removed samples [%]	0	0	0	0	0	0	0	0

**Table 4.3:** Features to be investigated. Row GALILEAN invariance shows whether this requirement is satisfied. The row log shows if a logarithm should be applied. Removed samples show the number of samples removed due to the application of the logarithm.

The features are evaluated regarding their correlation with each other and with the target value. Three correlation coefficients as introduced in 3.4.3 are compared. Figure 4.21 presents SPEARMAN’s rank correlation between all features and the target. Similar plots for the PEARSON correlation (see Figure A.1) and the distance correlation (see Figure A.2) can be found in the Appendix A.

Across all three metrics, none of the features shows a really strong correlation to the target. However, only  $\eta_{17}$  has a correlation of less 0.1 on all three metrics. As this is an indication that this feature is not beneficial for an ML model, it is removed. A high correlation between two features indicates that not both features are necessary as they deliver similar information. Here, all feature pairs that have a correlation of above 0.9 or below  $-0.9$  for all three correlation coefficients are listed:

- $\eta_1$  and  $\eta_5$ : as due to  $\eta_1$  17.7% of the samples are removed (see Table 4.3) it should be removed.
- $\eta_6$  and  $\eta_9$ : as  $\eta_9$  does not satisfy GALILEAN invariance and exhibits smaller correlation with  $\beta$  it is removed.

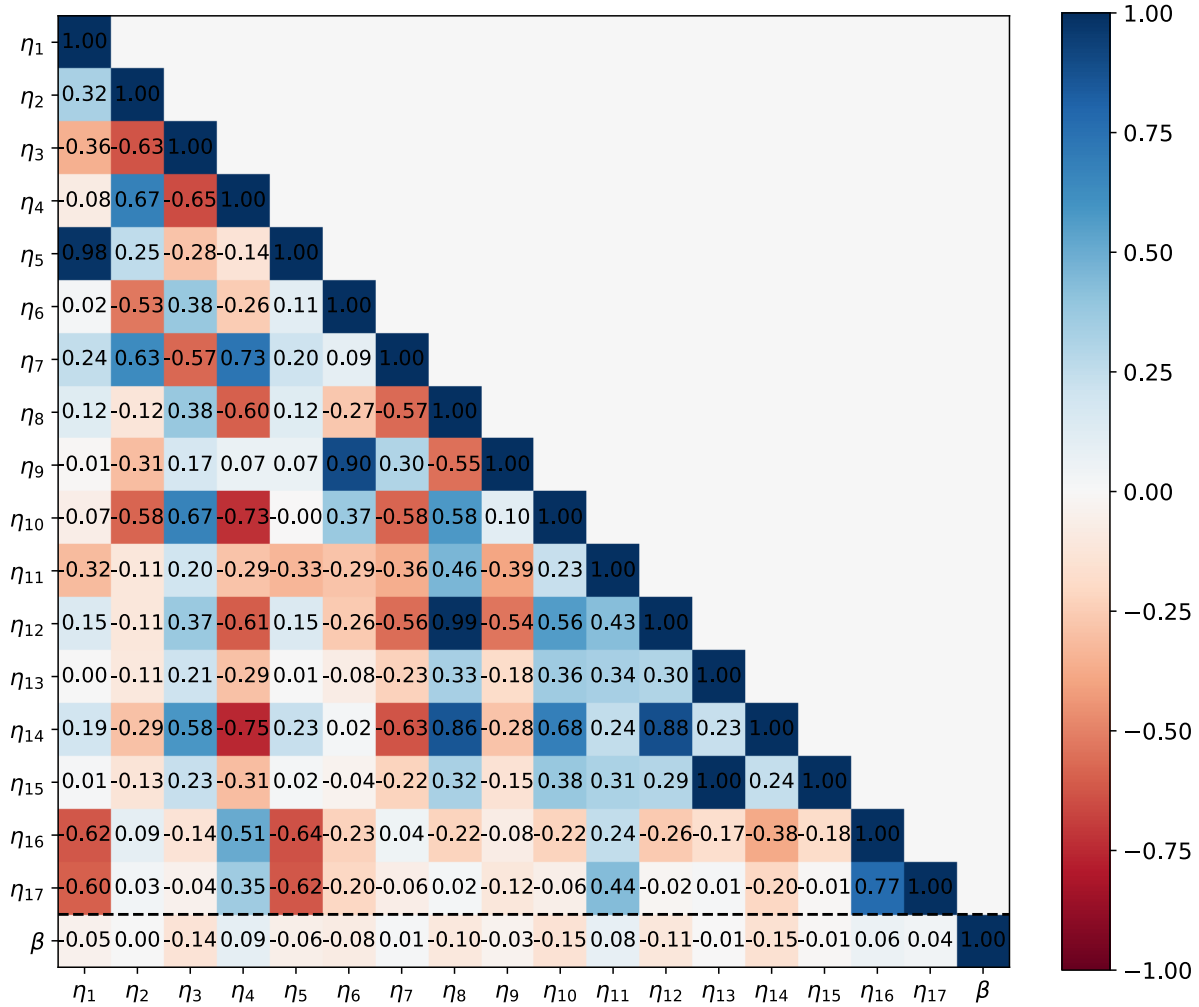


**Figure 4.21:** Spearman's rank correlation coefficient between all features and the target.

- $\eta_8$  and  $\eta_{12}$ : both features show similar correlation with the target.  $\eta_8$  is directly available in the solution and is kept.
- $\eta_{13}$  and  $\eta_{15}$ : both show similar performance,  $\eta_{13}$  is kept.

The presented considerations are based on the correlations only. However, it is also possible to find causal explanations:  $\eta_8 = M$  is the ratio of the local flow velocity to the speed of sound.  $\eta_{12}$  is the ratio of the velocity in the x-direction to the free-stream velocity. For the present simulations, the free-stream velocity and the speed of sound are fixed. Furthermore, the flow is moving fast in the x-direction. Thus, the z-component is very small. Consequently, both features describe a very similar value: the flow velocity in the x-direction.

Four possible sets of features are used for the ML model training. The initial features only, all features, the features that are selected after evaluating the correlation coefficients, and

a subset of the latter that only contains features that are GALILEAN invariant:

$$\boldsymbol{\eta}_{\text{initial}} = \{\eta_1, \eta_2, \eta_3, \eta_4, \eta_5\} \quad (4.2)$$

$$\boldsymbol{\eta}_{\text{all}} = \{\eta_1, \eta_2, \eta_3, \eta_4, \eta_5, \eta_6, \eta_7, \eta_8, \eta_9, \eta_{10}, \eta_{11}, \eta_{12}, \eta_{13}, \eta_{14}, \eta_{15}, \eta_{16}, \eta_{17}\} \quad (4.3)$$

$$\boldsymbol{\eta}_{\text{selection}} = \{\eta_2, \eta_3, \eta_4, \eta_5, \eta_6, \eta_7, \eta_8, \eta_{10}, \eta_{11}, \eta_{13}, \eta_{14}, \eta_{16}\} \quad (4.4)$$

$$\boldsymbol{\eta}_{\text{Galilean}} = \{\eta_2, \eta_3, \eta_4, \eta_5, \eta_6, \eta_7\} \quad (4.5)$$

### 4.3.3 Generic Test Models

In this subsection two regression models, one based on radial basis functions (RBF) and one based on a fully-connected neural network (FCNN), are used to test the influence of manipulations of the dataset and the features. First, three test metrics are introduced, before two generic models are evaluated. For test purposes the data at two angles of attack are used:  $\boldsymbol{\alpha}_{\text{test}} = \{1.5^\circ, 4.5^\circ\}$ . These data are selected as they represent one case from the linear region of the  $\alpha$ - $c_l$  curve and one case from the non-linear region (see Figure 4.5). The remaining angles of attack can be used for training purposes. Two sets are defined to evaluate the influence of the amount of training data:  $\boldsymbol{\alpha}_{\text{train, small}} = \{0.0^\circ, 1.0^\circ, 2.0^\circ, 3.0^\circ, 4.0^\circ, 5.0^\circ\}$  and  $\boldsymbol{\alpha}_{\text{train, large}} = \{0.0^\circ, 0.5^\circ, 1.0^\circ, 2.0^\circ, 2.5^\circ, 3.0^\circ, 3.5^\circ, 4.0^\circ, 5.0^\circ, 5.5^\circ\}$ .

#### Test Metrics

Three metrics are used to compare the predicted values  $\boldsymbol{\beta}_{\text{pred}} \in \mathbb{R}^n$  to the true values  $\boldsymbol{\beta}_{\text{true}} \in \mathbb{R}^n$ , where  $n$  is the number of samples. The following descriptions are based on [64].

The coefficient of determination  $R^2$  is a measure for the proportion of the variance of  $\boldsymbol{\beta}_{\text{true}}$  that is explained by the model. A perfect prediction yields 1.0, while a model that predicts the mean of true value regardless of the input has a score of 0.0. Negative scores are possible if the model is arbitrarily worse. With  $\overline{\beta_{\text{true}}}$  the arithmetic mean of  $\boldsymbol{\beta}_{\text{true}}$  it is defined as

$$R^2(\boldsymbol{\beta}_{\text{true}}, \boldsymbol{\beta}_{\text{pred}}) = 1 - \frac{\sum_{i=1}^n (\beta_{\text{true},i} - \beta_{\text{pred},i})^2}{\sum_{i=1}^n (\beta_{\text{true},i} - \overline{\beta_{\text{true}}})^2}. \quad (4.6)$$

The mean absolute error (MAE) is the arithmetic mean of the  $l_1$ -norm loss and defined as

$$\text{MAE}(\boldsymbol{\beta}_{\text{true}}, \boldsymbol{\beta}_{\text{pred}}) = \frac{1}{n} \sum_{i=1}^n |\beta_{\text{true},i} - \beta_{\text{pred},i}|. \quad (4.7)$$

Similar to the MAE, the mean squared error (MSE) is the arithmetic mean of the  $l_2$ -norm loss. In contrast to the MAE, it is more sensitive to outliers. The following equation gives a definition:

$$\text{MSE}(\boldsymbol{\beta}_{\text{true}}, \boldsymbol{\beta}_{\text{pred}}) = \frac{1}{n} \sum_{i=1}^n (\beta_{\text{true},i} - \beta_{\text{pred},i})^2. \quad (4.8)$$

### Radial Basis Function Regression

The first model that is tested is an RBF regression model as introduced in 3.4.4. The plan is to use the training dataset  $\alpha_{\text{train, small}}$  with the features  $\alpha_{\text{initial}}$  to initially compare the RBF model and the FCNN model that is described in the next paragraph. However, fitting an RBF model requires computing a matrix of size  $\mathbb{R}^{n,n}$  with  $n$  the number of sample points. This exceeds the computational infrastructure that is accessible to the author. Thus,  $\alpha_{\text{train, RBF}} = \{1.0^\circ, 4.0^\circ\}$  is used instead. Several layouts, including varying augmentation parameters, regularisations, and basis functions are investigated. However, no satisfactory results are achieved. The results of one exemplary model are presented.

An RBF based on a thin plate spline according to  $\varphi = r^2 \ln(r)$  is used. The regularisation at each sample location is set to  $10^{-8}$ . No trend function is added to the RBFs [47]. Thus, for a point far away from a sample point the resulting value of the regression function is 0. Consequently, the model is fitted to predict  $\beta - 1$ , because this enforces a prediction of  $\beta = 1$ , i.e. an unchanged turbulence model, at locations far away from the sample points. The resulting metrics on the training and test data are summarised in Table 4.4. The model gives near-perfect predictions on the training data but is not able to generalize on the test cases. Additional investigations might deliver further insights and improvements. However, since the FCNN which is presented next, delivers much more promising results, the RBF approach is not being investigated further.

	Training			Test		
	$R^2$	MAE ·10 <sup>5</sup>	MSE ·10 <sup>8</sup>	$R^2$	MAE ·10 <sup>2</sup>	MSE ·10 <sup>2</sup>
exemplary RBF	0.999	4.00	3.91	-3.123	2.28	1.58

**Table 4.4:** Resulting scores for presented RBF model.

### Fully-Connected Neural Network

A fully-connected neural network according to subsection 3.4.4 is investigated to see whether it can capture the structures in the data. To test the capabilities, a generic model with four hidden layers is used. The four layers contain 100, 85, 70, and 55 neurons with ReLU activation functions each. With a dropout rate of 0.1, 10% of the neurons in each layer are deactivated at each training step to prevent overfitting. In- and outputs are scaled linearly to a range between 0 and 1. During network training, the mean squared error (MSE) between predicted and true target values is used as a loss function to update the model parameters.

The model is trained using the gradient-based optimisation algorithm Adam with SMARTy default settings [47, 65]. The initial learning rate is multiplied with a factor of 0.1 after 1000, 2000, and 3000 training epochs. 30% of the training data are selected randomly to be used as validation data. The training is conducted in batches of 4096 samples. Finally, the training is stopped after 4000 epochs or in case an early stopping criterion is fulfilled: if the mean absolute error (MAE) between the predicted and true value on the validation data does not improve for 500 epochs, the training is stopped.

Training the model on the  $\alpha_{\text{train, small}}$  using the features  $\eta_{\text{initial}}$  results in the metrics presented in the first row of the Table 4.5. Figure 4.22 visualizes the predictions of the ML model for the training and test samples. Even though the predictions are far from perfect the

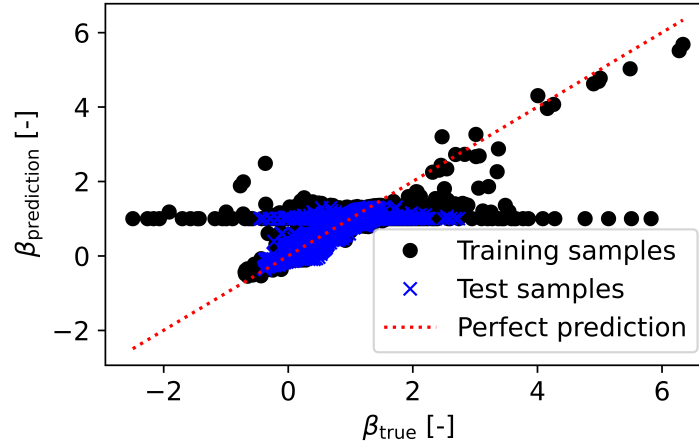


**Figure 4.22:** Predicted versus true target values from training and test data for FCNN no. 1.

figure shows that the FCNN is capable of capturing underlying structures in the data. It must be mentioned that a  $\beta_{\text{prediction}} \approx 1$  is vastly overrepresented.

### Systematic Model Evaluation

The previous paragraph shows that an FCNN can capture the given data to some extent, but is far from satisfactory. Subsections 4.3.1 and 4.3.2 present considerations regarding the feature selections and manipulations of the dataset. Using the presented generic FCNN model, the influence of the individual approaches is evaluated. Based on the baseline result present in the previous paragraph (Table 4.5, no. 1) changes are done systematically, i.e. in contrast to a full factorial test, the influence of changes of individual variables is tested, but not all combinations.

First, similar to case no. 1, using  $\alpha_{\text{train,small}}$ , the feature sets  $\eta_{\text{all}}$ , and  $\eta_{\text{selection}}$  are evaluated (no. 2 and 3):  $\eta_{\text{selection}}$  is the best set of features as it performs better on all training and test metrics except the coefficient of determination on the training data.

Trials no. 4 to 9 evaluate the influence of manipulations on the dataset: applying no reduction, applying the area selection, applying a down selection of the samples with  $0.99 < \beta < 1.01$ , or applying a combination of the latter two. According to the metrics, an application of area selection only (no. 5) yields the best results.

For the previous trials, the validation samples are selected randomly from all training points. Trial no. 10 tests the hypothesis of whether it is beneficial to use the data from selected angles of attack exclusively for validation purposes to improve the capability of the network to generalize. The metrics must be compared to trial no. 9 and show that randomised validation data leads to better results.

The current best approach (no. 5) must also be trained on  $\eta_{\text{train,small}}$  as the smaller dataset leads to better results on the test data in direct comparison (no. 3 vs no. 4): Trial no. 11 presents the results of the small dataset using the area selection approach and exhibits promising metrics with an  $R^2$ -score of 0.967 on the training data and 0.898 on the test data.

No.	Dataset	Features	Training			Test		
			$R^2$	MAE $\cdot 10^3$	MSE $\cdot 10^3$	$R^2$	MAE $\cdot 10^3$	MSE $\cdot 10^3$
1	small, no reduction	$\boldsymbol{\eta}_{\text{initial}}$	0.511	6.45	2.19	0.574	7.57	1.63
2		$\boldsymbol{\eta}_{\text{all}}$	0.586	4.77	1.85	0.565	6.59	1.67
3		$\boldsymbol{\eta}_{\text{selection}}$		0.537	4.10	1.74	0.635	<b>5.35</b>
4	large, no reduction		0.631	4.33	1.28	0.607	5.51	1.25
5	large, area		0.942	4.13	0.22	0.884	6.73	5.42
6	large, 50%		0.575	7.36	2.68	0.524	5.42	1.51
7	large, 10%		0.637	19.91	6.80	0.608	5.82	1.24
8	large, 5%		0.624	26.25	9.32	0.576	6.30	1.34
9	large, area + 10%		0.944	13.06	0.85	0.867	7.85	0.62
10	large, area + 10% + sep. val.		0.927	14.92	1.16	0.814	9.92	0.87
11	small, area		<b>0.967</b>	<b>3.29</b>	<b>0.12</b>	<b>0.898</b>	6.67	<b>0.47</b>
12	small, area		$\boldsymbol{\eta}_{\text{Galilean}}$	0.942	4.19	0.21	0.700	9.57

**Table 4.5:** Influence of feature selection and dataset on generic FCNN. *small*: training data are  $\boldsymbol{\alpha}_{\text{train, small}}$ . *large*: training data are  $\boldsymbol{\alpha}_{\text{train, large}}$ . *no reduction*: dataset is not altered. *area*: area selection is applied. *x%*: only  $x\%$  of the samples with  $0.99 < \beta < 1.01$  are included. *sep. val.*: train and validation data are not split randomly (70%/30%), but  $\alpha = \{0.5^\circ, 2.0^\circ, 4.0^\circ\}$  are used for validation.

Finally, trial no. 12 investigates the outcome using only features that hold GALILEAN invariance. While the results on the training data do worsen only slightly, a strong degradation can be seen in the test data. Consequently, the additional non-GALILEAN invariant features contained in  $\boldsymbol{\eta}_{\text{selection}}$  benefit the generalisation.

#### 4.3.4 Hyperparameter Optimisation

The performance of an FCNN is significantly influenced by the network topology and how it is trained. Parameters that influence the mentioned areas are called hyperparameters. In contrast to those parameters that are updated during network training, i.e. weights and biases, the hyperparameters must be chosen to a fixed value before the network training. The generic FCNN in subsection 4.3.3 uses a set of arbitrarily chosen hyperparameters. By performing a hyperparameter optimisation (HPO) an optimised set of hyperparameters can be found.

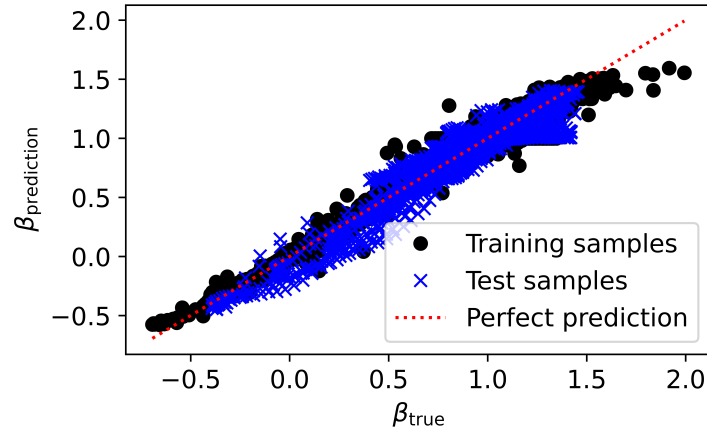


**Figure 4.23:** Predicted versus true target values from training and test data for FCNN no. 11.

Setting the minimisation of the MAE on the validation samples as the optimisation target, an HPO is performed using the Python library *optuna* [66]. The following hyperparameters are used as optimisation variables. Explanations are given for parameters that have not been introduced previously in this thesis:

1. Number of neurons in the first hidden layer.
2. Maximum number of hidden layers.
3. Shrinkage factor: factor defining the number of neurons in the subsequent hidden layers.
4. Dropout rate: number of neurons that are deactivated during training to improve generalisation.
5. Initial learning rate.
6. Gamma: a factor that is used to adapt the learning rate after a given number of steps that is defined by the milestone factor.
7. Milestone factor: defines two milestones at milestone factor  $\times 1$  and milestone factor  $\times 2$  training iterations at which the learning rate is multiplied with gamma.
8. Batch size.

Table A.1 can be found in the Appendix A and lists the value ranges. All the remaining settings, as well as the sampling strategy and the features, are identical to FCNN no. 11 from Table 4.5.

The HPO is run for 40 trials, i.e. 40 different FCNNs are trained and evaluated. *Optuna* uses a combination of random search and Bayesian optimisation to determine the hyperparameters for each trial. Trying to find the optimum with only 40 trials while varying 8 hyperparameters may not be sufficient, but it can give an impression of to what extent improvements over the baseline model are possible. A larger number of trials might lead to a better result, however, depending on the network topology and the learning rate, training a neural network can be very costly.

Table 4.6 presents training and test metrics for the best model of the systematic test in subsection 4.3.3 and the model that results from the HPO. The corresponding hyperparameters are listed in Table A.1 in the Appendix A. An improvement can be seen regarding all three train metrics, however, regarding the test metrics, the optimised model does only perform slightly better on the MAE. Consequently, the optimised FCNN is less capable of generalising on unseen data and to some degree overfitted to the training data. The HPO leads to a larger number of neurons per hidden layer and more hidden layers. The fact that the weight of each neuron is tuned towards the training data underlines the assumption that the deeper and wider network is overfitted to the training data. It must be noted that two hyperparameters result in values on the edge of the sampling space. However, because an HPO requires a lot of time and computational resources and the first 40 trials do not lead to an improvement over the baseline, the HPO is not further extended within this thesis.

	Training			Test		
	$R^2$	MAE ·10 <sup>3</sup>	MSE ·10 <sup>3</sup>	$R^2$	MAE ·10 <sup>3</sup>	MSE ·10 <sup>3</sup>
FCNN No. 11	0.967	3.29	0.12	<b>0.898</b>	6.67	<b>0.47</b>
HPO result	<b>0.977</b>	<b>2.34</b>	<b>0.08</b>	0.884	<b>6.39</b>	0.54

**Table 4.6:** Comparison of training and test metrics of HPO result and previous best FCNN model.

Considering that the optimised FCNN does not exhibit an overall improvement regarding the evaluated metrics, and contains more neurons, which demands more storage space and training time, the following investigations are not done using the optimised FCNN, but FCNN no. 11.

## 4.4 Application to Steady Simulations

To conclude the investigation of the FIML approach on steady cases, the trained model is applied within the RANS solver of the DLR-TAU code as described in section 3.5. A correction period of 500 inner iterations between evaluations of the trained ML model is chosen. Other settings remain unchanged compared to the baseline SA simulation. Convergence is reached at all angles of attack. Figure 4.24 presents the resulting lift, drag, and pitching moment coefficients. Overall, the augmented simulations, i.e. the RANS simulations with the SA model that is corrected using the trained ML model, match with the FI solutions and hence the reference data.

In addition to the global forces and the surfaces plots that are presented up to this point figures A.4 and A.5 in the Appendix A present field solutions of  $c_p$  at  $\alpha = 1.5^\circ$  and  $\alpha = 4.5^\circ$ . The augmented simulations show improved field solution over the baseline SA solution.

### Investigation of $\alpha = 5.5^\circ$

The strongest deviations can be seen for  $\alpha = 5.5^\circ$ , most obviously for  $c_{my}$ . As Figure 4.25 shows, the augmented SA solution is closer to the reference solution than the FI at the shock. However, in the rear shock region, the augmented SA solution is slightly closer to the baseline solution than the FI solution.

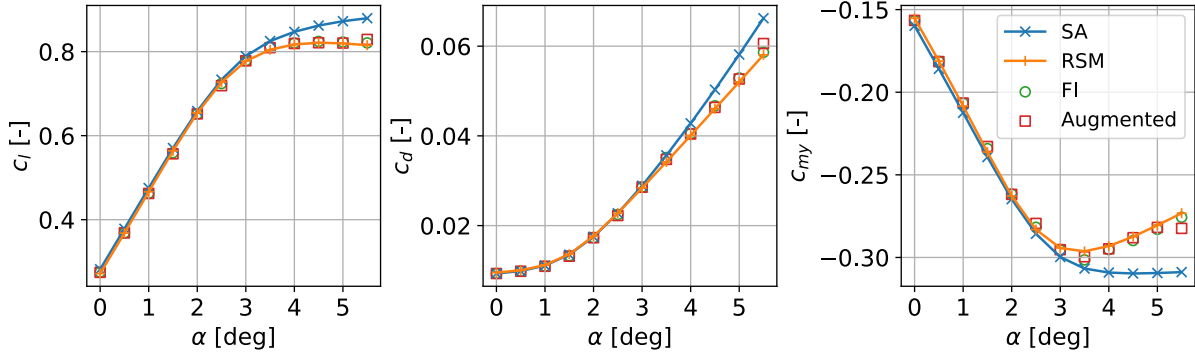


**Figure 4.24:**  $c_l$  (left),  $c_d$  (middle), and  $c_{my}$  (right) over  $\alpha$  for  $M = 0.75$   $Re = 6.0 \cdot 10^6$  comparing SA, RSM, FI, and SA augmented using the trained ML model.

To investigate why the result at  $\alpha = 5.5^\circ$  is worse than for the other angles of attack, first, the  $\beta$ -field of the FI for the case in question is presented in Subfigure 4.26a. The contour lines in the plot are at  $\beta = 0.5$ . Subfigure 4.26b presents the difference between the correction field that results from the augmented SA simulation and the FI result. It becomes clear that errors are especially high in regions with  $\beta < 0.5$  in the FI result.

The feature distribution of  $\eta_{11}$  over  $\beta$  is presented in Figure 4.27 (or  $\eta_7$  over  $\beta$  in Figure A.3 in the Appendix A). The area of  $\beta < 0.5$  and  $\eta_{11} < 0.3$  contains samples of the  $\alpha = 5.5^\circ$  case, but not of the other angles of attack. The  $\alpha = 5.5^\circ$  sample is not in the span of the training set of the ML correction model. Consequently, the sample is a case of extrapolation. This explains the imperfect prediction in areas where  $\beta < 0.5$  is expected according to the FI result. Nevertheless, the result is still an improvement over the baseline model.

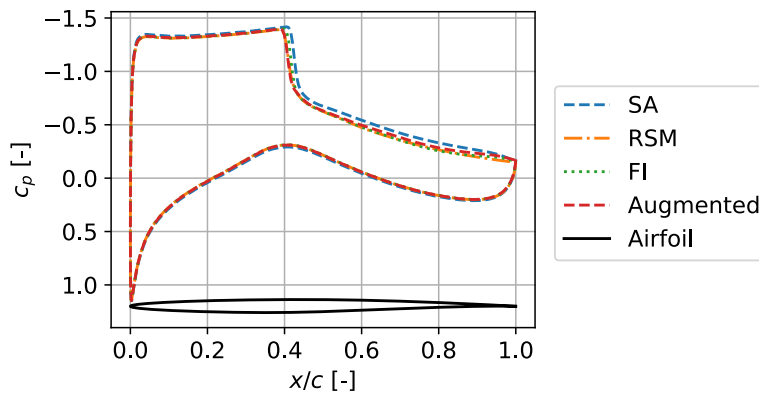
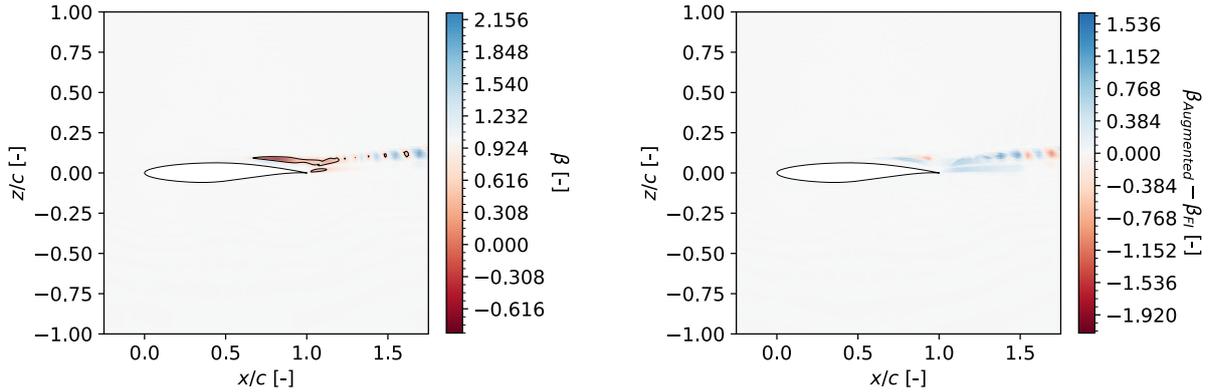


**Figure 4.25:** Comparison of  $c_p$ -distributions of SA, RSM, FI, and SA augmented using the trained ML model at  $\alpha = 5.5^\circ$

## Evaluation

Applying the ML model that is trained as explained in the previous sections yields a good correction of steady RANS simulations with the SA model. As the model can yield good correction results over a varying angle of attack it implicitly knows  $d\beta/d\alpha$  even though the predictions are made nodewise based on local flow features and not with  $\alpha$  as an input variable. Given these advancements, the trained model can now be applied to unsteady



(a)  $\beta$ -field of FI result at  $\alpha = 5.5^\circ$  with contour lines at  $\beta = 0.5$ . (b) Comparison of  $\beta$ -field of FI result and augmented ML simulation at  $\alpha = 5.5^\circ$ .

**Figure 4.26:** Synthetic test cases with baseline and reference solution from different angles of attack.

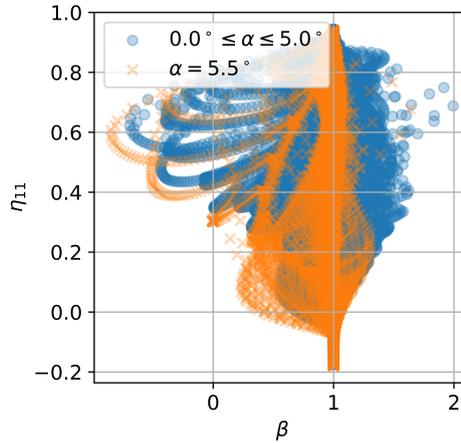


**Figure 4.27:** Comparison of  $\eta_{11}$  over  $\beta$  for all samples vs.  $\alpha = 5.5^\circ$  samples.

simulations with a pitching airfoil to evaluate how a model trained on steady data affects unsteady simulations.

## 4.5 Unsteady Case Description and Preparation

Analog to subsection 4.1.2, the objective of this section is to produce unsteady simulations with the SA turbulence model as the baseline solution and the RSM turbulence model as the reference solution. The unsteadiness is caused by a pitching motion of the rigid airfoil. This type of isolated motion is chosen as it only contains a temporal change of the angle of attack and thus is a suitable test case for the effect of an ML model that is trained to predict  $d\beta/d\alpha$ .

### 4.5.1 Data Generation

The same airfoil and mesh as introduced in subsection 4.1.2 are used for the unsteady simulations. Furthermore, no changes are made regarding the turbulence models.

## Flow Conditions

Unsteady simulations do not require a steady solution as a starting point, however, starting from a converged steady solution reduces the computational effort. Based on section 4.1, steady simulations are available for multiple angles of attack. As the goal is to apply the ML model trained on steady data to unsteady simulations it is obvious to use the available steady simulations as a starting point. Three angles of attack, each corresponding to a different flow condition, are selected:

- $\alpha = 1.5^\circ$ : This case is located on the linear region of the  $c_l$ - $\alpha$ -curve, SA and RSM are very close together. FI and augmented SA simulation both lead to good results.
- $\alpha = 3.0^\circ$ : Placed at the beginning of the non-linear region of the  $c_l$ - $\alpha$ -curve, this case is stronger affected by non-linearities. Furthermore, differences between SA and RSM become visible. Both FI and augmented SA simulation yield good corrections.
- $\alpha = 4.5^\circ$ : Even larger differences between SA and RSM can be found for this case. Being placed in the non-linear region of the  $c_l$ - $\alpha$ -curve, this is the most challenging correction of the three angles of attack. FI and augmented SA simulation both lead to good correction results.

Given the steady solution at an angle of attack, the motion and therefore the unsteadiness of the harmonically pitching airfoil is defined by two variables, both introduced in section 2.2: the pitching amplitude  $\hat{\theta}$  and the reduced frequency  $k$ . Table 4.7 presents the combinations of  $k$  and  $\hat{\theta}$  that are computed at each of the three mean angles of attack. At  $\hat{\theta} = 0.001^\circ$  the influence of the reduced frequency is evaluated. The investigation is conducted at 8 reduced frequencies between 0.01 and 1.0. With  $k = 0.01$  as a very small reduced frequency that is close to quasi-steady conditions, i.e.  $k \rightarrow 0$ , and  $k = 1.0$  representing pronounced unsteadiness. In addition,  $k = 0.3$  is selected as a reduced frequency at which the influence of the amplitude is investigated. In addition to  $\hat{\theta} = 0.001^\circ$ , three more amplitudes are evaluated, each an order of magnitude larger previous one.

$\hat{\theta} \backslash k$	0.01	0.1	0.2	0.3	0.4	0.5	0.75	1.0
$0.001^\circ$	X	X	X	X	X	X	X	X
$0.01^\circ$				X				
$0.1^\circ$				X				
$1^\circ$				X				

**Table 4.7:** Combinations of reduced frequency and pitching amplitude considered for the unsteady simulations.

## Computation

For the unsteady dual time-stepping RANS computation a convergence criterion for the inner iterations in each physical time step must be set. In addition, the physical time step  $\Delta t_{\text{physical}}$  must be set small enough to accurately depict the unsteady flow behaviour, but as large as possible to reach a converged simulation as fast as possible. The two different types of convergence must be distinguished: the first concerns the convergence of the inner iterations with each time step, and the second concerns the decay of transient oscillation of quantities of interest, e.g.  $c_l(t)$  or  $c_{my}(t)$ .

A CAUCHY convergence criterion is used to monitor the change of  $c_l$ ,  $c_d$ , and  $c_{my}$ . If the values change less than  $\Delta c_{l,CAUCHY} = 1 \cdot 10^{-4}$ ,  $\Delta c_{d,CAUCHY} = 1 \cdot 10^{-5}$ ,  $\Delta c_{my,CAUCHY} = 5 \cdot 10^{-6}$  over an episode of 200 inner iterations the physical time step has reached convergence. This means a minimum number of 200 inner iterations is performed for each physical time step.

$k$ [-]	0.01	0.1	0.2	0.3	0.4	0.5	0.75	1.0
Time steps per period [-]	8192	1024	512	256	256	256	128	128
$\Delta t_{\text{physical}} \cdot 10^4$ [s]	3.09	2.47	2.47	3.29	2.47	1.98	2.63	1.98

**Table 4.8:** Time steps per pitching period and physical time step size  $\Delta t_{\text{physical}}$  at each reduced frequency  $k$ .

The physical time step size is determined by trial and error until a satisfying progression of  $c_l(t)$  and  $c_{my}(t)$  can be observed for an exemplary simulation. Subsequently, the number of physical time steps per oscillation period is adapted in such a way that similar physical time step sizes are obtained for each reduced frequency. Table 4.8 shows the resulting values. The number of oscillation periods, and hence the overall number of physical time steps, is determined for each case and thus not listed in this thesis.

## 4.5.2 Resulting Data

Due to the excitation of the airfoil, the forces acting on it are changing with time. The following investigation takes  $c_l(t)$  and  $c_{my}(t)$  into account. Figure 4.28 presents the progression of the excitation signal and the two force coefficients over time for the exemplary case  $\bar{\alpha} = 3.0^\circ$ ,  $\hat{\theta} = 0.001^\circ$ , and  $k = 0.3$  of the reference simulation. At the start of the unsteady simulation, transient effects are present. After the transient effects have decayed, a steady magnitude and phase shift between force coefficients and excitation signal can be observed.

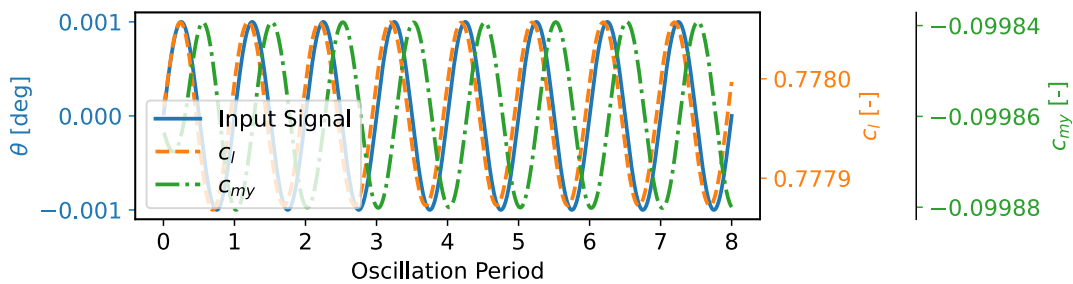


**Figure 4.28:** Excitation  $\theta$  and resulting force coefficients  $c_l$ ,  $c_{my}$  vs. number of excitation periods for  $\bar{\alpha} = 3.0^\circ$ ,  $\hat{\theta} = 0.001^\circ$ , and  $k = 0.3$  for the reference simulation.

## Frequency Domain Analysis

Investigating the oscillation behaviour in the time domain may be inaccurate as phase shift or magnitude can not be read directly from a plot over time. Consequently, the signals are transferred to the frequency domain for further analysis. Using a fast FOURIER transform (FFT), a discrete time-dependent signal is transferred to the frequency domain efficiently [67]. The result of the FFT is a spectrum of complex values that determine the contribution of discrete frequencies to the original signal [68]. By dividing the result

corresponding to the smallest frequency of the FFT of a quantity of interest by the result corresponding to the smallest frequency of the FFT of the excitation signal, a frequency response function (FRF) is obtained. The result of the FRF is a complex value which can be split into a magnitude and a phase.

Computing the FRF over an analysis window of one excitation period which is sliding over the time domain signal yields Figure 4.29. Analog to Figure 4.28 transient effects are present in the first periods before the signal settles on steady values for the magnitude and phase.

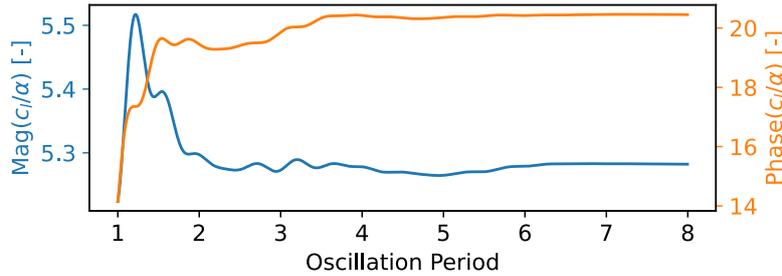


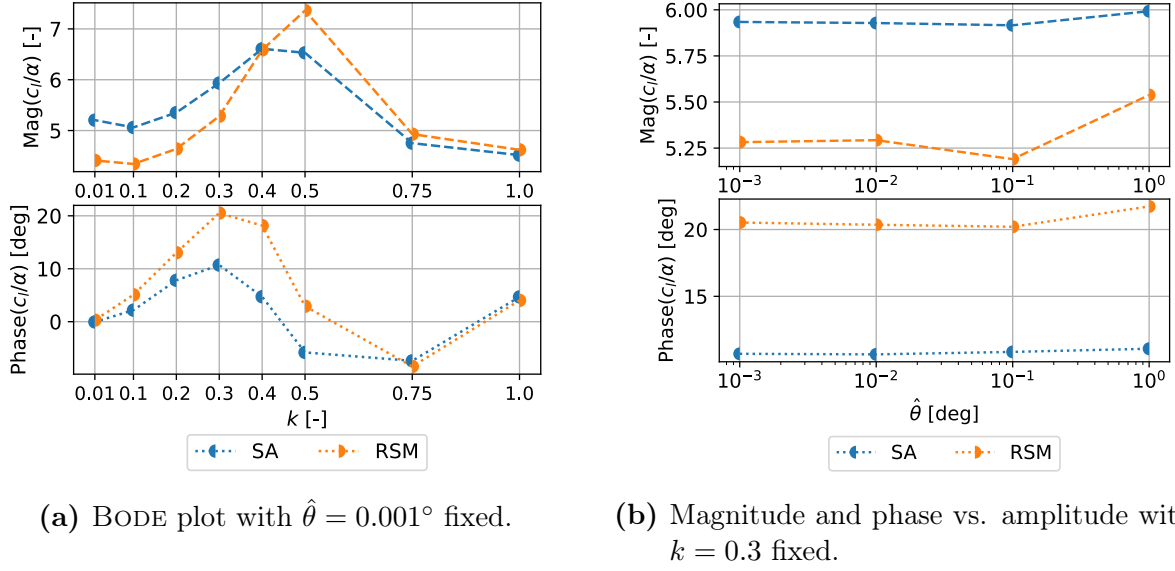
**Figure 4.29:** Sliding FFT of  $c_l/\alpha$  vs. number of excitation periods for  $\bar{\alpha} = 3.0^\circ$ ,  $\hat{\theta} = 0.001^\circ$ , and  $k = 0.3$  for the reference simulation.

#### Data at $\bar{\alpha} = 3.0^\circ$

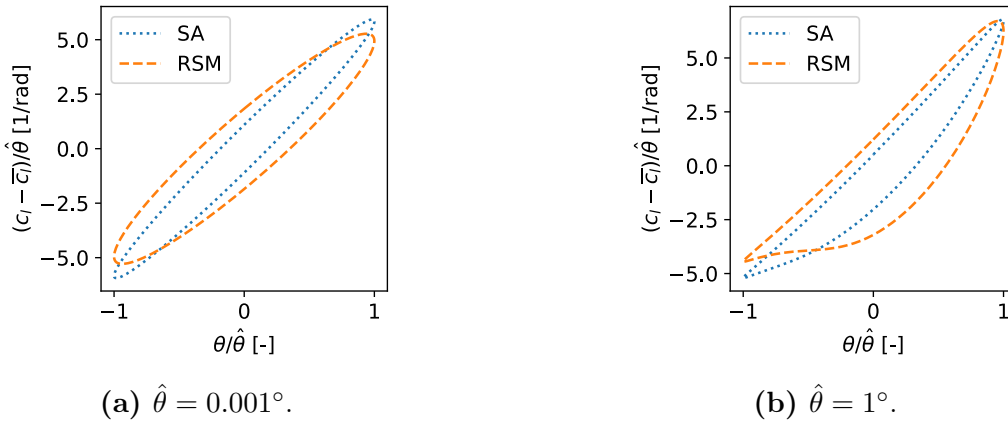
The resulting magnitude and phase values can now be analysed over the reduced frequency, i.e. in a BODE plot, or over the amplitude of the excitation signal. Subfigure 4.30a presents the BODE plot for  $\alpha = 3.0^\circ$ , comparing the SA baseline model with the RSM based reference data. Differences in both, the magnitude in the upper plot and the phase in the lower plot of  $c_l/\alpha$  can be seen at almost all reduced frequencies. However, at  $k = 0.75$  and  $k = 1$ , both results are close together. The RSM results exhibit a larger peak in the magnitude plot and stronger phase shifts. Thus, the SA model should be corrected in these areas. Subfigure 4.30b presents the same values on the y-axis over the excitation amplitude. While SA is almost constant over  $\hat{\theta}$ , RSM varies slightly. However, the small scale of the plot must be noticed.

Figure 4.31 presents how the lift changes with two different excitation amplitudes over one excitation period. For  $\hat{\theta} = 0.001^\circ$  an elliptic hysteresis curve can be seen for both turbulence models (see Subfigure 4.31a). The shape of the ellipses corresponds to the magnitude and phase. The position of the ellipses corresponds to the gradient of the steady  $c_l-\alpha$  curve (see Figure 4.5) in combination with unsteady effects. At a higher pitch amplitude, the resulting curve is no longer an ellipse (see Subfigure 4.31b). The complex shape of the hysteresis curve is an indicator of non-linear effects. For the RSM model, a stronger deviation from the elliptic shape can be seen. This might explain why RSM deviates stronger from the constant magnitude and phase trend in Subfigure 4.30b.

More data at different angles of attack is not shown at this point to keep the text concise and because similar plots, extended with corrected simulation results, are shown in section 4.6.



**Figure 4.30:** Unsteady baseline and reference results in the frequency domain for  $\bar{\alpha} = 3.0^\circ$ .



**Figure 4.31:** Unsteady portion of the lift coefficient normalised with pitch amplitude  $(c_l - \bar{c}_l)/\hat{\theta}$  over pitch angle normalised with pitch angle  $\theta/\hat{\theta}$  for SA and RSM at  $\bar{\alpha} = 3.0^\circ$ ,  $k = 0.3$ , and two different amplitudes.

## 4.6 Correction of Unsteady Simulations

The final step of this test case is to apply the correction model trained on steady data (see sections 4.2-4.4) to unsteady simulations and to compare the results to the unsteady RSM reference data (see section 4.5).

### 4.6.1 Approaches

Multiple approaches are tested to correct the unsteady simulation. While the main objective is to investigate the effect of coupling the trained ML model with the unsteady solver, two approaches that use a steady  $\beta$ -field are tested as well.

### FI-Based Steady $\beta$ -Field

The FIs in section 4.2 deliver a  $\beta$ -field containing a spatially varying correction term that is valid for the steady flow conditions of each case. Instead of applying a trained ML model the steady  $\beta$ -field is applied as an input-invariant correction to the unsteady simulation. Given the assumption that the flow field of an unsteady flow with very small excitation amplitudes is close to the steady flow field, the idea of applying a steady  $\beta$ -field is that also the correction field is valid if the unsteady effects are small enough.

The FI-based steady  $\beta$ -field is applied using a *dummy* correction model that constantly predicts the same correction field. The same CAUCHY convergence criterion with 200 iterations for evaluation as for the baseline and reference simulation is used. According to section 3.5, a number of subiterations in each physical time step might be performed. Even though this is not necessary, as the  $\beta$ -field does not change, 5 subiterations are performed in each physical time step to be consistent with the application of the actual ML-based correction model.

### ML-Based Steady $\beta$ -Field

The application of an ML-based steady  $\beta$ -field is similar to the previous approach, but instead of using a steady  $\beta$ -field that results from an FI, this approach uses the  $\beta$ -field that results from an ML-augmented steady simulation. For the steady simulations, the area selection approach is applied. Thus, the steady correction fields that are applied to unsteady simulations only contain non-unity values in the selected area. In contrast to FI-based steady  $\beta$ -fields this approach can be used at mean angles of attack without an FI result. The convergence and subiteration settings are chosen analogues to the previous approach if not stated differently.

### Applied ML Model

Applying the steadily trained ML model to unsteady simulations serves the goal of investigating whether the implicitly learned  $d\beta/d\alpha$  relationship delivers a benefit. It is expected that with increased unsteadiness the steady correction model depreciates in accuracy as temporal derivatives gain importance. Per default, the ML model is evaluated five times per physical time step, i.e. 5 subiterations are performed, and the CAUCHY convergence settings are set as mentioned above. As a steady start, this approach uses a steady simulation result that is augmented using the same model.

### Assessment

Some advantages and disadvantages of the three approaches are known before the investigation of the results. Table 4.9 gives an overview. The listed advantages and disadvantages are not weighed, and refer to a comparison of the approaches with one another and not with further approaches.

## 4.6.2 Results

The results in this subsection are described per mean angle of attack  $\bar{\alpha}$ . Due to issues with the numerical stability for  $\bar{\alpha} = 4.5^\circ$ , investigations on unsteady simulations without excitation are made before the results with excitation are examined. To be concise, all

Approach	Advantages	Disadvantages
FI-based steady $\beta$ -field	<ul style="list-style-type: none"> <li>- Most accurate correction field</li> <li>- Correction term available in entire domain</li> </ul>	<ul style="list-style-type: none"> <li>- Correction valid for single angle of attack</li> <li>- FI solution must exist at <math>\bar{\alpha}</math></li> </ul>
ML-based steady $\beta$ -field	<ul style="list-style-type: none"> <li>- Not limited to certain angles of attack</li> </ul>	<ul style="list-style-type: none"> <li>- Correction available in selected area only</li> <li>- Correction valid for single angle of attack</li> <li>- Predictions influenced by accuracy of ML model</li> </ul>
Applied ML model	<ul style="list-style-type: none"> <li>- Model valid at a range of <math>\alpha</math></li> <li>- <math>d\beta/d\alpha</math> relationship implicitly learned</li> </ul>	<ul style="list-style-type: none"> <li>- Correction available in selected area only</li> <li>- Possibly numerically least stable (RANS solver coupled with ML model)</li> <li>- Predictions influenced by accuracy of ML model</li> </ul>

**Table 4.9:** Advantages and disadvantages of the different models

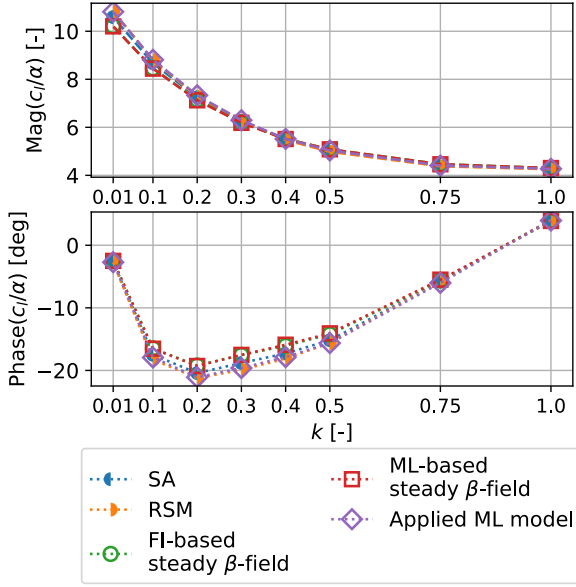
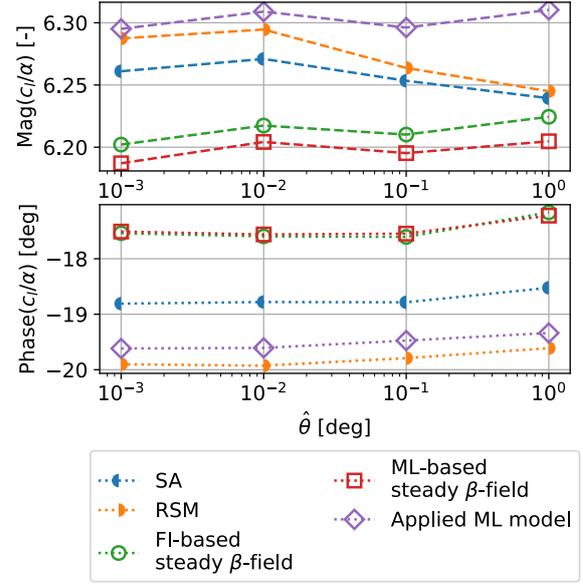
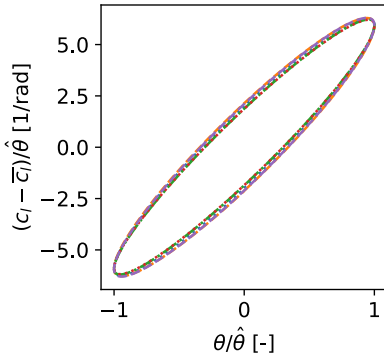
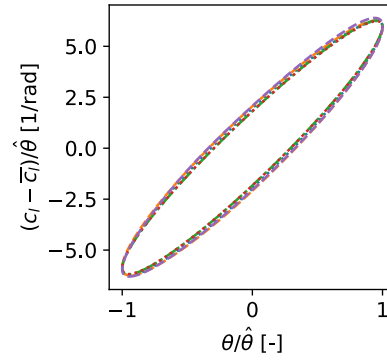
investigations in the text are done regarding  $c_l$ . The corresponding plots for  $c_{my}$  can be found in the Appendix A.

$$\bar{\alpha} = 1.5^\circ$$

Figure 4.32 presents the results of the unsteady simulations with  $\bar{\alpha} = 1.5^\circ$ , comparing SA and RSM with the three correction approaches. The BODE plot in Subfigure 4.32a presents a monotonously decreasing magnitude with increasing  $k$ . Starting close to 0 for  $k = 0.01$ , the phase decreases up to  $k = 0.2$  before it increases. Overall, SA and RSM are very close together. Thus, this case is less a check of the ability to correct, but rather a check of whether the correction models cause deterioration when a good baseline solution is present. The applied ML model is visibly close to the RSM solution, the FI- and ML-based steady  $\beta$ -fields deviate from the SA solution in the *wrong* direction, i.e. the results are further away from the RSM solution. With increasing reduced frequency the differences between all approaches become negligible.

The trend at  $\hat{\theta} = 0.001$  can be observed at all tested amplitudes as Subfigure 4.32b depicts. Note that the scales on the axes are very small. All approaches lead to a roughly constant relationship between magnitude and amplitude, respectively phase and amplitude. The hysteresis plots in subfigures 4.32c and 4.32d confirm the findings, the results are not distinguishable visibly, however, some variance can be seen. At both amplitudes, the hysteresis plots present an ellipse. Consequently, the flow is dominated by linear effects.

To summarize the findings, the applied ML model leads to the best results for small differences between baseline and reference. The steady  $\beta$ -fields yield a small deterioration in some cases.

(a) BODE plot with  $\hat{\theta} = 0.001^\circ$  fixed.(b) Magnitude and phase vs. amplitude with  $k = 0.3$  fixed.(c) Hysteresis plot at  $k = 0.3$ ,  $\hat{\theta} = 0.001^\circ$ .(d) Hysteresis plot at  $k = 0.3$ ,  $\hat{\theta} = 1^\circ$ .

**Figure 4.32:** Unsteady results at  $\bar{\alpha} = 1.5^\circ$  for  $c_l$ . All plots use the same colour scheme. Figure A.6 in the Appendix A presents the corresponding results for  $c_{my}$ .

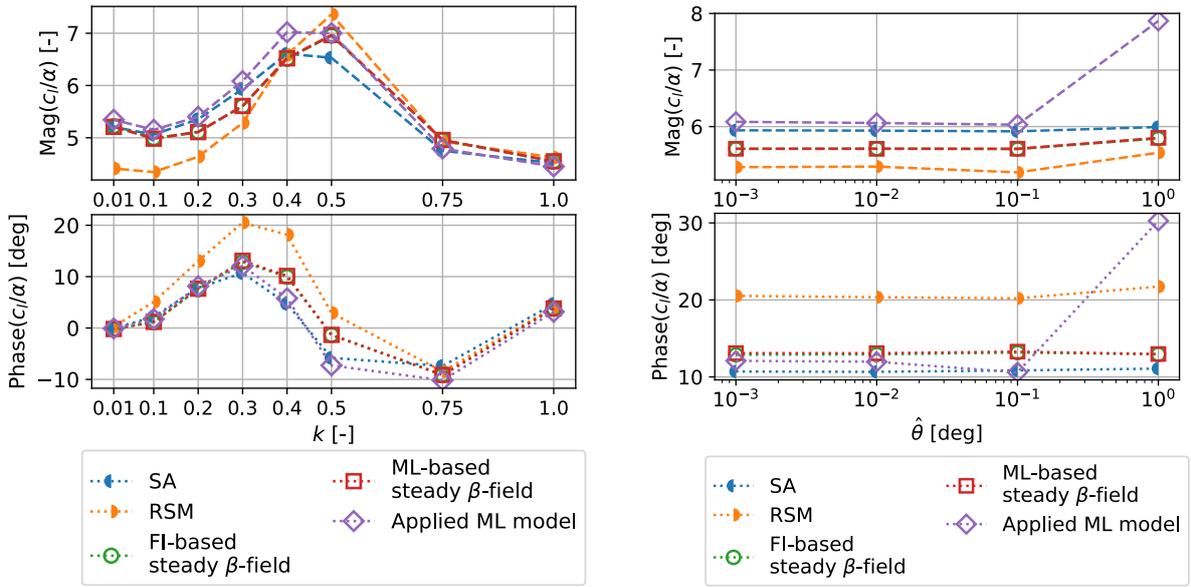
$\bar{\alpha} = 3.0^\circ$

Larger differences between SA and RSM results can be observed at  $\bar{\alpha} = 3.0^\circ$  as already discussed in subsection 4.5.2 and presented in Figure 4.33. The applied ML model delivers ambiguous results: at most reduced frequencies in the BODE plot in Subfigure 4.33a the resulting magnitude and phase is close to the baseline solution. Near the resonance peak at  $k = 0.5$ , the applied ML model corrects the magnitude in the right, but the phase in the wrong direction. With increasing excitation amplitude the behaviour remains (see Subfigure 4.33b). However, at  $\hat{\theta} = 1$  the result deviates from the previously constant trend. The corresponding hysteresis plot in Subfigure 4.33d confirms that the applied ML model predicts a significantly different flow behaviour. In addition to unsatisfactory results at small amplitudes, the application of the ML model loses validity at larger amplitudes.

More promising, but not sufficiently accurate results can be seen for the steady  $\beta$ -fields, both FI- and ML-based lead to congruent results. For all investigated points the corrected

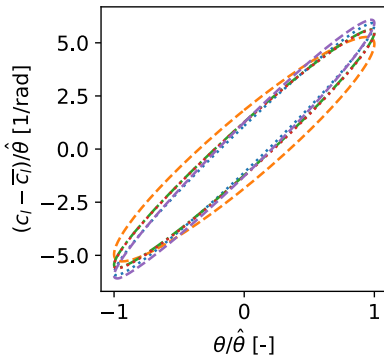
result lies between SA and RSM, for some cases closer to RSM, for some closer to SA. Consequently, the correction using steady  $\beta$ -fields does not always yield good corrections, however, it does not impair the baseline solution. The correction at higher reduced frequencies yields better results than closer to the quasi-steady case. With increasing amplitude, the steady  $\beta$ -fields have a stable behaviour. However, comparing the shapes of the hysteresis curves in subfigures 4.33c and 4.33d the correction with steady  $\beta$ -fields are closer to SA than RSM.

In contrast to the previous case, the results of this mean angle of attack favour the correction using steady correction fields over the applied ML model.

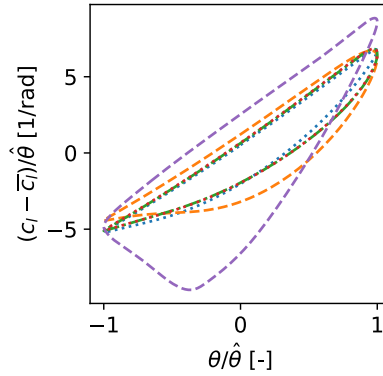


(a) BODE plot with  $\hat{\theta} = 0.001^\circ$  fixed.

(b) Magnitude and phase vs. amplitude with  $k = 0.3$  fixed.



(c) Hysteresis plot at  $k = 0.3$ ,  $\hat{\theta} = 0.001^\circ$ .



(d) Hysteresis plot at  $k = 0.3$ ,  $\hat{\theta} = 1^\circ$ .

**Figure 4.33:** Unsteady results at  $\bar{\alpha} = 3.0^\circ$  for  $c_l$ . All plots use the same colour scheme. Figure A.7 in the Appendix A presents the corresponding results for  $c_{my}$ .

### $\bar{\alpha} = 4.5^\circ$ without Excitation

At  $\bar{\alpha} = 4.5^\circ$ , the ML-based steady  $\beta$ -field and the applied ML model do not converge to steady magnitude and phase values. Thus, before the available results are investigated, unsteady simulations without excitation are conducted to investigate the convergence

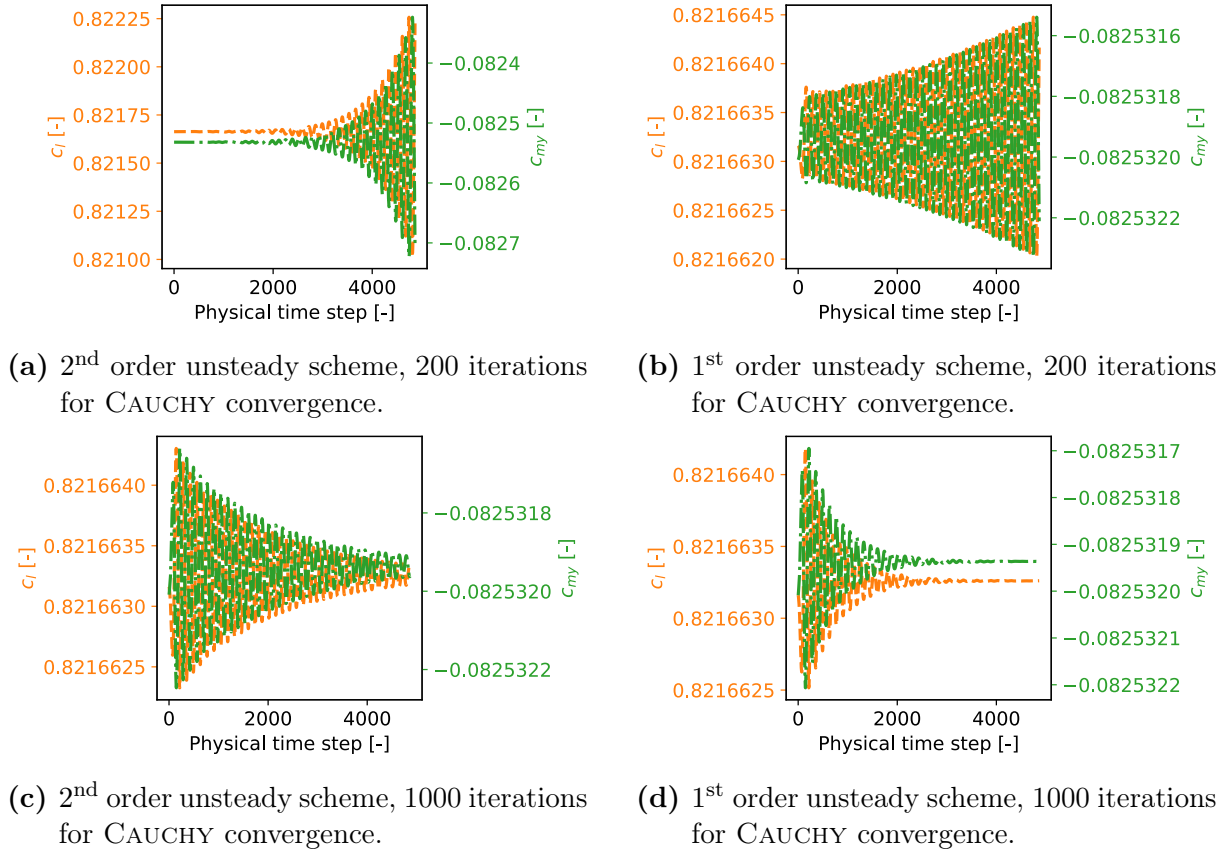


**Figure 4.34:** Influence of unsteady order scheme and the number of iterations to evaluate the CAUCHY convergence for simulations without excitation applying an ML-based steady  $\beta$ -field. Note that the axes use different scales.

issues. The initial settings of this test are analogue to the previous investigations of  $k = 0.3$ . The influence of the following parameters is tested:

- Number of subiterations.
- Interval for evaluation of CAUCHY convergence, i.e. the minimum number of inner iterations.
- Unsteady order scheme. The previous simulations use a 2<sup>nd</sup> order scheme, i.e. two past physical time steps are used to compute the next one. A 1<sup>st</sup> order scheme is tested.
- Physical time step size.

Not all parameter combinations are tested and only selected results are presented in this thesis.

Subfigure 4.34a presents how  $c_l$  and  $c_{my}$  progress using the same settings as previously described for the cases with excitation. The oscillations diverge over time. While the mentioned figure concerns the correction using an ML-based steady  $\beta$ -field, convergence is reached for the FI-based steady  $\beta$ -field (not depicted). For the steady simulations, the FI and applied ML model are close together, furthermore, both produce very similar results for the unsteady simulations at  $\bar{\alpha} = 1.5^\circ$  and  $\bar{\alpha} = 3.0^\circ$ . However, the difference

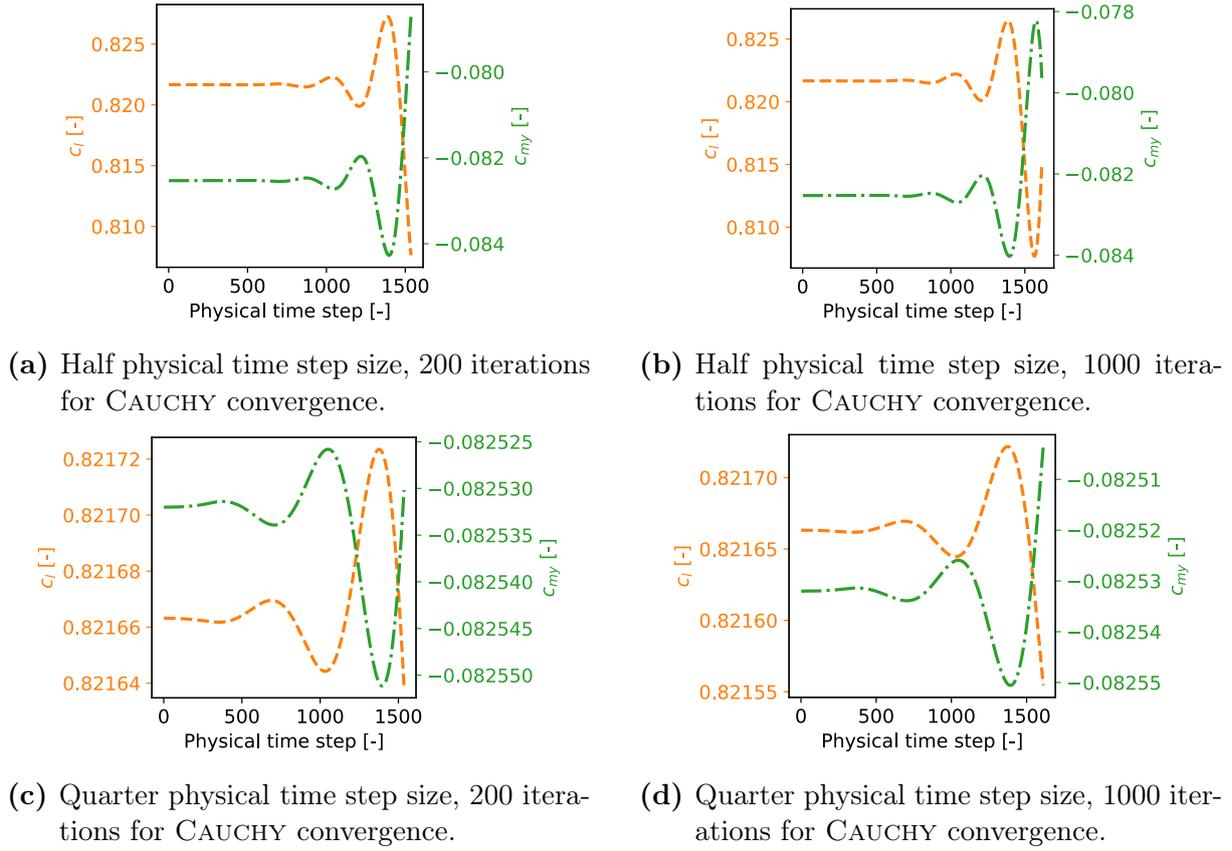


**Figure 4.35:** Influence of physical time step size (in comparison to  $\Delta t_{\text{physical}}$  for  $k = 0.3$  in 4.8) and the number of iterations to evaluate the CAUCHY convergence for simulations without excitation applying the trained ML model. Note that the axes use different scales.

between FI- and ML-based steady  $\beta$ -field, i.e. the noise in the ML prediction, leads to numerical instability at  $\bar{\alpha} = 4.5^\circ$  where strong non-linearities are present.

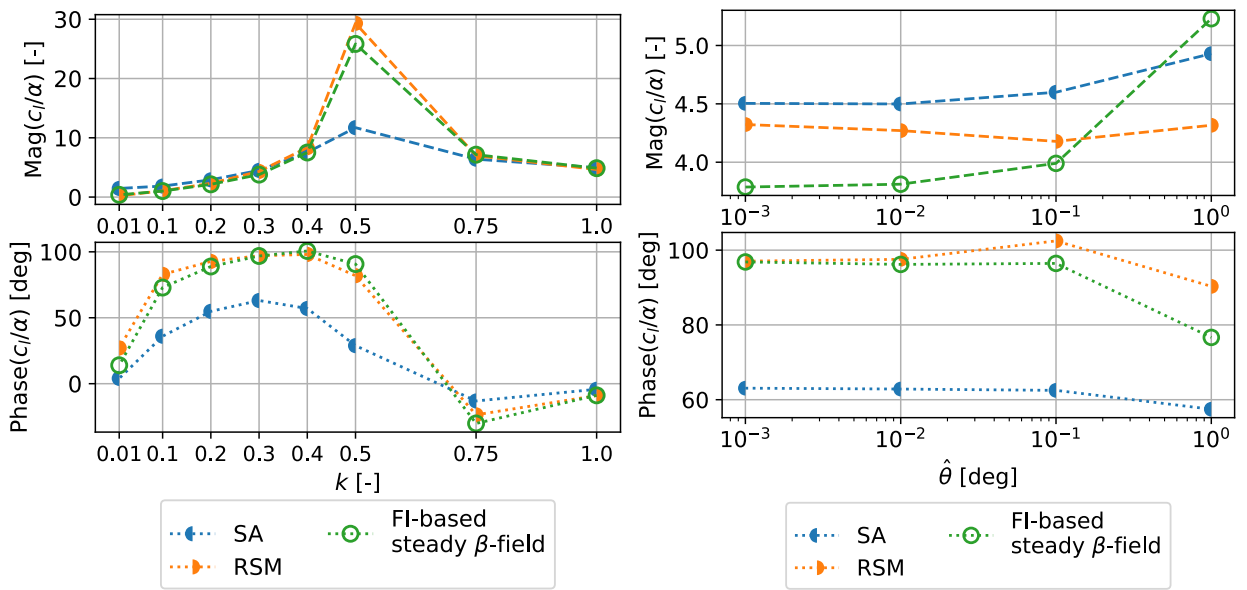
Switching from a 2<sup>nd</sup> to a 1<sup>st</sup> order unsteady scheme still results in divergence, however, much slower (see Subfigure 4.34b). When increasing the number of iterations for CAUCHY convergence from 200 to 1000, convergence is reached. Using the 1<sup>st</sup> order scheme the oscillation settles faster.

Transferring the settings that yield convergence for the ML-based steady  $\beta$ -field to the applied ML model does not lead to a converging unsteady simulation (not depicted). Thus, Figure 4.35 compares the influence of the physical time step size to the influence of increasing the number of iterations for the evaluation of the CAUCHY convergence. As, according to the previous findings, the 1<sup>st</sup> order unsteady scheme is more stable, it is used in all cases. In all four subfigures, the simulation becomes unstable at some point. Decreasing the physical time step size seems to be more effective than performing more inner iterations.

Varying the number of subiterations does also not lead to convergence and is not depicted here. In conclusion, no combination of settings that produces a stable unsteady simulation using the applied ML model is found.

### $\bar{\alpha} = 4.5^\circ$ with Excitation

No settings that allow a stable computation using the applied ML are found for the simulation without excitation. Consequently, no stable simulations with excitation are expected and thus this approach is not investigated. The ML-based steady  $\beta$ -field is applied with an increased number of 1000 iterations for the evaluation of the CAUCHY convergence, and using both types of unsteady scheme order. However, the simulations only converge at a couple of combinations of reduced frequency and excitation amplitude. Even though this shows that convergence of the ML-based steady  $\beta$ -field approach is possible, no combination of satisfactory settings could be found within the duration of this thesis. Consequently, the following comparison includes SA, RSM and FI-based steady  $\beta$ -field only.



(a) BODE plot with  $\hat{\theta} = 0.001^\circ$  fixed.

(b) Magnitude and phase vs. amplitude with  $k = 0.3$  fixed.

(c) Hysteresis plot at  $k = 0.3$ ,  $\hat{\theta} = 0.001^\circ$ .

(d) Hysteresis plot at  $k = 0.3$ ,  $\hat{\theta} = 1^\circ$ .

**Figure 4.36:** Unsteady results at  $\bar{\alpha} = 4.5^\circ$  for  $c_l$ . All plots use the same colour scheme. Figure A.8 in the Appendix A presents the corresponding results for  $c_{my}$ .

Figure 4.36 presents the results of the unsteady simulations at  $\bar{\alpha} = 4.5^\circ$ . The BODE plot shows a very good correction using the FI-based steady  $\beta$ -field (see Subfigure 4.36a). The correction is consistent with increasing amplitude up to  $\hat{\theta} = 0.1$ . Keeping in mind the

small scale on the axis for the magnitude, this can be seen in Subfigure 4.36b. Regarding the shape of the hysteresis plots the previous findings are confirmed. At a small amplitude, the corrected simulation approaches the reference, however, it starts to deviate at larger amplitudes (see subfigures 4.36c and 4.36d).

The resonance peak of the RSM reference solution at  $\bar{\alpha} = 4.5^\circ$  is about three times higher than at  $\bar{\alpha} = 3.0^\circ$ , compare subfigures 4.33a and 4.36a. A peak in the magnitude that approaches infinity corresponds to a buffet onset [69]. Therefore, it is not surprising that the simulations  $\bar{\alpha} = 4.5^\circ$  that are closer to buffet onset are numerically more sensitive.

### Consistency for $k \rightarrow 0$

For quasi-steady simulations with  $k \rightarrow 0$ , one would expect the unsteady results to approach the steady results. However, even though good corrections of steady simulations are achieved at all of the three considered angles of attack this is not the case for the unsteady simulations, e.g. at  $\bar{\alpha} = 3.0^\circ$  all correction approaches at  $k = 0.001$  are closer to SA than RSM.

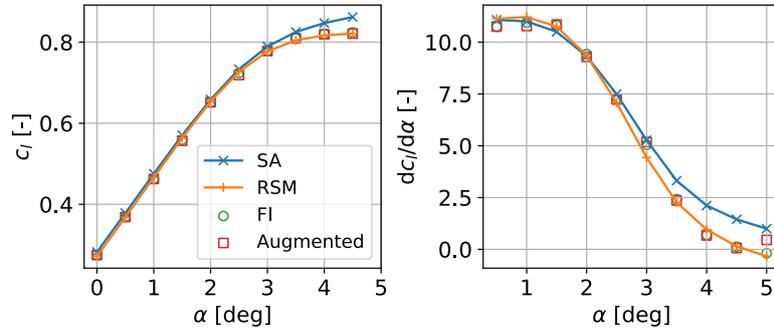


**Figure 4.37:**  $c_l$  (left), and  $dc_l/d\alpha$  (right) over  $\alpha$  for  $M = 0.75$   $Re = 6.0 \cdot 10^6$  comparing SA, RSM, FI, and SA augmented using the trained ML model. Figure A.9 in the Appendix A presents the corresponding results for  $c_{my}$ .

The previous unsteady investigations in the frequency domain concern the magnitude and phase ratio of  $c_l/\alpha$ . Thus, Figure 4.37 depicts the gradient  $dc_l/d\alpha$  of the steady simulations. The derivatives are computed using a 2<sup>nd</sup> order central finite difference and are therefore not available for  $\alpha = 0^\circ$  and  $\alpha = 5.5^\circ$ . In contrast to the good match between the global force coefficients of the FI and the augmented simulation to the reference data, the derivatives do not match the reference at all angles of attack. However, the plot confirms that the investigated values of the unsteady simulations approach the value of the steady derivatives for  $k \rightarrow 0$ . Consequently, the correction model can be just as good regarding the unsteady simulation as the corresponding reference case. Interestingly, the effect is not only present for the ML model that is trained on multiple angles of attack but also for the steady  $\beta$ -field corrections that do not contain information about the neighbouring angles of attack.

## 4.7 Findings

This section briefly summarizes the findings of chapter 4. The full conclusion for this thesis can be found in chapter 6.

The FI is capable of correcting a surface  $c_p$ -distribution using a number of reference points that are realistic for an experimental setup. The corrections with  $c_p$  as reference quantity yield good correction of the resulting integral values, however,  $c_f$  is not corrected. Furthermore, differences between reference and baseline that are not caused by the turbulence model may not be corrected using the FI.

Using the area selection approach for the ML part yields improved results while decreasing the number of training samples and thus the computational effort. In addition, the systematic test shows that adding features to the ones that are found in literature improves the ML accuracy. An FCNN with model  $R^2 \approx 0.9$  is obtained, however, the presented HPO does not lead to further improvement. Nevertheless, by applying the resulting ML model within RANS simulations good corrections on steady simulations can be achieved, as long as no extrapolation is necessary.

Generally, the application of a steadily trained ML model within an unsteady simulation is possible, however, with high non-linearities, the simulations do not converge. Furthermore, when strong non-linearities are present, small deviations between a FI- and ML-based steady  $\beta$ -field lead to numerical instabilities for the ML-based approach. The unsteady simulations close to  $k \rightarrow 0$  are just as good as the corresponding steady results, including the derivatives of the steady results. Consequently, regarding the stability and the accuracy of the correction, the FI-based steady  $\beta$ -field approach must be favoured over the ML-based steady  $\beta$ -field approach, which must be favoured over the applied ML model. However, the best-rated approach is only available where steady reference data are available.

# Chapter 5

## Experimental Test Case

Given the findings of the numerical test case in chapter 4, this experimental test case serves the purpose of investigating whether and to what extent the outcomes can be generalised. In contrast to the numerical test case, the necessary steps of the FIML approach are just executed, but no investigations are repeated.

In section 5.1 the experimental data are described and prepared to serve as reference data for the FI in section 5.2. Subsequently, ML models are trained and applied within steady simulations in section 5.3. Finally, section 5.4 conducts an exemplary unsteady simulation.

### 5.1 Case Description and Preparation

Airbus RWC.01\_1 is a database containing wind tunnel measurements of the RAE 2822 airfoil from 2016, the airfoil that is also used for the numerical test case. The scope of the campaign is to validate and extend the measurements by Cook *et al.* [57]. The measurements come from the pilot facility of the European Transonic Wind Tunnel and are made available to the author by the DLR. In contrast to CFD simulations, an experiment cannot be two-dimensional. However, measurements from the test section's centerline are used for this study, and three-dimensional effects are assumed to be negligible. Furthermore, the data are already corrected regarding effects caused by the wind tunnel, e.g. blockage [70].

For each sampling point,  $M$ ,  $Re$ , and  $\alpha$  are known, furthermore, total pressure  $p_{\text{tot}}$  and total temperature  $T_{\text{tot}}$  are known, as these quantities are used to set the REYNOLDS number. The force coefficient in inertial  $z$ -direction is measured. Pressure is measured at 74 locations on the airfoil, 46 on the upper and 28 on the lower side. One pressure sensor constantly produces outliers and must be disregarded. Given the measurements,  $c_p$  can be calculated according to equation A.1 in the Appendix A.

#### 5.1.1 Test Case Selection

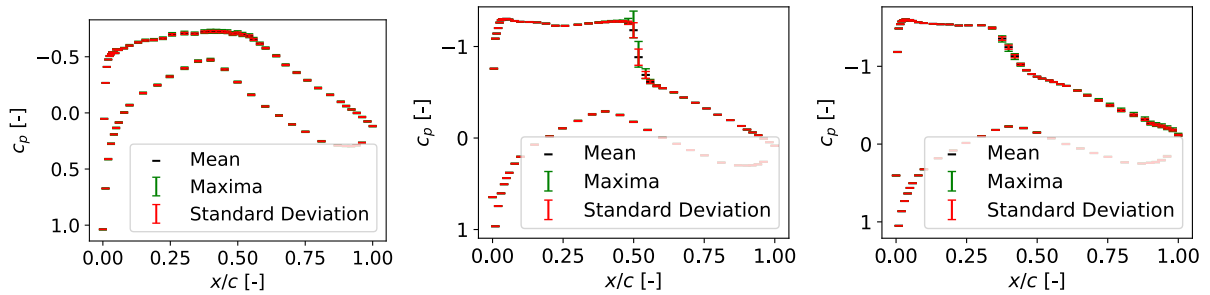
Within the test campaign measurements with fixed transition, caused by flow tripping, and free transition measurements are conducted. As reference data for this test case, free transition data are selected. Just as for the previous RANS simulations of the numerical test case, no transition model for the laminar to turbulent transition is used, i.e., the flow is assumed to be fully turbulent. Even though this means the numerical solution assumes fundamentally different physical behaviours than the reference data, performing an FI with the described conditions might deliver further insights into the technique's capabilities.

Figure A.10 in the Appendix A presents the flow conditions in the database. Overall 7719 measurement points are available. However, approximately 10 measurement points correspond to the same free-stream conditions to account for variance. Data with similar free-stream flow conditions to the numerical test case, i.e. MACH and REYNOLDS number, are selected. Thus, it is tested whether the findings from the numerical test case can be generalised to a different type of reference data without considering entirely new circumstances. The measurement series 488 is a polar with  $M \approx 0.73$ ,  $Re \approx 6.5 \cdot 10^6$  and angles of attack between  $-1.12^\circ$  and  $5.74^\circ$ .

### Averaging

The arithmetic mean is calculated and used since multiple measurements are available at each of the 16 free-stream conditions. Table A.2 in the Appendix A lists the averaged data and the deviations. Deviations from the mean are present and must be kept in mind, however, from this point on, only the mean values are considered. In contrast to a perfect polar with constant free-stream conditions,  $M$  and  $Re$  do slightly decrease with increasing angle of attack.

Figure 5.1 displays three selected averaged  $c_p$ -distributions, as well as the maxima, and the standard deviation. Strong variance in the experimental data can be seen in Subfigure 5.1b at the shock location. Regarding the FI approach, the variance in the reference data must be considered, as the correction can not be more accurate than the reference data. Besides the shock no visibly strong variance is present.



(a)  $M = 0.74$ ,  $\alpha = 0.71^\circ$ , and  $Re = 6.44 \cdot 10^6$ , (b)  $M = 0.72$ ,  $\alpha = 3.10^\circ$ , and  $Re = 6.37 \cdot 10^6$ , and (c)  $M = 0.72$ ,  $\alpha = 5.20^\circ$ , and  $Re = 6.33 \cdot 10^6$ .

**Figure 5.1:**  $c_p$ -distributions of averaged experimental data as well as standard deviation, minima, maxima.

Just as CFD simulations have sources of error, experiments are also imperfect. Nevertheless, from this point onwards, the averaged experimental data are treated as the ground truth.

### 5.1.2 Interpolation of Experimental Data to Numerical Mesh

Spatially distributed FI reference data must be available at the same locations as the ones where CFD solutions are available. However, the locations of the pressure measurements do not coincide with the mesh nodes, thus, an interpolation of the data are necessary. Two possibilities are considered:

1. Linear interpolation: using linear interpolation, the reference data are made available at specified locations of the CFD mesh. This allows to have reference data at

more mesh locations than reference points are available. The original values of the reference data are altered based on an assumption, e.g. linear relationship between value and location.

2. Nearest neighbour: for each reference data point, the nearest neighbouring point in the CFD grid is calculated. Then, the reference data are transferred to the new locations. The reference values remain unchanged, however, for coarse CFD grids larger changes in position might occur. This could have an especially severe influence on the shock location.

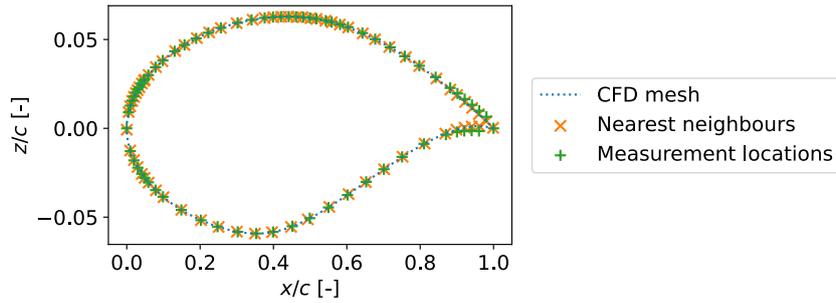


**Figure 5.2:** Nearest neighbours of experimental data in CFD mesh.

Figure 5.2 presents the results of the nearest neighbour approach. Note that only the surface mesh is considered. Furthermore, it must be noted that the experiment uses a thickened trailing edge. Except in the thickened area, differences between the nearest neighbours and the measurement locations are not visible. The CFD mesh appears to be fine enough. Consequently, the nearest neighbour approach is used for further investigations, as it does not alter the reference values in contrast to the interpolation approach.

### 5.1.3 Resulting Data

Given the experimental reference data, CFD solutions with the baseline SA turbulence model are produced analogue to the numerical test case (see subsection 4.1.2). The simulations use the averaged free-stream conditions as an input. In addition to  $M$ ,  $Re$ , and  $\alpha$ , the available information regarding total pressure and total temperature is also passed as an input parameter.

The resulting CFD solutions can be compared to the reference data. The global force in the experiment is measured in the inertial reference system and is only available in  $z$ -direction. In contrast, the RANS solution contains the forces in a body-fixed reference system. Thus, the forces of the corresponding numerical solutions must be transformed into the inertial coordinate system. According to the sketch in Figure A.11 in the Appendix A, the force coefficient in the inertial  $z$ -direction can be calculated using the lift and drag coefficients  $c_l$ ,  $c_d$  and the angle of attack  $\alpha$  (assuming the flow in inertial  $x$ -direction) with the following equation:

$$c_{z,\text{inertial}} = c_l \cdot \cos \alpha - c_d \cdot \sin \alpha. \quad (5.1)$$

In Figure 5.3 a comparison of  $c_{z,\text{inertial}}$  of the experimental data and the SA simulations as well as  $c_l$  of the SA simulations can be seen.  $c_{z,\text{inertial}}$  of the SA simulations contains slightly smaller values than  $c_l$ , however, the differences are very small and especially in the linear region negligible. The measured forces are higher than the SA simulations forces.

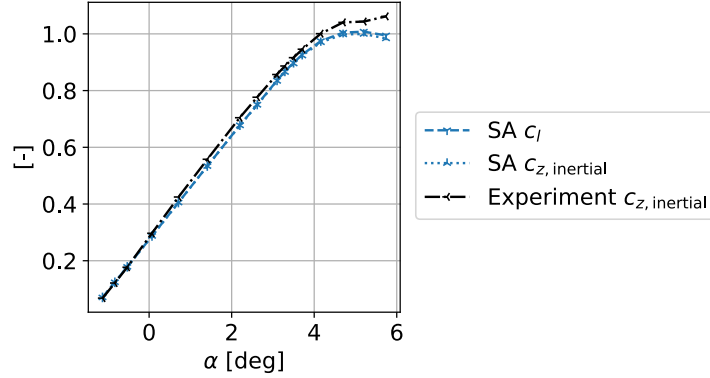


**Figure 5.3:**  $c_{z,\text{inertial}}$  respectively  $c_l$  vs.  $\alpha$  comparing SA simulations and experimental data.

Differences can be seen in the linear as well as in the non-linear region. While for the numerical result a decreasing force for the stall region ( $\alpha > \alpha_{c_l,\text{max}} \approx \alpha_{c_{z,\text{inertial}},\text{max}} \approx 5.20^\circ$ ) can be seen, the experiment shows an untypical behaviour with an increasing force.

Figure 5.4 compares the experimental and SA  $c_p$ -distributions at four selected angles of attack. At  $\alpha = 0.07^\circ$  and  $\alpha = 3.29^\circ$  only small deviations, especially in the post-shock region are present (see subfigures 5.4a and 5.4b). At  $\alpha = 4.70^\circ$  in Subfigure 5.4c a separation bubble was measured behind the shock, this flow feature is not captured in the SA simulation. An entirely different flow behaviour can be seen in Subfigure 5.4d at  $\alpha = 5.20^\circ$ : while the SA solution contains a clear shock, the pressure in the experiment is continuously increasing after the pressure plateau.

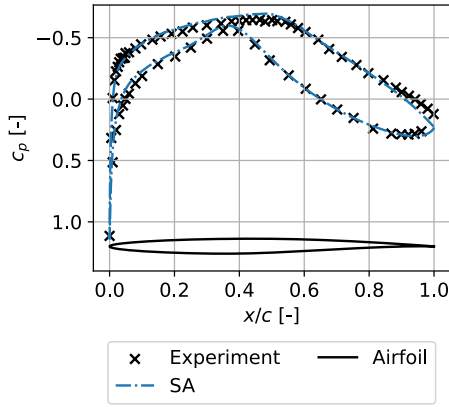
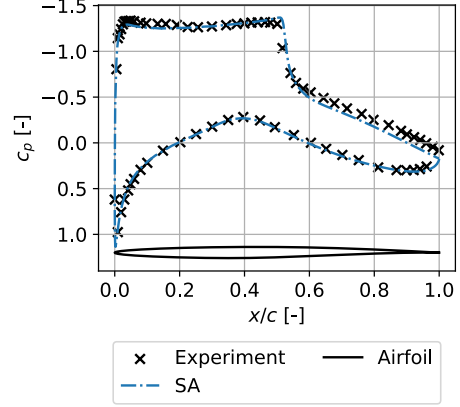
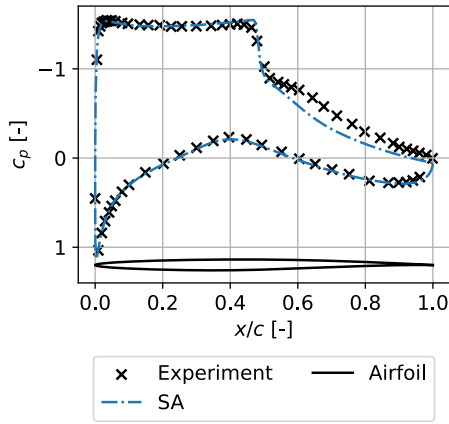
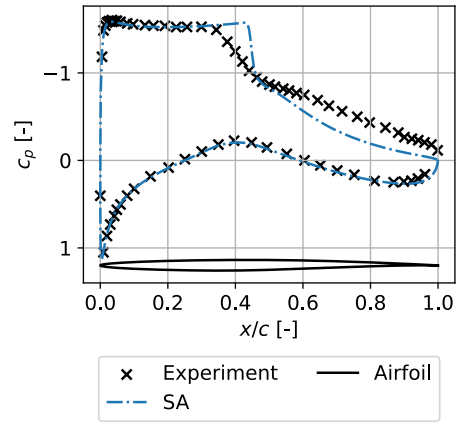
The good match of some  $c_p$ -distribution indicates that the SA simulation is conducted using appropriate settings. However, mismatches between SA and experiment show room for improvement of the SA simulation where the FIML approach is to be applied.

## 5.2 Field Inversion

The general considerations regarding the reference quantity of the FI are similar to the numerical test case and  $c_p$  on the airfoil surface is selected (see subsection 4.2.1). For the experimental test case, no evaluation regarding the amount of reference data are done, and all available measurement points are used.

### 5.2.1 Regularisation

One of the findings of the numerical test case concerns the fact, that the resulting regularisation parameters are all in a very similar range. Thus, the expensive process of producing an L-curve is not done for all data points, but only at two selected ones:  $\alpha = 1.41^\circ$  from the linear region and  $\alpha = 4.70^\circ$  from the non-linear region. To be concise, the resulting plots can be found in the Appendix A. For both cases, the L-curve criterion does not deliver a clear result, thus, an investigation of the pressure distributions is done. For  $\alpha = 1.41^\circ$ , the FI is mostly ineffective and the results are close to the baseline, regardless of  $\lambda$  (see Subfigure A.12a). Based on the L-curve and the pressure distributions of the  $\alpha = 4.70^\circ$  case,  $\lambda_{\text{opt}} = 10^{-12}$  is selected as no further improvement can be achieved with

(a)  $M = 0.74$ ,  $\alpha = 0.07^\circ$ , and  $Re = 6.49 \cdot 10^6$ .(b)  $M = 0.72$ ,  $\alpha = 3.29^\circ$ , and  $Re = 6.42 \cdot 10^6$ .(c)  $M = 0.72$ ,  $\alpha = 4.70^\circ$ , and  $Re = 6.36 \cdot 10^6$ .(d)  $M = 0.72$ ,  $\alpha = 5.20^\circ$ , and  $Re = 6.33 \cdot 10^6$ .**Figure 5.4:** Comparison of  $c_p$ -distributions of experimental data and SA simulation.

smaller regularisation parameters (see Figure A.13). This selection of  $\lambda_{\text{opt}}$  is to some extent subjective, different values might be suitable as well.

## 5.2.2 Resulting Corrections

Regarding the four angles of attack that are compared in subsection 5.1.3, satisfactory corrections are achieved. In Figure A.14 in the Appendix A the FI pressure distributions are presented. As a new flow feature, the post-shock separation bubble that is not present in the numerical test case is corrected using the FI approach.

In Figure 5.5 the  $c_{z,\text{inertial}}-\alpha$ -curve show a good match of the FI result with the experimental reference at negative angles of attack and in the non-linear region. For the two highest angles of attack, the FIs did not converge within a reasonable time, i.e. one week of run time on a high-performance computing cluster. However, corrections in the right direction are visible. In between these regions, the FI does not lead to improvements, a worsening of the results can be seen.

To further investigate one of the cases with a bad FI performance, the surface pressure and the turbulent eddy viscosity field at  $\alpha = 1.41^\circ$  are visualised in Figure 5.6. The  $c_p$ -distribution shows different flow behaviours for the experimental and the numerical data (see Subfigure 5.6a): while the numerical solutions contain a small shock, this is not visible in the experimental data. The fully turbulent numerical approach does not

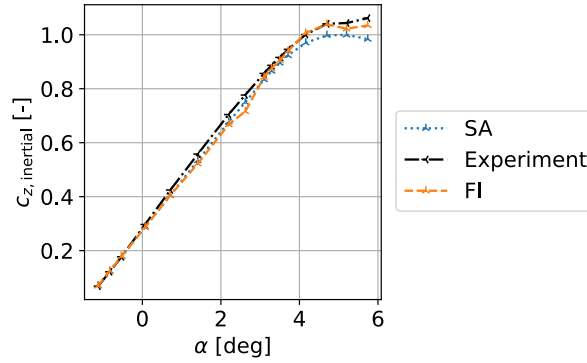
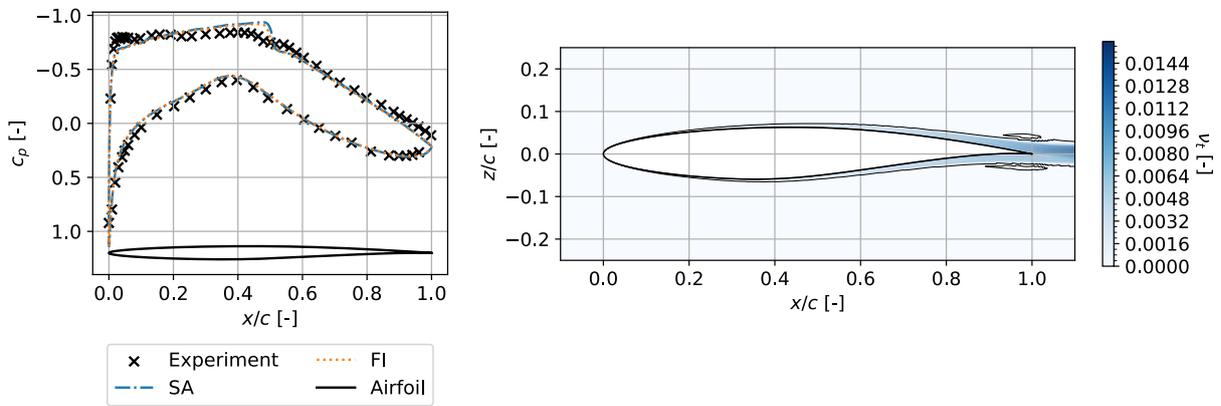


**Figure 5.5:**  $c_{z,\text{inertial}}$  vs.  $\alpha$  comparing SA simulations, experimental data, and FI result.



(a)  $c_p$ -distribution.

(b)  $\nu_t$  with contour lines at  $\nu_t = 10^{-4}$ .

**Figure 5.6:**  $M = 0.73$ ,  $\alpha = 1.41^\circ$ , and  $Re = 6.45 \cdot 10^6$ .

match the free-transition experiment with laminar flow close to the leading edge. The turbulent eddy viscosity plot shows that the turbulent model does not affect the flow close to the leading edge. Thus, the FI is also ineffective in this area and not able to match the experimental pressure distribution.

Overall, the findings regarding FI from the numerical test case are confirmed using the experimental data: the approach can lead to good corrections of the turbulence model, but is not capable of correcting differences that are not caused by the turbulence model. Nevertheless, the obtained data are used for further study to evaluate the impact on the next steps of the FIML approach.

## 5.3 Machine Learning and Application to Steady Simulation

Investigations regarding the ML model use the results from the numerical test case (see section 4.3): the same FCNN model structure, input features, area selection approach, and trainer settings as for model no. 11 from Table 4.5 are considered.

### 5.3.1 Application Model Trained on Numerical Data

Before an FCNN is trained on the experimental data, the final model from the numerical test case is applied to correct the simulations of this test case. The application of the model within the steady RANS simulations is analogue to section 3.5 and therefore not further described here. Figure 5.7 presents the effect of the correction model on  $c_{z,\text{inertial}}$ . The correction is not successful. The resulting curve matches the SA simulation or does result in corrections in the wrong direction. Selected pressure distributions might be found in the Appendix A in Figure A.15 and confirm the result. Small corrections of the shock position and the post-shock pressure distribution are corrected in the numerical test case. Stronger deviations, with additional features such as separation bubbles, can not be corrected, as these features are not seen during training. Consequently, the application of the ML model, trained along one polar, to an unseen polar with a different kind of reference data are not suitable.

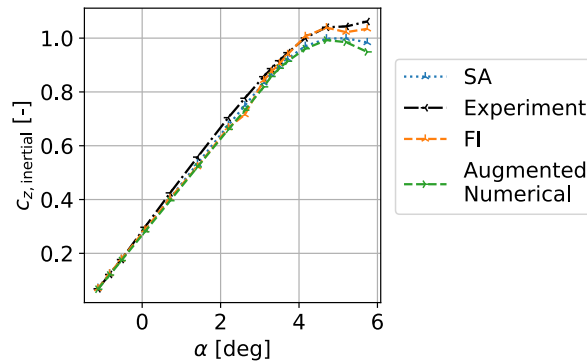


**Figure 5.7:**  $c_{z,\text{inertial}}$  vs.  $\alpha$  comparing SA simulations, experimental data, FI result, and augmented SA simulation using the ML model trained on the numerical test case.

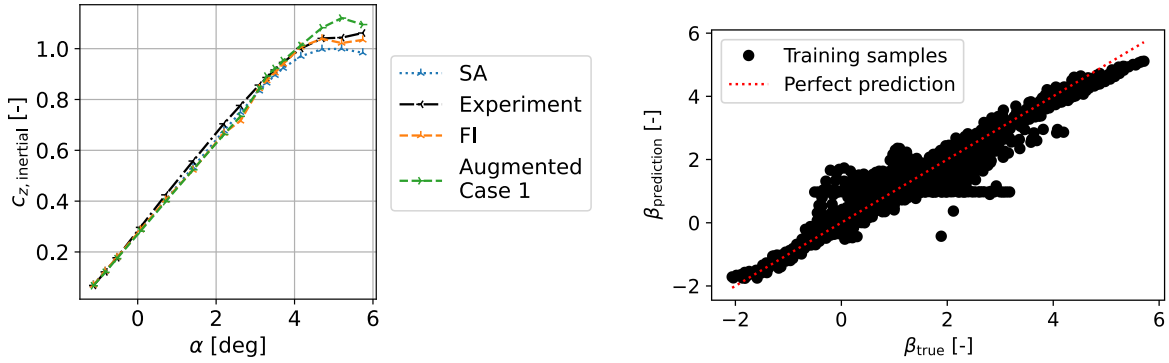
### 5.3.2 Training and Application of ML Model using Experimental Data

Two FCNNs are trained using the available FI results from section 5.2. Taking into account that the two FIs at  $\alpha > 5.0^\circ$  are not converged, the first FCNN *case 1* takes the entire polar into account, and the second FCNN *case 2* excludes the unconverged FIs from the training data.

#### Case 1

Following the prior considerations, the ML model case 1 is trained on every second angle of attack. Subfigure 5.8b presents the prediction accuracy regarding the training data (30% of the training data are used for validation during training). The predictions in the plot are close to perfect prediction, however, some variance can be seen. Furthermore, numerous mispredictions with  $\beta \approx 1$  can be seen. The prediction metrics on the training data of  $R^2 = 0.907$ ,  $\text{MAE} = 11.80 \cdot 10^{-3}$ , and  $\text{MSE} = 2.62 \cdot 10^{-3}$  are partially close to the numerical test case and partially below.

Subfigure 5.8a presents the  $c_{z,\text{inertial}}$  predictions. The augmented simulations match the SA simulations in the linear region. Within the non-linear region, a severe overprediction of the force coefficient can be seen.



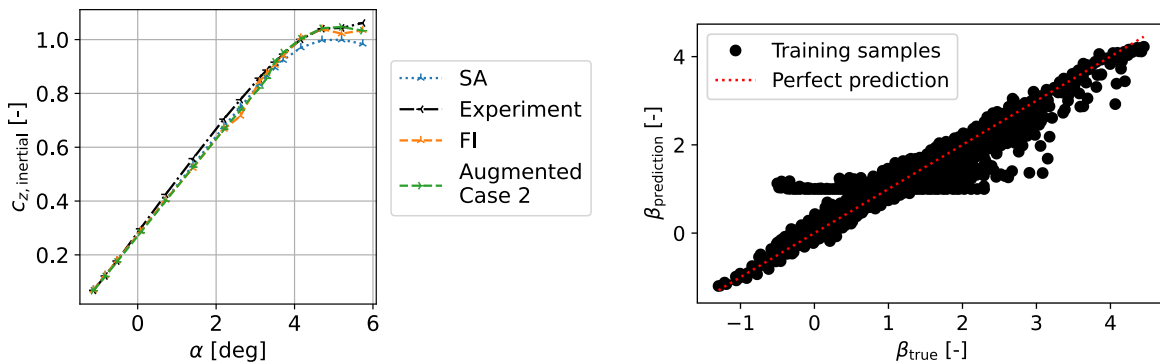
(a)  $c_{z,inertial}$  vs.  $\alpha$  comparing SA simulations, (b) Predicted versus true target values from experimental data, FI result, and augmented SA simulation using the ML model case 1.

**Figure 5.8:** Experimental FCNN case 1.

In Figure A.16 in the Appendix A selected  $c_p$ -distributions are displayed. Except at very small angles of attack the ML model predictions do not match with the FI, the SA simulation or the reference data. Despite the mediocre metrics, the applied ML model can not capture the underlying structures in the flow.

## Case 2

One possibility to improve the ML model might be to exclude the FIs that are not converged from the training data, as these might deliver skewed information. Training the model on every second angle of attack with  $\alpha < 5.0^\circ$  results in the following metrics:  $R^2 = 0.891$ ,  $MAE = 8.67 \cdot 10^{-3}$ , and  $MSE = 1.45 \cdot 10^{-3}$ . The improved MAE and MSE come with the prediction distribution in Subfigure 5.9b. Regarding the force coefficient, a similar behaviour to FCNN case 1 can be seen in the linear region in Subfigure 5.9a. Nevertheless, in the non-linear region, a clear improvement is visible. The augmented result is close to the reference, however, not perfect.

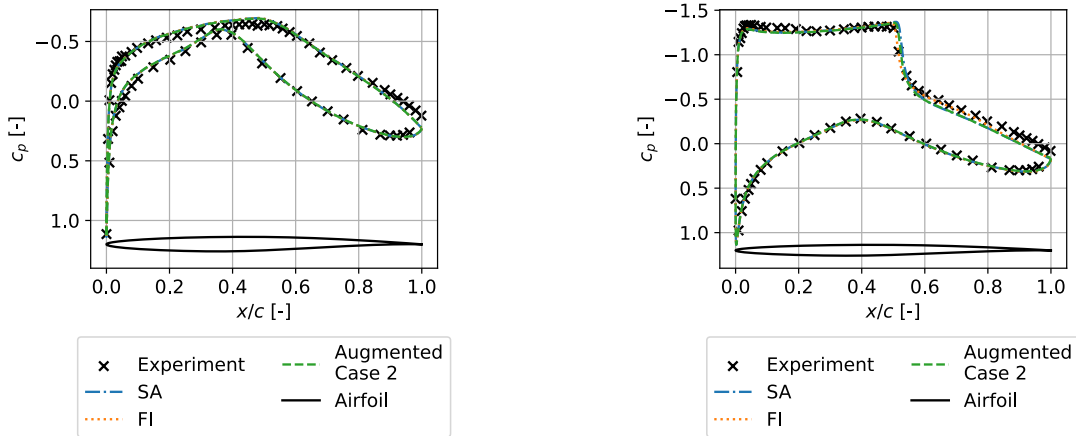


(a)  $c_{z,inertial}$  vs.  $\alpha$  comparing SA simulations, (b) Predicted versus true target values from experimental data, FI result, and augmented SA simulation using the ML model case 2.

**Figure 5.9:** Experimental FCNN case 2.

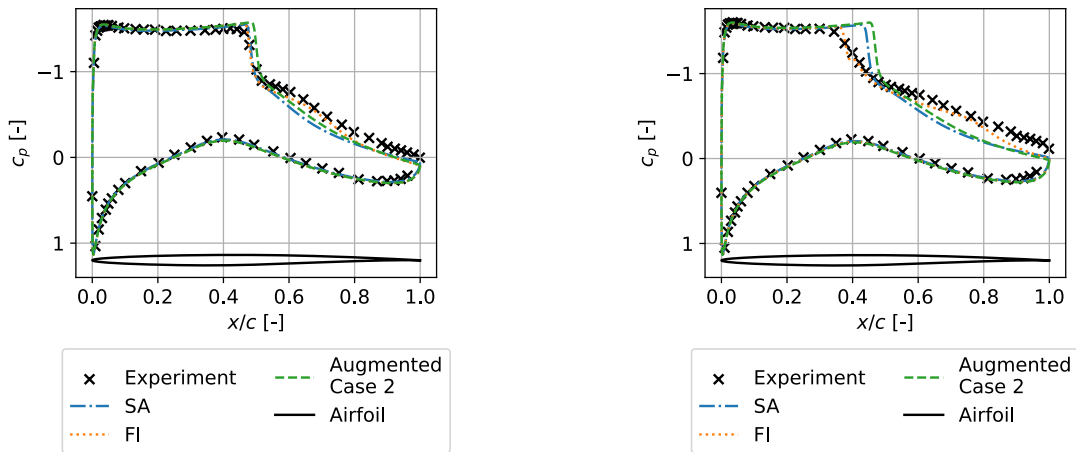
Comparing the  $c_p$ -distributions of this case (see Figure 5.10) to the ones of case 1 (see Figure A.16 in the Appendix A), an improvement can be seen. While FCNN case 1 predicts kinks in the shocks, this attempt gives a good correction of the shock position in some cases, e.g. at  $\alpha = 4.70^\circ$  in Subfigure 5.10c. However, a correction of the separation bubble is not achieved. Furthermore, for the cases that are excluded from the training data, e.g.  $\alpha = 5.2^\circ$  in Subfigure 5.10d, flow features such as the steadily increasing pressure after the pressure plateau are not covered by the correction.

A comparison of the  $\beta$ -fields that are predicted and that are a result of the FI backs up the finding that the ML model is not able to capture all the flow features (see Figure A.17 in the Appendix A).



(a)  $M = 0.74$ ,  $\alpha = 0.07^\circ$ , and  $Re = 6.49 \cdot 10^6$ .

(b)  $M = 0.72$ ,  $\alpha = 3.29^\circ$ , and  $Re = 6.42 \cdot 10^6$ .



(c)  $M = 0.72$ ,  $\alpha = 4.70^\circ$ , and  $Re = 6.36 \cdot 10^6$ .

(d)  $M = 0.72$ ,  $\alpha = 5.20^\circ$ , and  $Re = 6.33 \cdot 10^6$ .

**Figure 5.10:** Comparison of  $c_p$ -distributions of experimental data, SA simulation, FI, and ML model case 2.

No satisfactory ML model could be trained. Important flow features, such as the separation bubble, are not covered by the models. Thus, a simple transfer of the ML model to the experimental test case is not possible. Next to a reevaluation of hyperparameters of the model, the input features could potentially be a factor that significantly influences the outcome and should therefore undergo a repeated feature selection. However, these improvements are not done within this thesis.

## 5.4 Exemplary Unsteady Simulation

Given the non-satisfactory results regarding unsteady augmented simulations (see section 4.6), the lack of generalizability of the ML model (see section 5.3), and the fact that no experimental unsteady reference data for the RAE2822 airfoil are available to the author, a profound study of unsteady augmented simulations for the experimental test case is not meaningful. Nevertheless, one exemplary unsteady simulation is conducted to show that generally, a correction of unsteady simulations with experimental reference data are possible. Correcting unsteady simulations with a steady FI-based  $\beta$ -field leads to the best results on the numerical test case, furthermore, the FI can deliver a good correction for the steady simulations of the experimental test case. Thus, a correction based on a steady FI-based  $\beta$ -field is chosen for the exemplary unsteady simulation.

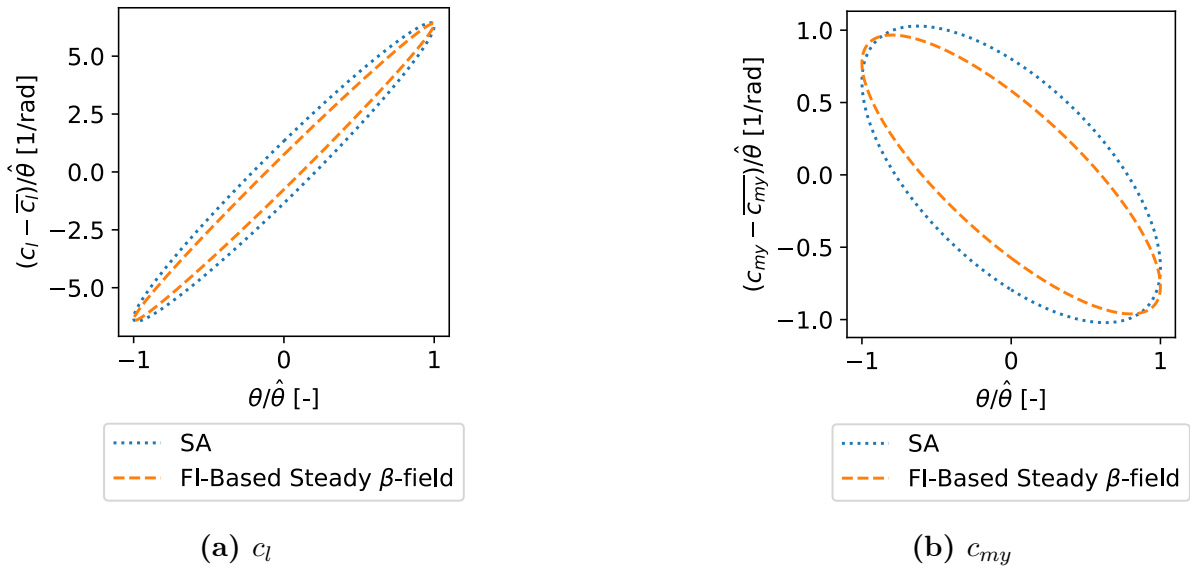


**Figure 5.11:** Hysteresis plot due to pitch excitation for experimental test case at  $\alpha = 4.16$ ,  $k = 0.3$ , and  $\hat{\alpha} = 0.001^\circ$ .

The unsteady simulations lead to the hysteresis plots in Figure 5.11 with oscillations around the following mean coefficients:  $\bar{c}_{l,SA} = 0.975$ ,  $\bar{c}_{l,FI\text{-based steady } \beta\text{-field}} = 1.012$ ,  $\bar{c}_{my,SA} = -0.086$ , and  $\bar{c}_{my,FI\text{-based steady } \beta\text{-field}} = -0.096$ . Even though no reference data are available one can notice that the mean values of  $c_l$  are close to steady  $c_{z,inertial}$  values in Figure 5.5. Note that the differences between  $c_l$  and  $c_{z,inertial}$  are very small. An evaluation of the hysteresis plot without reference data are not useful, however, a change in the shape of the curves can be seen.

## 5.5 Findings

This section gives a summary of the findings of chapter 5. The full conclusion is available in chapter 6.

Using a fixed value for  $\lambda$  reduces the computational effort, however, two FIs did not converge, possibly this could be prevented by individual evaluations of the regularisation. The chosen structure of the FI is not able to correct effects that are not due to the turbulence model itself, e.g. transition. Thus, restrictions are not caused by the type of

---

reference data, e.g. experimental or numerical, but rather by the physical effects in the reference data.

An application of the ML model trained on the numerical test case to the experimental test case does not produce accurate results. However, using the considerations regarding the ML model from the numerical test case enables correcting flow features that are present in the numerical test case, but additional features, e.g. separation bubbles, are not covered. Furthermore, the exclusion of FIs that did not reach convergence from the training data benefits the prediction accuracy.

Generally, corrections on unsteady simulations with experimental reference data seem to be possible. However, only an example test case with a low informative value is examined.

# Chapter 6

## Conclusions and Outlook

### 6.1 Conclusions

The main objective of this thesis is to investigate if the field inversion and machine learning (FIML) methodology can correct turbulence models such that improved predictions at steady transonic flow conditions including shocks are obtained and how this affects a subsequent unsteady response analysis. This thesis uses two test cases that build upon each other to investigate different aspects of the FIML approach regarding steady and unsteady simulations.

#### Summary of Results

Using the two-dimensional RAE 2822 airfoil, a first test case is designed to correct the SPALART-ALLMARAS (SA) turbulence model with the FIML approach and higher fidelity numerical reference data based on REYNOLDS-averaged NAVIER-STOKES (RANS) equations closed with a REYNOLDS stress model (RSM). Steady RANS simulations with varying angles of attack are generated at transonic flight conditions including shocks:  $M = 0.75$ ,  $Re = 6.0 \cdot 10^6$ . Sampling data points along one polar is chosen to gain information about how the flow fields and the associated FIML correction change with the angle of attack. A dataset containing baseline and reference data with small differences in the linear region and stronger differences in the non-linear region is generated.

Before applying the field inversion (FI) approach to the test case dataset, several investigations with regard to a realistic application are conducted. Considering typical experimental set-ups  $c_p$  on the airfoil's surface is selected as a reference quantity. A study regarding the number of reference points shows an increasing error for very small numbers of reference points and convergence issues if the number of reference points is too high. The accuracy of the FI depends on the resolution of the flow phenomena that require correction, however, this is not known *a priori*. For the present test case, 32 to 64 reference points on the airfoil's surface deliver a good compromise between accuracy and computational effort. Corrections based on a reference quantity deliver good results regarding the reference quantity and related variables, however, no satisfactory correction of unrelated quantities can be achieved. Furthermore, the FI approach is limited to correcting inadequacies caused by the turbulence model, e.g. a correction of deviations due to differing free-stream conditions is not possible. Given the results of the investigations FIs for the test case dataset are performed. Good correction results at all angles of attack with small imperfections at the trailing edge of the airfoil are achieved.

Considerations regarding the resulting imbalanced dataset with overrepresented  $\beta \approx 1$  samples and the selection of input features are discussed before two generic ML models are trained: a fully-connected neural network (FCNN) and an interpolation model based on radial basis functions. Most promising results are achieved using the FCNN in a selected

area around the airfoil. Starting from a set of features found in literature a set of 12 locally available, dimensionless, partially non-GALILEAN invariant features is selected based on the correlation to the target quantity. No improvements are achieved trying to tune the FCNN within a hyperparameter optimisation. Given the investigations, the resulting FCNN achieves a coefficient of determination  $R^2 \approx 0.9$  when predicting the correction field at two selected test angles of attack. Applying the resulting model within a RANS simulation leads to corrected  $c_p$ -distributions as well as qualitative and quantitative improvements of the force coefficients  $c_l$ ,  $c_d$ , and  $c_{my}$ . Decreased accuracy in cases with extrapolation can be seen.

The ML model that implicitly knows  $d\beta/d\alpha$  as a consequence of training it along one polar is applied to correct unsteady dual time-stepping RANS simulations with a harmonically pitching airfoil. Additionally, the influence of applying steady  $\beta$ -fields as an alternative correction method is evaluated. At a small mean angle of attack with small deviations between SA and RSM, the correction approaches yield small or no deterioration over the baseline solution, as long as the amplitude is small enough. For cases with strong differences between SA and RSM, steady  $\beta$ -fields lead to better results than the application of the FCNN model. With strong non-linearities in the flow field, the unsteady simulations using the ML model or an ML-based steady  $\beta$ -field do not converge. The correction using an FI-based steady  $\beta$ -field yields good corrections where the excitation amplitudes are smaller than one degree. For the quasi-steady case, the resulting corrections are consistent with the steady simulations. Here, not only the quantities of interest but also their derivatives with respect to the angle of attack are important.

A second test case with experimental reference data from wind tunnel measurements of the RAE 2822 is designed in such a way that the findings of the numerical test case can be examined regarding their generalisability towards experimental data sources. Data with similar free-stream conditions to the first test case are selected and transferred to the numerical mesh using a nearest neighbour approach. The findings regarding FI confirm the outcome of the first test case: differences unrelated to the turbulence model, e.g. laminar flow, cannot be corrected using the chosen FIML approach. However, additional flow features such as post-shock separation bubbles are corrected. An easy transfer of the ML approach to this test case is not possible. The post-shock separation bubble is not captured. Thus, considerations that are specific to flows along one polar do not easily generalise.

### Evaluation Regarding the Research Objective

After summarizing and reviewing the findings of this thesis, statements regarding the research (sub-)objectives stated in the introduction can be made. Therefore, four takeaway points are formulated to give a concise overview of the main outcomes of this thesis:

- By using FI for **inadequacies caused by the SA turbulence model** in transonic flow fields including shocks, accurate corrections of the **reference quantity and related quantities** can be achieved with a **realistic number of reference points**.
- Training an **FCNN** to give a node-wise prediction of the correction factor  $\beta$  and applying the model within a RANS solver yields **accurate results** as long as **no extrapolation** is required. The biggest improvements regarding the ML model are achieved by the **local application** of the correction approach and the usage of **additional features**.

- Applying **steady  $\beta$ -fields** to correct unsteady simulations delivers good results for excitation amplitudes up to at least one degree. Applying the **ML model** is not only inferior regarding the accuracy but in some cases with strong non-linearities also regarding the **convergence** of the numerical simulation. The accuracy of all tested correction approaches is **limited by the performance on the corresponding steady** cases.
- A general strategy for **handling experimental reference data** is presented. However, especially the considerations for the **ML model lack generalisability** towards new flow features.

## 6.2 Outlook

The investigations in this thesis answer many questions, especially, a first step towards the application of the steady FIML approach within unsteady dual time-stepping simulations is made. However, many more questions arise and give motivation for further work. Some ideas are stated below, separated into four categories.

### Test Case Design

The design of the test cases within this thesis is well-reasoned by the idea of applying a model with knowledge about  $d\beta/d\alpha$  of the steady simulations to unsteady simulations and delivers accurate results for the given steady data. However, the transfer of the model to the second test case shows that the limited design of experiments comes with the cost of decreased generalisability. Thus, the question arises of whether including not only differing angles of attack but also multiple free-stream conditions, varying data sources, and multiple airfoil geometries benefits the process of feature selection and the generalisability of the resulting model. Not only the effect on steady simulations but also the subsequent unsteady analysis is of interest.

Furthermore, the evaluation of the correction of unsteady simulations within this thesis is limited by the underlying assumptions of unsteady RANS simulations, as both, reference and baseline data, are numerical. Thus, an investigation of an experimental test case including unsteady reference data would be interesting.

### Field Inversion

Regarding the correction of the reference quantity, the FIML approach fulfils the expectations with small inadequacies, e.g. at the trailing edge. One possible improvement could be to spend even more effort on the selection of the regularisation parameter with more values in the test range.

Correcting  $c_f$  using  $c_p$  as reference quantity does not yield good results. Thus, evaluating the influence of additional reference quantities might be beneficial. However, the availability of reference quantities must be regarded.

The accuracy of the correction of unsteady simulations seems to depend not only on the values of the quantities of interest but also on their derivatives with respect to the angle of attack. Improving the accuracy of the FIs even more could be of benefit. One possible idea is to apply a correction factor not only to the production term but also to other

parts, e.g. the diffusive transport. However, this would also change the complexity of the inverse mathematical problem.

### Machine Learning

The area selection approach in this thesis leads to a big improvement regarding the prediction accuracy of the FCNN. A robust and simple design is present. An investigation regarding a more refined area selection, e.g. using a sensor function to determine correction-worthy areas, could deliver an accuracy improvement.

The feature selection approach delivers good results for the first test case. However, the lack of generalisability towards different flow conditions, such as separation bubbles, indicates room for improvement. This could be achieved by evaluating more variables as possible features, and by incorporating additional test cases into the correlation analysis of the feature selection approach.

FCNNs are powerful tools, however, advancements within the field of ML such as graph neural networks, that use spatial information, are worth investigating. Another way to improve a selected ML methodology could be to run an HPO to a further extent than within this thesis.

### Unsteady Simulations

Convergence issues can be seen for the ML-based correction approaches on unsteady simulations. This thesis investigates a variety of, but not all, settings of the unsteady numerical method. A wider study with more settings would be of interest.

Furthermore, the test design in this thesis is targeted to be applied to an unsteady pitching motion. Other types of motions, e.g. heave, or combinations of motion types, are yet to be investigated. Not only an effect regarding the unsteady simulations but also on the required steady simulations are of interest.

Solving the unsteady RANS equations in a dual-time stepping scheme is computationally very expensive. The linear frequency domain (LFD) method is computationally much more efficient by solving a linearised version of the governing equations. Thus, an investigation regarding the applicability of FIML towards LFD is of interest [71].

Finally, a study of a fully unsteady FIML Direct approach exists [20]. A reproduction and extension of the results could be a way forward towards improved unsteady simulations. However, this requires an unsteady adjoint method to evaluate gradients with respect to time-dependent values. This is currently not implemented within TAU. In contrast to the approach presented in this thesis a fully unsteady FIML approach should theoretically not be limited to a range of amplitudes or reduced frequencies by taking unsteady effects into account.

# Bibliography

- [1] T. Mauery *et al.*, „A 20-year vision for flight and engine certification by analysis“, in *AIAA SCITECH 2022 Forum*. DOI: 10.2514/6.2022-1553.
- [2] European Union Aviation Safety Agency (EASA), „Certification Specifications and Acceptable Means of Compliance for Large Aeroplanes (CS-25), Amendment 27“, 2021.
- [3] J. SMAGORINSKY, „General circulation experiments with the primitive equations: I. the basic experiment“, *Monthly Weather Review*, vol. 91, no. 3, pp. 99–164, 1963. DOI: 10.1175/1520-0493(1963)091<0099:GCEWTP>2.3.CO;2.
- [4] J. Anderson, *Computational Fluid Dynamics: The Basics with Applications* (McGraw-Hill International Editions: Mechanical Engineering). McGraw-Hill, 1995, ISBN: 9780071132107.
- [5] J. P. Slotnick *et al.*, „Cfd vision 2030 study: A path to revolutionary computational aerosciences“, *NASA Technical Report*, no. NASA/CR-2014-218178, 2014.
- [6] S. L. Brunton, B. R. Noack and P. Koumoutsakos, „Machine Learning for Fluid Mechanics“, *Annual Review of Fluid Mechanics*, vol. 52, no. 1, pp. 477–508, 2020. DOI: 10.1146/annurev-fluid-010719-060214.
- [7] E. J. Parish and K. Duraisamy, „A paradigm for data-driven predictive modeling using field inversion and machine learning“, *Journal of Computational Physics*, vol. 305, pp. 758–774, 2016, ISSN: 0021-9991. DOI: <https://doi.org/10.1016/j.jcp.2015.11.012>.
- [8] K. Duraisamy, G. Iaccarino and H. Xiao, „Turbulence modeling in the age of data“, *Annual review of fluid mechanics*, vol. 51, pp. 357–377, 2019, ISSN: 1545-4479. DOI: <https://doi.org/10.1146/annurev-fluid-010518-040547>.
- [9] J. Ling and J. Templeton, „Evaluation of machine learning algorithms for prediction of regions of high Reynolds averaged Navier Stokes uncertainty“, *Physics of Fluids*, vol. 27, no. 8, p. 085103, Aug. 2015, ISSN: 1070-6631. DOI: 10.1063/1.4927765.
- [10] J.-X. Wang, J.-L. Wu and H. Xiao, „Physics-informed machine learning approach for reconstructing reynolds stress modeling discrepancies based on dns data“, *Phys. Rev. Fluids*, vol. 2, p. 034603, 3 Mar. 2017. DOI: 10.1103/PhysRevFluids.2.034603.
- [11] J.-L. Wu, H. Xiao and E. Paterson, „Physics-informed machine learning approach for augmenting turbulence models: A comprehensive framework“, *Phys. Rev. Fluids*, vol. 3, p. 074602, 7 Jul. 2018. DOI: 10.1103/PhysRevFluids.3.074602.
- [12] J. Ling, A. Kurzawski and J. Templeton, „Reynolds averaged turbulence modelling using deep neural networks with embedded invariance“, *Journal of Fluid Mechanics*, vol. 807, pp. 155–166, 2016. DOI: 10.1017/jfm.2016.615.

- [13] M. Gamahara and Y. Hattori, „Searching for turbulence models by artificial neural network“, *Phys. Rev. Fluids*, vol. 2, p. 054604, 5 May 2017. DOI: 10.1103/PhysRevFluids.2.054604.
- [14] A. Beck, D. Flad and C.-D. Munz, „Deep neural networks for data-driven LES closure models“, *Journal of Computational Physics*, vol. 398, p. 108910, 2019, ISSN: 0021-9991. DOI: <https://doi.org/10.1016/j.jcp.2019.108910>.
- [15] F. Jäckel, „Sensitivity analysis of discrepancy terms introduced in turbulence models using field inversion“, in *22nd STAB/DGLR Symposium on New Results in Numerical and Experimental Fluid Mechanics XIII*, A. Dillmann, G. Heller, E. Krämer and C. Wagner, Eds., ser. Notes on Numerical Fluid Mechanics and Multidisciplinary Design, vol. 151, Springer Nature, Jul. 2021, pp. 625–634. [Online]. Available: <https://elib.dlr.de/136236/>.
- [16] C. Grabe, F. Jäckel, P. Khurana and R. Dwight, „Data-driven augmentation of a rans turbulence model for transonic flow prediction“, *International Journal of Numerical Methods for Heat and Fluid Flow*, vol. 33, no. 4, emerald insight, Ed., pp. 1544–1561, Apr. 2023. [Online]. Available: <https://elib.dlr.de/194686/>.
- [17] J. R. Holland, J. D. Baeder and K. Duraisamy, „Field inversion and machine learning with embedded neural networks: Physics-consistent neural network training“, in *AIAA Aviation 2019 Forum*. DOI: 10.2514/6.2019-3200.
- [18] F. Jäckel, „A closed-form correction for the spalart-allmaras turbulence model for separated flows“, in *AIAA SciTech 2022 Forum*, AIAA, Ed., AIAA 2022-0462 Session: RANS/LES/Hybrid Turbulence Modeling of Separated Flow I, ARC, Jan. 2022, pp. 1–20. [Online]. Available: <https://elib.dlr.de/148403/>.
- [19] K. J. Fidkowski, „Gradient-based shape optimization for unsteady turbulent simulations using field inversion and machine learning“, *Aerospace Science and Technology*, vol. 129, p. 107843, 2022, ISSN: 1270-9638. DOI: <https://doi.org/10.1016/j.ast.2022.107843>.
- [20] L. Fang and P. He, „Field inversion machine learning augmented turbulence modeling for time-accurate unsteady flow“, *Physics of Fluids*, vol. 36, no. 5, p. 055117, May 2024, ISSN: 1070-6631. DOI: 10.1063/5.0207704.
- [21] U. Command and H. Hurt, *Aerodynamics for Naval Aviators*. CreateSpace Independent Publishing Platform, 2015, pp. 201–242, ISBN: 9781508489481. [Online]. Available: <https://books.google.de/books?id=YCIkrgeEACAAJ>.
- [22] N. D. Sandham, „Shock wave-boundary layer interactions“, in *Turbulent Shear Layers in Supersonic Flow*. New York, NY: Springer New York, 2006, pp. 319–363, ISBN: 978-0-387-26305-2. DOI: 10.1007/0-387-26305-5\_10.
- [23] „Full-potential, euler, and navier-stokes schemes“, in *Applied Computational Aerodynamics*, pp. 39–88. DOI: 10.2514/5.9781600865985.0039.0088.
- [24] Ü. Gülçat, „Introduction“, in *Fundamentals of Modern Unsteady Aerodynamics*. Cham: Springer International Publishing, 2021, pp. 1–23, ISBN: 978-3-030-60777-7. DOI: 10.1007/978-3-030-60777-7\_1.

- [25] D. Nixon, A. I. of Aeronautics and Astronautics, *Unsteady Transonic Aerodynamics* (Progress in astronautics and aeronautics). American Institute of Aeronautics and Astronautics, 1989, ISBN: 9780930403522. [Online]. Available: <https://books.google.de/books?id=2kkxtgEACAAJ>.
- [26] E. Albano and W. P. Rodden, „A doublet-lattice method for calculating lift distributions on oscillating surfaces in subsonic flows.“, *AIAA Journal*, vol. 7, no. 2, pp. 279–285, 1969. DOI: 10.2514/3.5086.
- [27] A. Jameson, „Application of dual time stepping to fully implicit runge kutta schemes for unsteady flow calculations“, in *22nd AIAA Computational Fluid Dynamics Conference*. DOI: 10.2514/6.2015-2753.
- [28] D. Schwamborn, A. Gardner, H. von Geyr, A. Krumbein, H. Lüdeke and A. Stürmer, „Development of the tau-code for aerospace applications“, in *50th NAL International Conference on Aerospace Science and Technology*, 2008. [Online]. Available: <https://elib.dlr.de/55519/>.
- [29] Y. Yang and K. Pahlke, „Implementation of a dual-time stepping method for the numerical solution of n-s equations for rigid airfoils in arbitrary unsteady motion“, Tech. Rep., 1995, LIDO-Berichtsjahr=1996, [Online]. Available: <https://elib.dlr.de/36429/>.
- [30] D. Wilcox, *Turbulence Modeling for CFD* (Turbulence Modeling for CFD Bd. 1). DCW Industries, 2006, ISBN: 9781928729082. [Online]. Available: <https://books.google.de/books?id=tFNNPgAACAAJ>.
- [31] P. Spalart and S. Allmaras, „A one-equation turbulence model for aerodynamic flows“, in *30th Aerospace Sciences Meeting and Exhibit*. DOI: 10.2514/6.1992-439.
- [32] S. Allmaras, F. Johnson and P. Spalart, „Modifications and clarifications for the implementation of the spalart-allmaras turbulence model“, Jan. 2012, pp. 1–11.
- [33] S. Braun, „Implementation of a  $\ln(\omega)$ -based SSG/LRR reynolds stress model into the DLR-TAU code“, Deutsches Zentrum für Luft- und Raumfahrt e.V., Tech. Rep., Mar. 2019. [Online]. Available: <https://elib.dlr.de/193446/>.
- [34] J. C. Rotta, „Statistische Theorie nichthomogener Turbulenz“, *Zeitschrift für Physik*, vol. 131, pp. 51–77, 1951. DOI: <https://doi.org/10.1007/BF01330059>.
- [35] C. C. Shir, „A Preliminary Numerical Study of Atmospheric Turbulent Flows in the Idealized Planetary Boundary Layer.“, *Journal of the Atmospheric Sciences*, vol. 30, no. 7, pp. 1327–1339, Oct. 1973. DOI: 10.1175/1520-0469(1973)030<1327:APNS0A>2.0.CO;2.
- [36] F. R. Menter, „Two-equation eddy-viscosity turbulence models for engineering applications“, *AIAA Journal*, vol. 32, no. 8, pp. 1598–1605, 1994. DOI: 10.2514/3.12149.
- [37] A. N. Tikhonov *et al.*, „On the stability of inverse problems“, in *Dokl. akad. nauk sssr*, vol. 39, 1943, pp. 195–198.

- [38] A. Tikhonov and V. Arsenin, *Solutions of Ill-posed Problems* (Halsted Press book). Winston, 1977, ISBN: 9780470991244. [Online]. Available: <https://books.google.de/books?id=ECrvAAAAMAAJ>.
- [39] M. B. Giles and N. A. Pierce, „An introduction to the adjoint approach to design“, *Flow, Turbulence and Combustion*, vol. 65, pp. 393–415, 2000. [Online]. Available: <https://api.semanticscholar.org/CorpusID:8351546>.
- [40] J. Nocedal and S. Wright, *Numerical Optimization* (Springer Series in Operations Research and Financial Engineering). Springer New York, 2006, ISBN: 9780387400655. [Online]. Available: <https://books.google.de/books?id=VbHYoSye1FcC>.
- [41] L. Armijo, „Minimization of functions having Lipschitz continuous first partial derivatives.“, *Pacific Journal of Mathematics*, vol. 16, no. 1, pp. 1–3, 1966.
- [42] G. E. Moore, „Cramming more components onto integrated circuits, reprinted from electronics, volume 38, number 8, april 19, 1965, pp.114 ff.“, *IEEE Solid-State Circuits Society Newsletter*, vol. 11, no. 3, pp. 33–35, 2006. DOI: 10.1109/N-SSC.2006.4785860.
- [43] I. Goodfellow, Y. Bengio and A. Courville, *Deep Learning*. MIT Press, 2016, <http://www.deeplearningbook.org>.
- [44] Y. LeCun, Y. Bengio and G. Hinton, „Deep learning“, *nature*, vol. 521, no. 7553, p. 436, 2015.
- [45] C. Spearman, „The proof and measurement of association between two things“, *American Journal of Psychology*, vol. 15, pp. 88–103, 1904.
- [46] D. W. Aha and R. L. Bankert, „A comparative evaluation of sequential feature selection algorithms“, in *Learning from Data: Artificial Intelligence and Statistics V*, D. Fisher and H.-J. Lenz, Eds. New York, NY: Springer New York, 1996, pp. 199–206, ISBN: 978-1-4612-2404-4. DOI: 10.1007/978-1-4612-2404-4\_19.
- [47] P. Bekemeyer *et al.*, „Data-driven aerodynamic modeling using the DLR SMARTy toolbox“, in *AIAA AVIATION 2022 Forum*, AIAA 2022-3899. DOI: 10.2514/6.2022-3899.
- [48] P. Virtanen *et al.*, „SciPy 1.0: Fundamental Algorithms for Scientific Computing in Python“, *Nature Methods*, vol. 17, pp. 261–272, 2020. DOI: 10.1038/s41592-019-0686-2.
- [49] G. J. Székely, M. L. Rizzo and N. K. Bakirov, „Measuring and testing dependence by correlation of distances“, *The Annals of Statistics*, vol. 35, no. 6, pp. 2769–2794, 2007. DOI: 10.1214/009053607000000505.
- [50] M. D. Buhmann, *Radial Basis Functions: Theory and Implementations* (Cambridge Monographs on Applied and Computational Mathematics). Cambridge University Press, 2003.
- [51] M. Minsky and S. Papert, *Perceptrons*. Cambridge, MA: MIT Press, 1969.

- [52] R. H. R. Hahnloser, R. Sarpeshkar, M. A. Mahowald, R. J. Douglas and H. S. Seung, „Digital selection and analogue amplification coexist in a cortex-inspired silicon circuit“, *Nature*, vol. 405, no. 6789, pp. 947–951, Jun. 2000. DOI: 10.1038/35016072.
- [53] D. E. Rumelhart, G. E. Hinton and R. J. Williams, „Learning representations by back-propagating errors“, *nature*, vol. 323, no. 6088, pp. 533–536, 1986.
- [54] A. Paszke *et al.*, „Pytorch: An imperative style, high-performance deep learning library“, *CoRR*, vol. abs/1912.01703, 2019. [Online]. Available: <http://arxiv.org/abs/1912.01703>.
- [55] K. Hornik, M. Stinchcombe and H. White, „Multilayer feedforward networks are universal approximators“, *Neural Networks*, vol. 2, no. 5, pp. 359–366, 1989, ISSN: 0893-6080. DOI: [https://doi.org/10.1016/0893-6080\(89\)90020-8](https://doi.org/10.1016/0893-6080(89)90020-8).
- [56] North Atlantic Treaty Organization. Advisory Group for Aerospace Research and Development, *Addendum to AGARD Advisory Report No. 138: Experimental Data Base for Computers Program Assessment : Report of the Fluid Dynamics Panel Working Group 04* (AGARD advisory report). AGARD, 1984, ISBN: 9789283514756. [Online]. Available: <https://books.google.de/books?id=uURixwEACAAJ>.
- [57] P. Cook, M. Firmin, M. McDonald and R. A. Establishment, *Aerofoil RAE 2822: Pressure Distributions, and Boundary Layer and Wake Measurements* (Technical memorandum / Royal Aircraft Establishment). RAE, 1977. [Online]. Available: <https://books.google.de/books?id=rX8CSQAACAAJ>.
- [58] NASA, *Nparc alliance validation archive*. [Online]. Available: <https://www.grc.nasa.gov/WWW/wind/valid/raetaf/raetaf.html>.
- [59] S. Langer, „An initial investigation of solving rans equations in combination with two-equation turbulence models“, Institut für Aerodynamik und Strömungstechnik, Tech. Rep., Sep. 2019. [Online]. Available: <https://elib.dlr.de/129170/>.
- [60] M. Raffel, C. Willert, F. Scarano, C. J. Kähler, S. T. Wereley and J. Kompenhans, *Particle Image Velocimetry - A Practical Guide (3rd Edition)*. Springer Verlag, Apr. 2018, vol. 1, pp. 1–669. [Online]. Available: <https://elib.dlr.de/119724/>.
- [61] C. Klein, R. Engler, W. Sachs and U. Henne, „Application of pressure sensitive paint (psp) for determination of the pressure field and calculation of forces and moments of models in a wind tunnel“, *Experiments in Fluids*, vol. Volume 39, pp. 475–483, Aug. 2005. DOI: 10.1007/s00348-005-1010-8.
- [62] P. Hansen, „The l-curve and its use in the numerical treatment of inverse problems“, English, in *Invite Computational Inverse Problems in Electrocardiology*, Invite Computational Inverse Problems in Electrocardiology ; Conference date: 01-01-2000, WIT Press, 2000.
- [63] A. Ferrero, A. Iollo, F. Larocca, M. de Castro Monteiro Loffredo and E. Menegatti, „Field inversion and machine learning strategies for improving rans modelling in turbomachinery“, *14th European Conference on Turbomachinery Fluid Dynamics*

- and Thermodynamics*, 2021. [Online]. Available: <https://api.semanticscholar.org/CorpusID:240262370>.
- [64] F. Pedregosa *et al.*, „Scikit-learn: Machine learning in Python“, *Journal of Machine Learning Research*, vol. 12, pp. 2825–2830, 2011.
- [65] D. P. Kingma and J. Ba, *Adam: A method for stochastic optimization*, 2017. arXiv: 1412.6980 [cs.LG]. [Online]. Available: <https://arxiv.org/abs/1412.6980>.
- [66] T. Akiba, S. Sano, T. Yanase, T. Ohta and M. Koyama, „Optuna: A next-generation hyperparameter optimization framework“, in *Proceedings of the 25th ACM SIGKDD International Conference on Knowledge Discovery and Data Mining*, 2019.
- [67] J. Cooley and J. Tukey, „An algorithm for the machine calculation of complex fourier series“, *Mathematics of Computation*, vol. 19, no. 90, pp. 297–301, 1965.
- [68] W. H. Press, S. A. Teukolsky, W. T. Vetterling and B. P. Flannery, *Numerical Recipes 3rd Edition: The Art of Scientific Computing*, 3rd ed. USA: Cambridge University Press, 2007, ISBN: 0521880688.
- [69] J. Nitzsche, J. Otte, C. Kaiser and H. Hennings, „The effect of shock control bumps on the transonic flutter and buffeting characteristics of a typical wing section“, in *19th International Forum on Aeroelasticity and Structural Dynamics, IFASD 2022*, Jun. 2022.
- [70] P. Khurana, „Application and extension of a data-driven turbulence modeling method using machine learning“, M.S. thesis, Delft University of Technology, Nov. 2021. [Online]. Available: <https://elib.dlr.de/145184/>.
- [71] R. Thormann and M. Widhalm, „Linear frequency domain prediction of dynamic response data for viscous transonic flows“, *AIAA Journal*, vol. 51, no. 11, P. P. Friedmann, Ed., pp. 2540–2557, Sep. 2013. [Online]. Available: <https://elib.dlr.de/84359/>.

# List of Figures

2.1	Schematic overview of the most common RANS turbulence modeling approaches. . . . .	8
3.1	Workflow of FIML Classic as in [18]. . . . .	13
3.2	Application of turbulence model correction model within RANS solver for steady and unsteady simulations. . . . .	18
4.1	RAE 2822 airfoil geometry. . . . .	19
4.2	Mesh used in this study. Left: full domain. Right: zoom on the airfoil. . . . .	21
4.3	$c_l$ (left) and $c_d$ (right) over $\alpha$ for $M = 0.75$ $Re = 6.0 \cdot 10^6$ using the SA turbulence model. . . . .	21
4.4	$c_l$ (left) and $c_d$ (right) over $\alpha$ for $M = 0.75$ , $Re = 6.0 \cdot 10^6$ using the RSM turbulence model. . . . .	22
4.5	$c_l$ (left), $c_d$ (middle), and $c_{my}$ (right) over $\alpha$ for $M = 0.75$ $Re = 6.0 \cdot 10^6$ comparing SA and RSM. . . . .	23
4.6	$c_p$ -distribution on airfoil surface for $M = 0.75$ , $Re = 6.0 \cdot 10^6$ comparing SA and RSM. . . . .	23
4.7	Influence of the number of reference points used for field inversion on a numerical test case (baseline: SA; reference: RSM) with flow conditions $M = 0.75$ , $\alpha = 5.5^\circ$ , $Re = 6 \cdot 10^6$ , and regularisation $\lambda = 10^{-12}$ . 512 reference points correspond to 100%. . . . .	26
4.8	$c_p$ -distributions on airfoil surface comparing FIs with different numbers of reference points at $\alpha = 5.5^\circ$ . The legend of Subfigure 4.8c applies to all three cases. . . . .	27
4.9	$c_f$ -distributions on airfoil surface comparing SA (baseline) and RSM (reference) and FI result. . . . .	28
4.10	Synthetic test cases with baseline and reference solution from different angles of attack. . . . .	28
4.11	SA-production $P$ for SA at $\alpha = 5.5^\circ$ . . . . .	29
4.12	$c_p$ -distributions on airfoil surface comparing FI with reference points at rear only to baseline and reference solutions. . . . .	29
4.13	Selection criteria of regularisation at $\alpha = 2.5^\circ$ . . . . .	30
4.14	Selection criteria of regularisation at $\alpha = 4.0^\circ$ . . . . .	31
4.15	Inversion results at $\alpha = 1.5^\circ$ and $\alpha = 4.5^\circ$ . The $\beta$ -fields use the same colour range. For the close-ups, the colours are amplified. . . . .	32
4.16	$c_l$ (left), $c_d$ (middle), and $c_{my}$ (right) over $\alpha$ for $M = 0.75$ $Re = 6.0 \cdot 10^6$ comparing SA, RSM, and FI. . . . .	33
4.17	Number of occurrences of $\beta$ in the available data (left). Same figure with the logarithmic y-axis (right). . . . .	34
4.18	Visual representation and the result of area selection. . . . .	34
4.19	Number of occurrences of $\beta$ after reducing the values $0.99 < \beta < 1.01$ (left). Same figure with the logarithmic y-axis (right). . . . .	35
4.20	Distribution of $\eta_1$ before (left) and after (right) applying a logarithm. . . . .	36
4.21	Spearman's rank correlation coefficient between all features and the target. . . . .	38
4.22	Predicted versus true target values from training and test data for FCNN no. 1. . . . .	41
4.23	Predicted versus true target values from training and test data for FCNN no. 11. . . . .	43
4.24	$c_l$ (left), $c_d$ (middle), and $c_{my}$ (right) over $\alpha$ for $M = 0.75$ $Re = 6.0 \cdot 10^6$ comparing SA, RSM, FI, and SA augmented using the trained ML model. . . . .	45

4.25	Comparison of $c_p$ -distributions of SA, RSM, FI, and SA augmented using the trained ML model at $\alpha = 5.5^\circ$ . . . . .	45
4.26	Synthetic test cases with baseline and reference solution from different angles of attack. . . . .	46
4.27	Comparison of $\eta_{11}$ over $\beta$ for all samples vs. $\alpha = 5.5^\circ$ samples. . . . .	46
4.28	Excitation $\theta$ and resulting force coefficients $c_l$ , $c_{my}$ vs. number of excitation periods for $\bar{\alpha} = 3.0^\circ$ , $\hat{\theta} = 0.001^\circ$ , and $k = 0.3$ for the reference simulation. . . . .	48
4.29	Sliding FFT of $c_l/\alpha$ vs. number of excitation periods for $\bar{\alpha} = 3.0^\circ$ , $\hat{\theta} = 0.001^\circ$ , and $k = 0.3$ for the reference simulation. . . . .	49
4.30	Unsteady baseline and reference results in the frequency domain for $\bar{\alpha} = 3.0^\circ$ . . . . .	50
4.31	Unsteady portion of the lift coefficient normalised with pitch amplitude $(c_l - \bar{c}_l)/\hat{\theta}$ over pitch angle normalised with pitch angle $\theta/\hat{\theta}$ for SA and RSM at $\bar{\alpha} = 3.0^\circ$ , $k = 0.3$ , and two different amplitudes. . . . .	50
4.32	Unsteady results at $\bar{\alpha} = 1.5^\circ$ for $c_l$ . All plots use the same colour scheme. Figure A.6 in the Appendix A presents the corresponding results for $c_{my}$ . . . . .	53
4.33	Unsteady results at $\bar{\alpha} = 3.0^\circ$ for $c_l$ . All plots use the same colour scheme. Figure A.7 in the Appendix A presents the corresponding results for $c_{my}$ . . . . .	54
4.34	Influence of unsteady order scheme and the number of iterations to evaluate the CAUCHY convergence for simulations without excitation applying an ML-based steady $\beta$ -field. Note that the axes use different scales. . . . .	55
4.35	Influence of physical time step size (in comparison to $\Delta t_{\text{physical}}$ for $k = 0.3$ in 4.8) and the number of iterations to evaluate the CAUCHY convergence for simulations without excitation applying the trained ML model. Note that the axes use different scales. . . . .	56
4.36	Unsteady results at $\bar{\alpha} = 4.5^\circ$ for $c_l$ . All plots use the same colour scheme. Figure A.8 in the Appendix A presents the corresponding results for $c_{my}$ . . . . .	57
4.37	$c_l$ (left), and $dc_l/d\alpha$ (right) over $\alpha$ for $M = 0.75$ $Re = 6.0 \cdot 10^6$ comparing SA, RSM, FI, and SA augmented using the trained ML model. Figure A.9 in the Appendix A presents the corresponding results for $c_{my}$ . . . . .	58
5.1	$c_p$ -distributions of averaged experimental data as well as standard deviation, minima, maxima. . . . .	61
5.2	Nearest neighbours of experimental data in CFD mesh. . . . .	62
5.3	$c_{z,\text{inertial}}$ respectively $c_l$ vs. $\alpha$ comparing SA simulations and experimental data. . . . .	63
5.4	Comparison of $c_p$ -distributions of experimental data and SA simulation. . . . .	64
5.5	$c_{z,\text{inertial}}$ vs. $\alpha$ comparing SA simulations, experimental data, and FI result. . . . .	65
5.6	$M = 0.73$ , $\alpha = 1.41^\circ$ , and $Re = 6.45 \cdot 10^6$ . . . . .	65
5.7	$c_{z,\text{inertial}}$ vs. $\alpha$ comparing SA simulations, experimental data, FI result, and augmented SA simulation using the ML model trained on the numerical test case. . . . .	66
5.8	Experimental FCNN case 1. . . . .	67
5.9	Experimental FCNN case 2. . . . .	67
5.10	Comparison of $c_p$ -distributions of experimental data, SA simulation, FI, and ML model case 2. . . . .	68
5.11	Hysteresis plot due to pitch excitation for experimental test case at $\alpha = 4.16$ , $k = 0.3$ , and $\hat{\alpha} = 0.001^\circ$ . . . . .	69
A.1	Pearson correlation coefficient for between all features and the target. . . . .	85
A.2	Distance correlation coefficient between all features and the target. . . . .	86
A.3	Comparison of $\eta_7$ over $\beta$ for all samples vs. $\alpha = 5.5^\circ$ samples. . . . .	86
A.4	$c_p$ field solutions at $\alpha = 1.5^\circ$ . Note that each plot uses a different color scale, as the ranges vary. . . . .	88
A.5	$c_p$ field solutions at $\alpha = 4.5^\circ$ . Note that each plot uses a different color scale, as the ranges vary. . . . .	89
A.6	Unsteady results at $\bar{\alpha} = 1.5^\circ$ for $c_{my}$ . All plots use the same colour scheme. . . . .	90
A.7	Unsteady results at $\bar{\alpha} = 3.0^\circ$ for $c_{my}$ . All plots use the same colour scheme. . . . .	91

---

A.8	Unsteady results at $\bar{\alpha} = 4.5^\circ$ for $c_{my}$ . All plots use the same colour scheme.	92
A.9	$c_{my}$ (left), and $dc_{my}/d\alpha$ (right) over $\alpha$ for $M = 0.75$ $Re = 6.0 \cdot 10^6$ comparing SA, RSM, FI, and SA augmented using the trained ML model. . . . .	92
A.10	Survey of available experimental data points. . . . .	93
A.11	Schematic reasoning for calculation of $c_{z,inertial}$ . . . . .	93
A.12	Selection criteria of regularization at $M = 0.73$ , $\alpha = 1.41^\circ$ , and $Re = 6.45 \cdot 10^6$ .	94
A.13	Selection criteria of regularization at $M = 0.72$ , $\alpha = 4.70^\circ$ , and $Re = 6.36 \cdot 10^6$ .	95
A.14	Comparison of $c_p$ -distributions of experimental data, SA simulation, and FI.	96
A.15	Comparison of $c_p$ -distributions of experimental data, SA simulation, FI, and ML model from the numerical test case. . . . .	97
A.16	Comparison of $c_p$ -distributions of experimental data, SA simulation, FI, and ML model case 1. . . . .	98
A.17	$\beta$ -fields at $M = 0.72$ , $\alpha = 3.29^\circ$ , and $Re = 6.42 \cdot 10^6$ . . . . .	99

# List of Tables

4.1	Numbers of investigated reference points . . . . .	25
4.2	Selected values for $\lambda$ . The letters in the last row denote selection by <u>L</u> -curve criterion (L) or <u>s</u> election by comparing $c_p$ -distributions (S). . . . .	31
4.3	Features to be investigated. Row GALILEAN invariance shows whether this requirement is satisfied. The row log shows if a logarithm should be applied. Removed samples show the number of samples removed due to the application of the logarithm. . . . .	37
4.4	Resulting scores for presented RBF model. . . . .	40
4.5	Influence of feature selection and dataset on generic FCNN. <i>small</i> : training data are $\alpha_{\text{train, small}}$ . <i>large</i> : training data are $\alpha_{\text{train, large}}$ . <i>no reduction</i> : dataset is not altered. <i>area</i> : area selection is applied. <i>x%</i> : only $x\%$ of the samples with $0.99 < \beta < 1.01$ are included. <i>sep. val.</i> : train and validation data are not split randomly (70%/30%), but $\alpha = \{0.5^\circ, 2.0^\circ, 4.0^\circ\}$ are used for validation. . . . .	42
4.6	Comparison of training and test metrics of HPO result and previous best FCNN model. . . . .	44
4.7	Combinations of reduced frequency and pitching amplitude considered for the unsteady simulations. . . . .	47
4.8	Time steps per pitching period and physical time step size $\Delta t_{\text{physical}}$ at each reduced frequency $k$ . . . . .	48
4.9	Advantages and disadvantages of the different models . . . . .	52
A.1	Tested and resulting hyperparameters. . . . .	87
A.2	Averaged free-stream conditions including minima, maxima and standard deviation . . . . .	87

# Chapter A

## Appendix

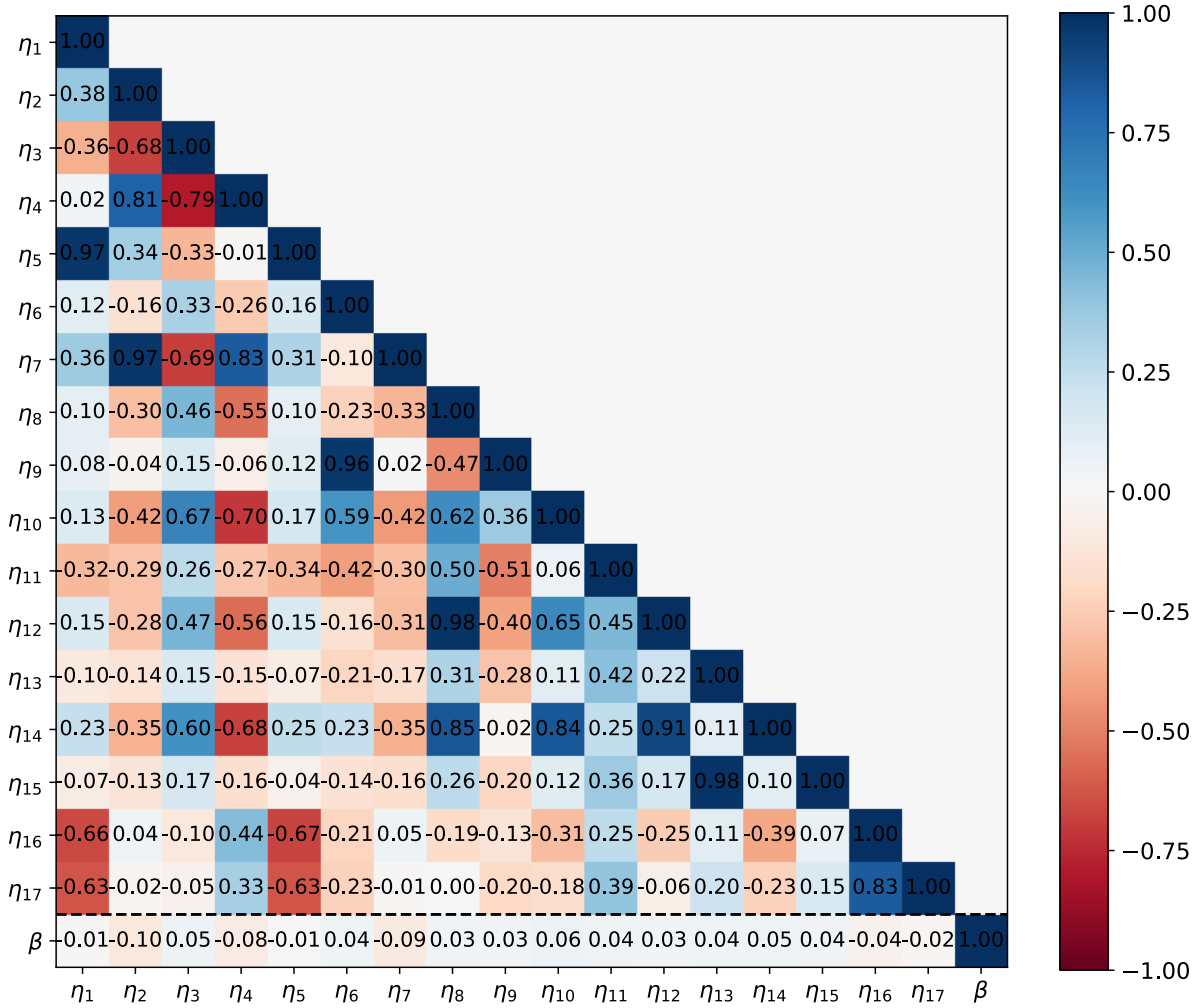


**Figure A.1:** Pearson correlation coefficient for between all features and the target.

Given static pressure  $p$ , isentropic expansion factor  $\kappa$ , and MACH number  $M$ ,  $c_p$  can be calculated as follows:

$$c_p = \frac{\left( \frac{1+0.5(\kappa-1)M^2}{1+0.5(\kappa-1)p^2} \right)^{\left( \frac{\kappa}{\kappa-1} \right)} - 1}{0.5\kappa M^2} \quad (\text{A.1})$$

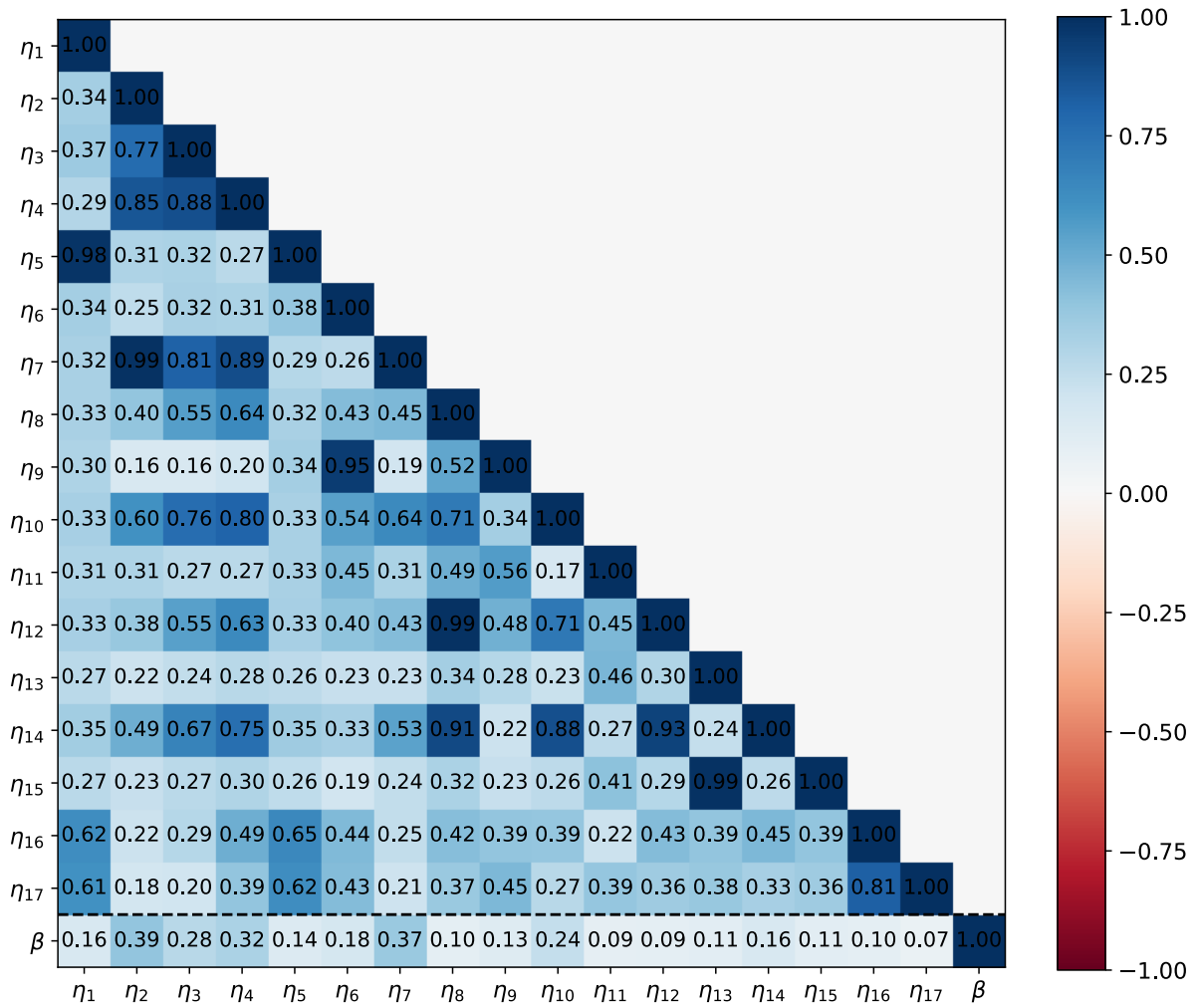


Figure A.2: Distance correlation coefficient between all features and the target.

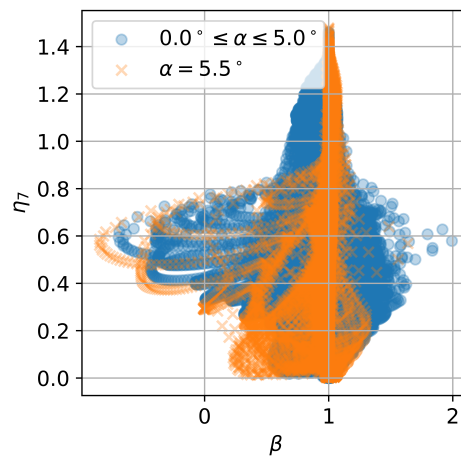


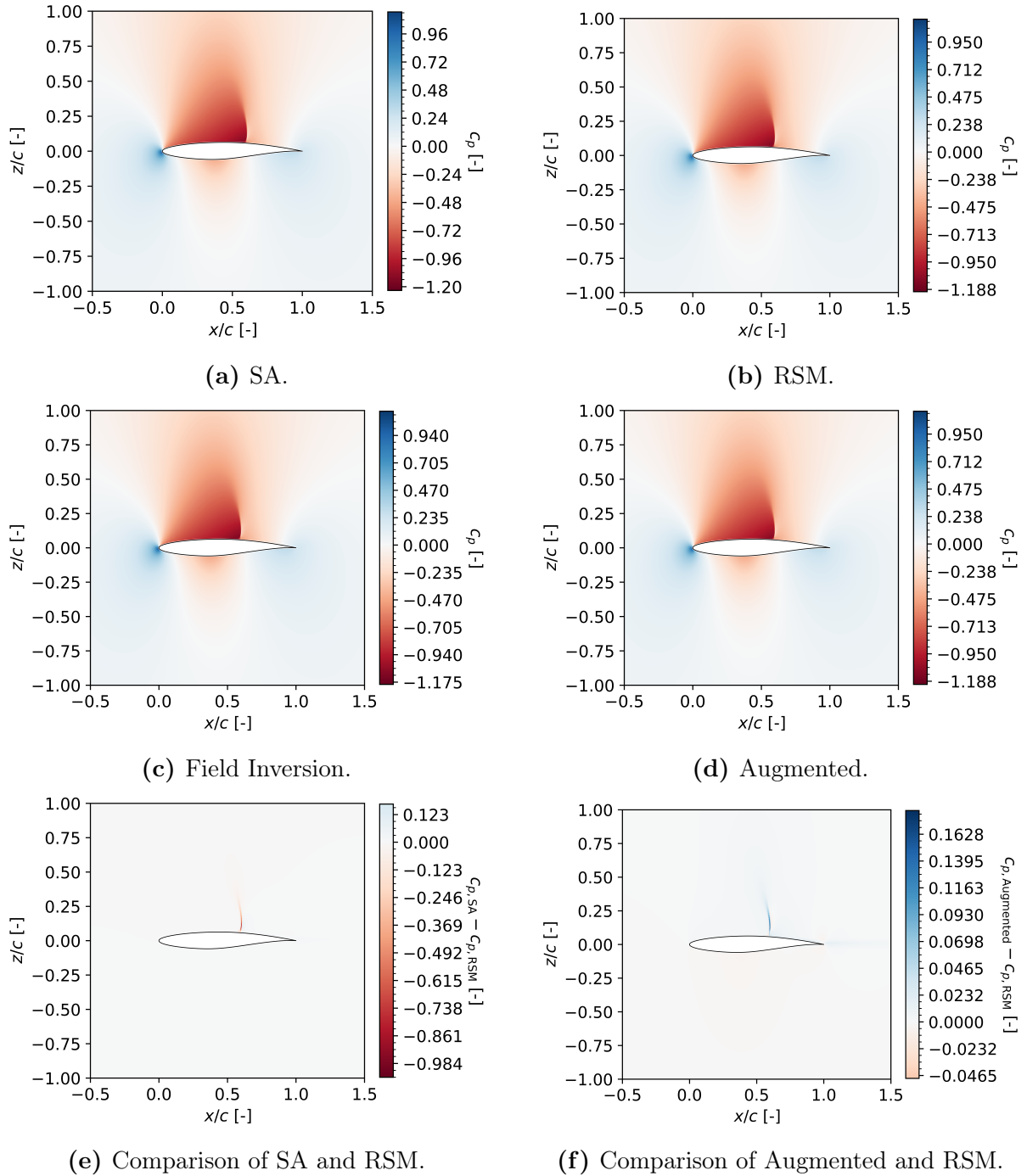
Figure A.3: Comparison of  $\eta_7$  over  $\beta$  for all samples vs.  $\alpha = 5.5^\circ$  samples.

Hyperparameter	Sampling space	Range	HPO result
Number of neurons in the first hidden layer	Integer from set	[32, 64, 128, 256, 512, 1024]	1024
Maximum number of hidden layers	Integer from range	[2, 8]	4
Shrinkage factor	Float from range	[0.2, 1.8]	1.427
Dropout rate	Float from logarithmic range	0.01, 0.4	0.130
Learning rate	Float from range	$[1 \cdot 10^{-5}, 1 \cdot 10^{-2}]$	$5.02 \cdot 10^{-4}$
Gamma	Float from logarithmic range	[0.1, 1]	0.432
Milestone factor	Integer from range	[10, 1000]	112
Batch size	Integer from set	[256, 512, 1024, 2048, 4096, 8192]	256

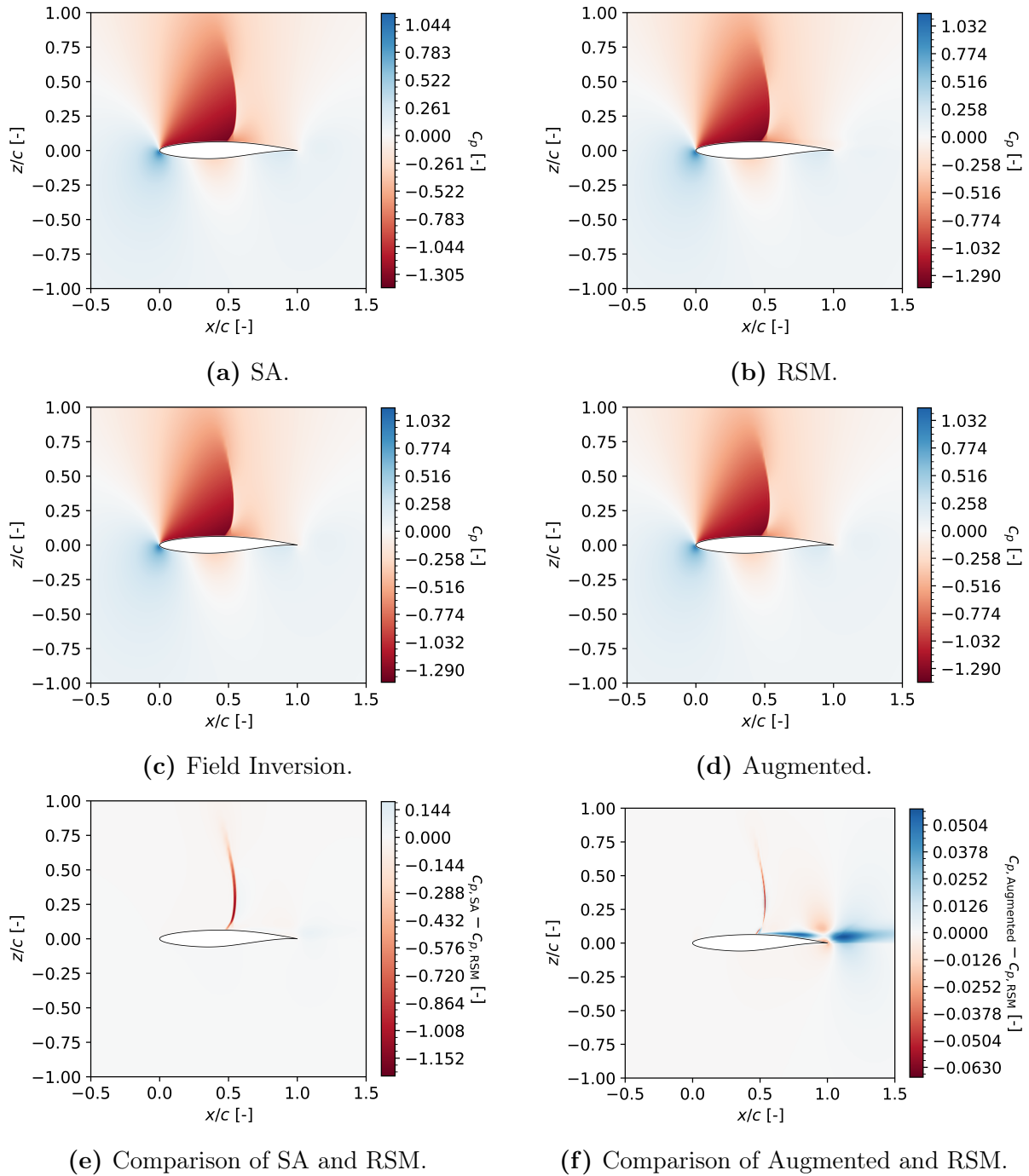
**Table A.1:** Tested and resulting hyperparameters.

$\alpha$ [deg]				M [-]				Re [-]			
Mean	Std $\cdot 10^3$	Min	Max	Mean	Std $\cdot 10^4$	Min	Max	Mean $\cdot 10^{-6}$	Std $\cdot 10^{-3}$	Min $\cdot 10^{-6}$	Max $\cdot 10^{-6}$
-1.13	1.29	-1.13	-1.12	0.74	3.97	0.73	0.74	6.47	9.52	6.46	6.49
-0.83	1.64	-0.83	-0.83	0.74	5.69	0.73	0.74	6.47	3.46	6.46	6.48
-0.53	2.14	-0.53	-0.53	0.74	6.31	0.73	0.74	6.45	7.78	6.43	6.46
0.07	2.47	0.06	0.07	0.74	9.87	0.73	0.74	6.49	15.15	6.46	6.51
0.71	4.04	0.71	0.72	0.74	13.43	0.73	0.74	6.44	23.23	6.41	6.49
1.41	3.08	1.41	1.42	0.73	7.34	0.73	0.74	6.45	18.41	6.42	6.47
2.20	2.10	2.19	2.20	0.73	7.72	0.73	0.73	6.40	25.05	6.37	6.44
2.62	1.26	2.62	2.62	0.73	3.87	0.72	0.73	6.40	14.78	6.38	6.42
3.10	6.64	3.09	3.11	0.72	14.59	0.72	0.73	6.37	20.25	6.35	6.40
3.29	1.59	3.29	3.30	0.72	4.33	0.72	0.72	6.42	5.30	6.41	6.43
3.50	3.11	3.49	3.50	0.72	4.63	0.72	0.72	6.44	14.43	6.41	6.47
3.71	3.45	3.71	3.72	0.72	5.82	0.72	0.72	6.41	6.78	6.40	6.42
4.16	4.78	4.15	4.17	0.72	5.41	0.72	0.72	6.40	8.40	6.38	6.41
4.70	2.05	4.70	4.70	0.72	4.63	0.72	0.72	6.36	10.00	6.34	6.38
5.20	2.40	5.20	5.21	0.72	5.47	0.72	0.72	6.33	6.94	6.32	6.34
5.74	4.60	5.73	5.74	0.72	8.05	0.72	0.72	6.32	19.07	6.30	6.35

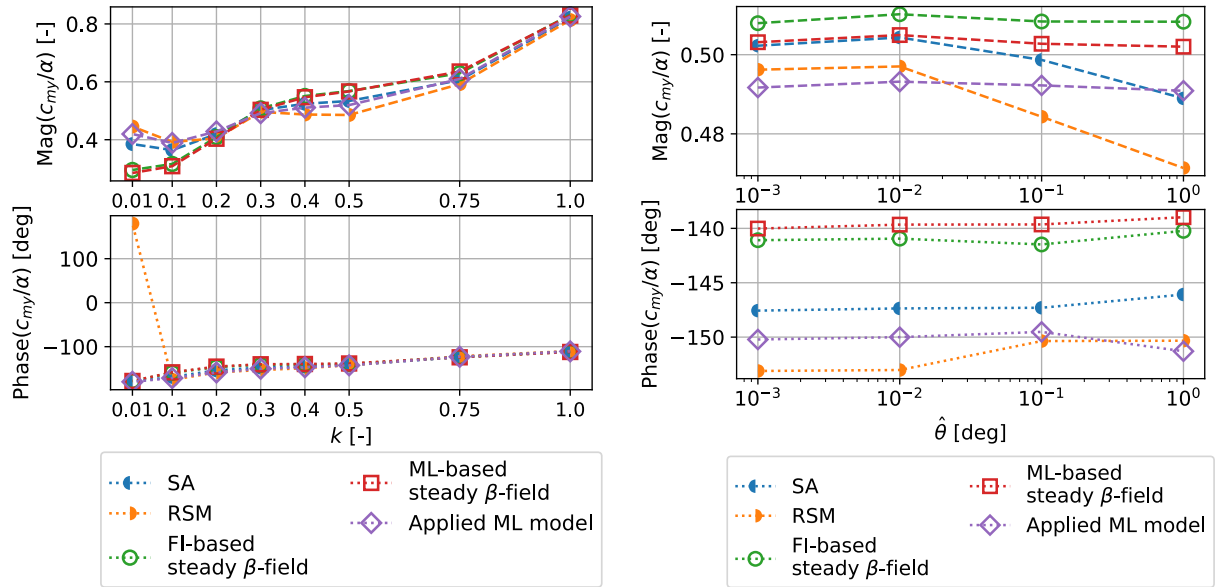
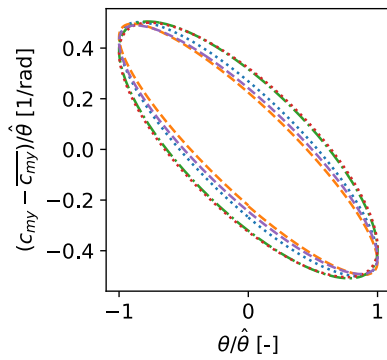
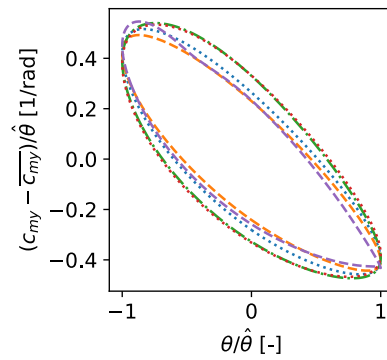
**Table A.2:** Averaged free-stream conditions including minima, maxima and standard deviation

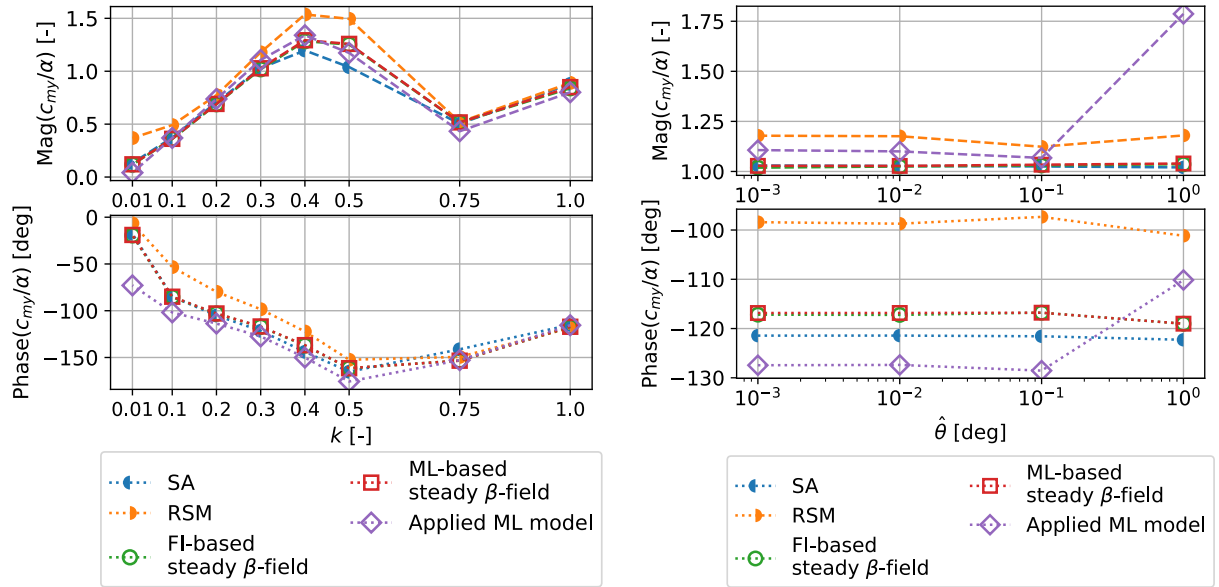
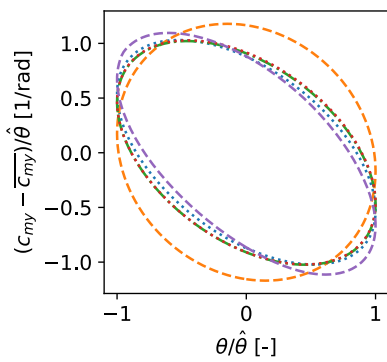
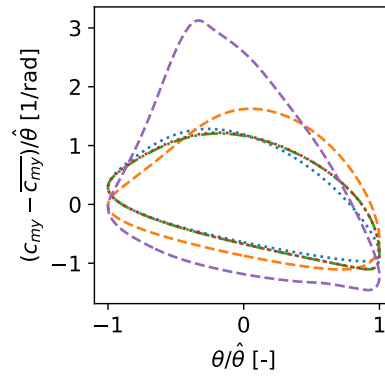


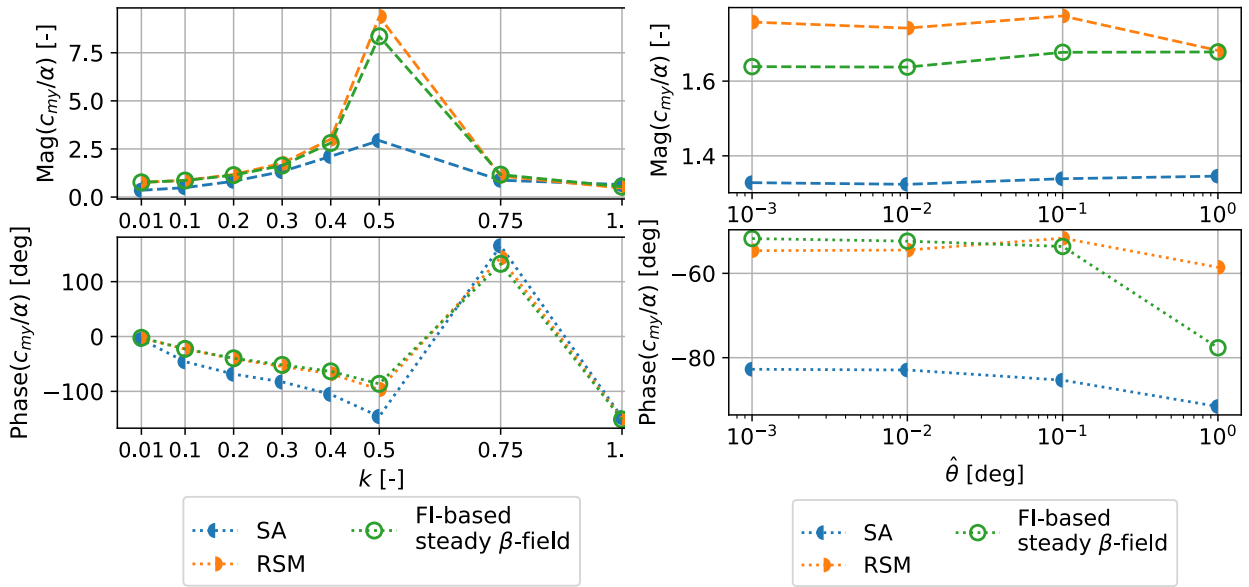
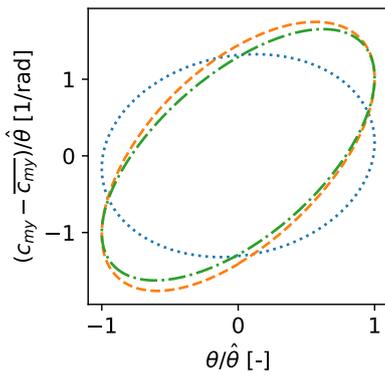
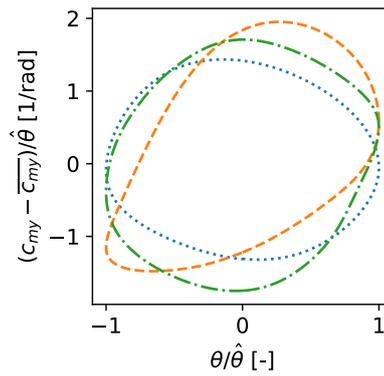
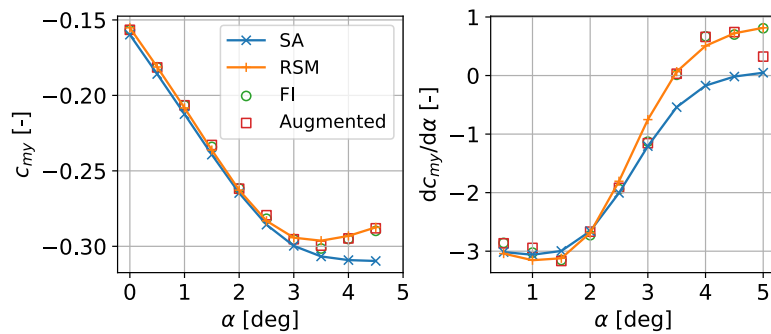
**Figure A.4:**  $c_p$  field solutions at  $\alpha = 1.5^\circ$ . Note that each plot uses a different color scale, as the ranges vary.



**Figure A.5:**  $c_p$  field solutions at  $\alpha = 4.5^\circ$ . Note that each plot uses a different color scale, as the ranges vary.

(a) BODE plot with  $\hat{\theta} = 0.001^\circ$  fixed.(b) Magnitude and phase vs. amplitude with  $k = 0.3$  fixed.(c) Hysteresis plot at  $k = 0.3$ ,  $\hat{\theta} = 0.001^\circ$ .(d) Hysteresis plot at  $k = 0.3$ ,  $\hat{\theta} = 1^\circ$ .**Figure A.6:** Unsteady results at  $\bar{\alpha} = 1.5^\circ$  for  $c_{my}$ . All plots use the same colour scheme.

(a) BODE plot with  $\hat{\theta} = 0.001^\circ$  fixed.(b) Magnitude and phase vs. amplitude with  $k = 0.3$  fixed.(c) Hysteresis plot at  $k = 0.3, \hat{\theta} = 0.001^\circ$ .(d) Hysteresis plot at  $k = 0.3, \hat{\theta} = 1^\circ$ .**Figure A.7:** Unsteady results at  $\bar{\alpha} = 3.0^\circ$  for  $c_{my}$ . All plots use the same colour scheme.

(a) BODE plot with  $\hat{\theta} = 0.001^\circ$  fixed.(b) Magnitude and phase vs. amplitude with  $k = 0.3$  fixed.(c) Hysteresis plot at  $k = 0.3$ ,  $\hat{\theta} = 0.001^\circ$ .(d) Hysteresis plot at  $k = 0.3$ ,  $\hat{\theta} = 1^\circ$ .**Figure A.8:** Unsteady results at  $\bar{\alpha} = 4.5^\circ$  for  $c_{my}$ . All plots use the same colour scheme.**Figure A.9:**  $c_{my}$  (left), and  $dc_{my}/d\alpha$  (right) over  $\alpha$  for  $M = 0.75 Re = 6.0 \cdot 10^6$  comparing SA, RSM, FI, and SA augmented using the trained ML model.

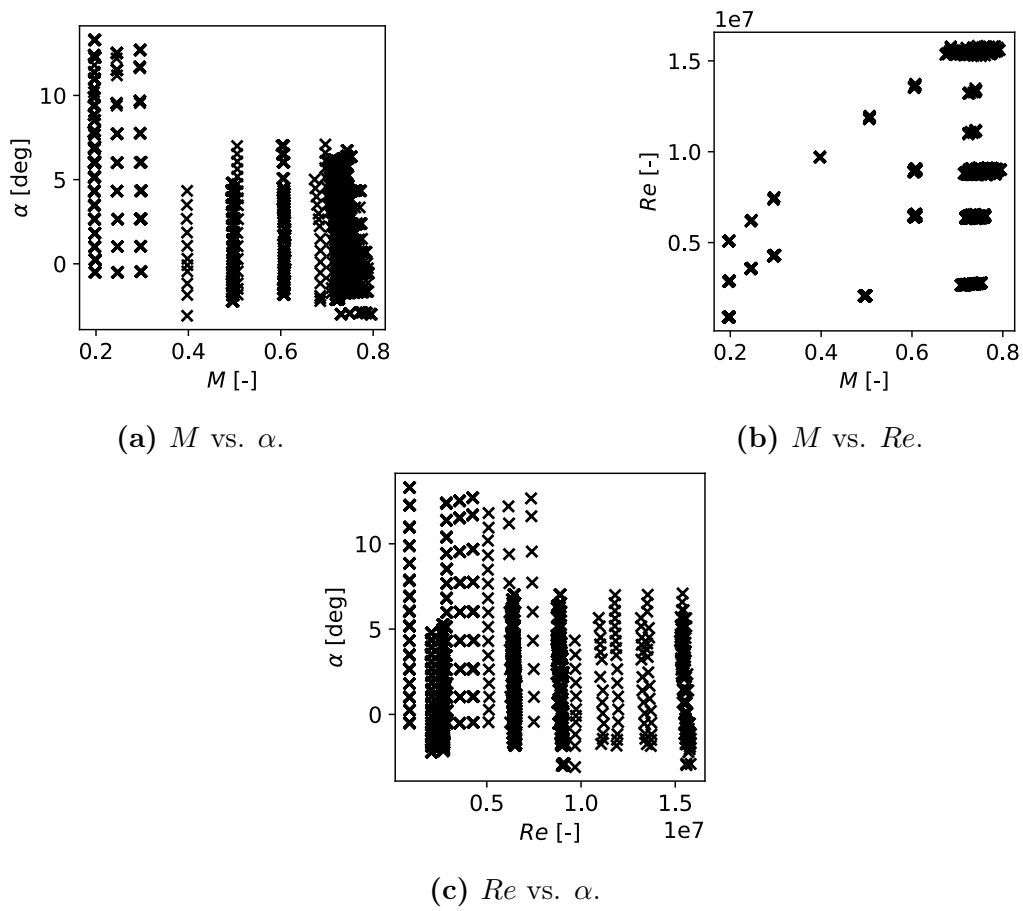


Figure A.10: Survey of available experimental data points.

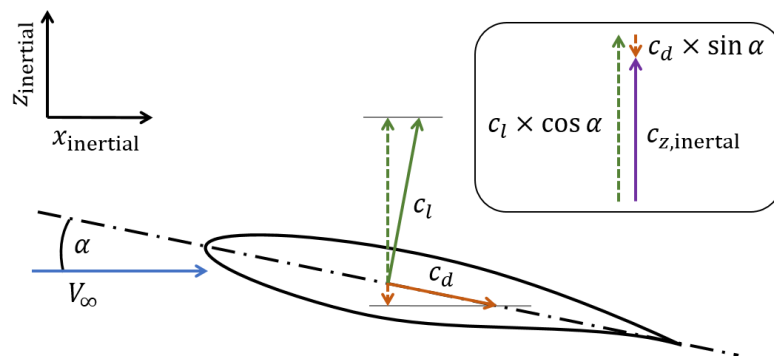
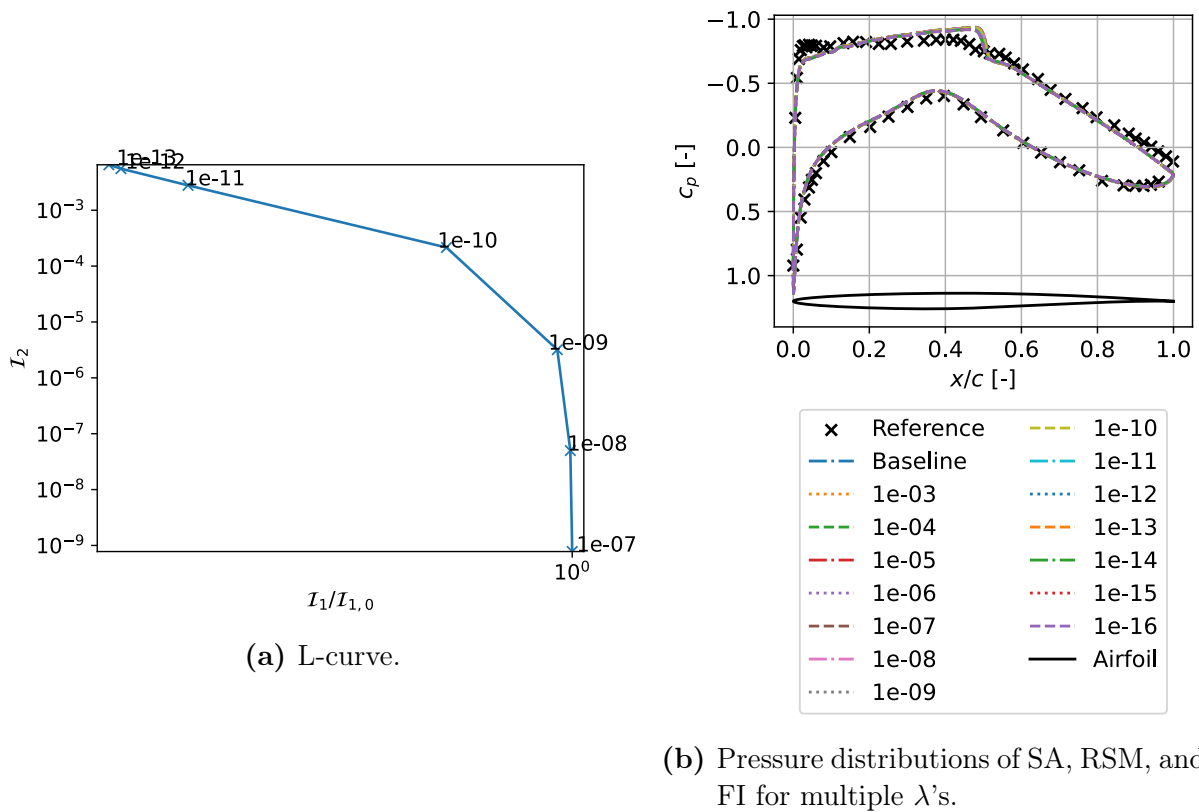
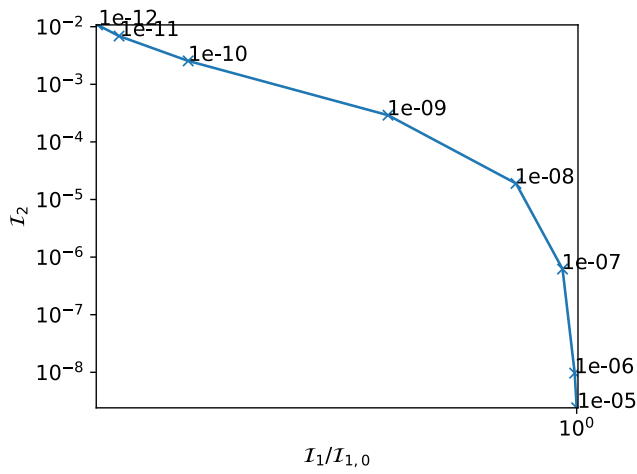


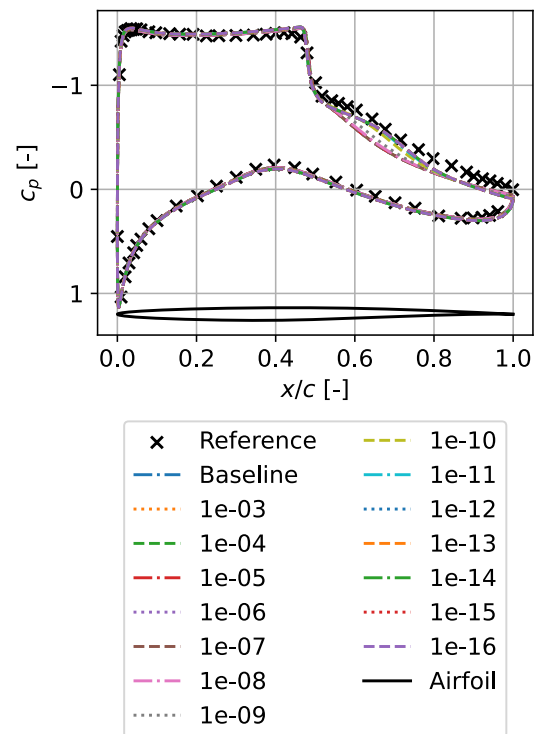
Figure A.11: Schematic reasoning for calculation of  $c_{z,inertial}$  based on  $c_l$  and  $c_d$ .



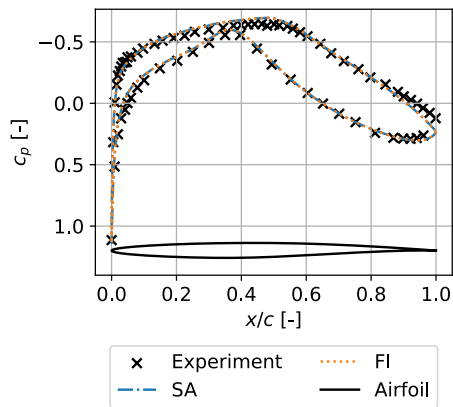
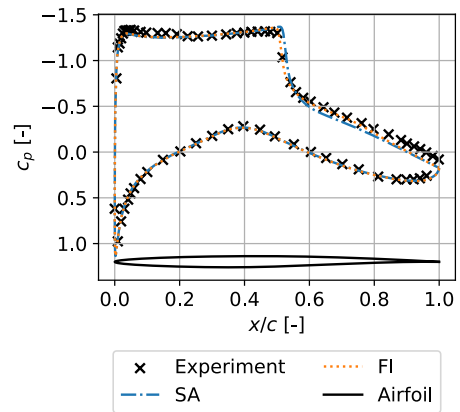
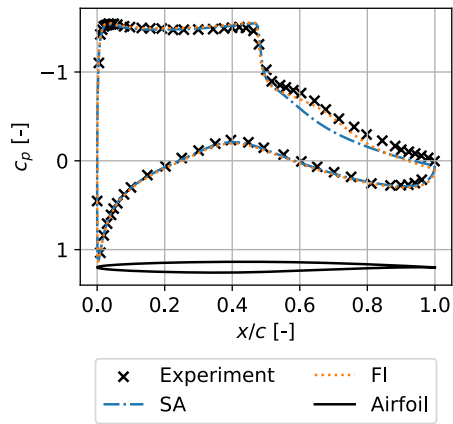
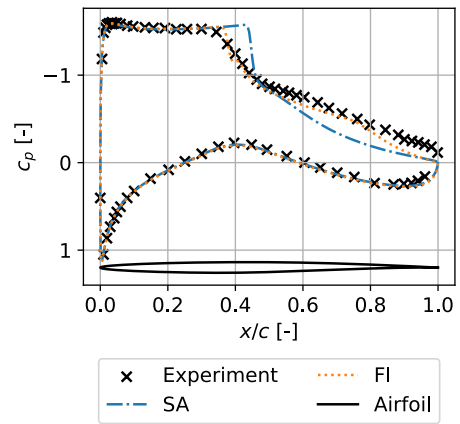
**Figure A.12:** Selection criteria of regularization at  $M = 0.73$ ,  $\alpha = 1.41^\circ$ , and  $Re = 6.45 \cdot 10^6$ .



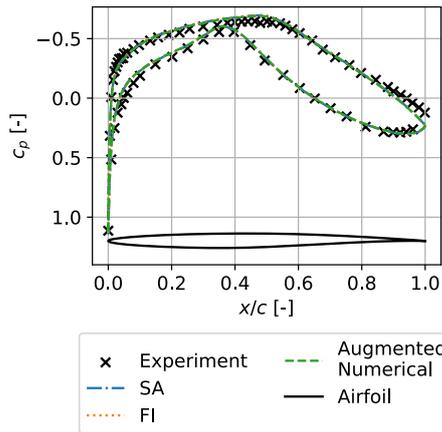
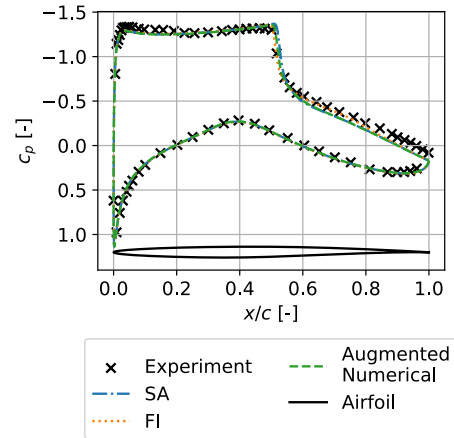
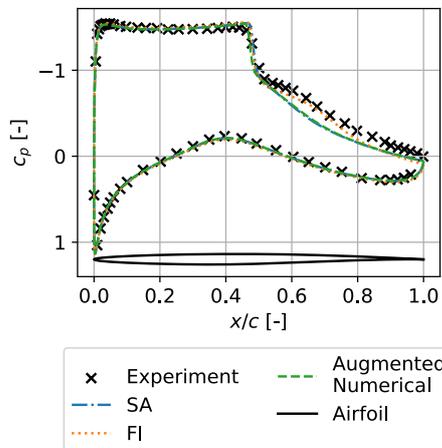
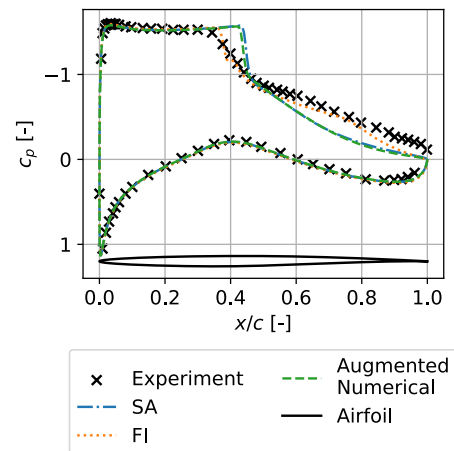
(a) L-curve.

(b) Pressure distributions of SA, RSM, and FI for multiple  $\lambda$ 's.

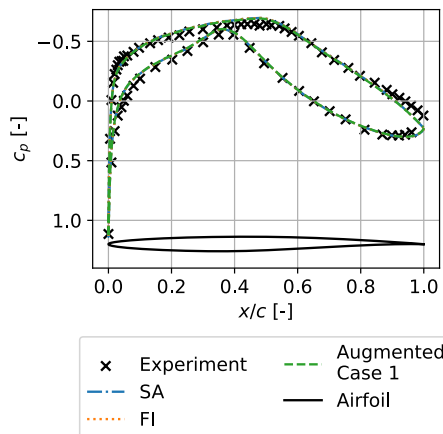
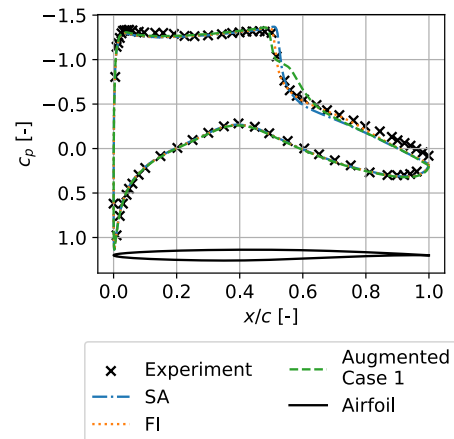
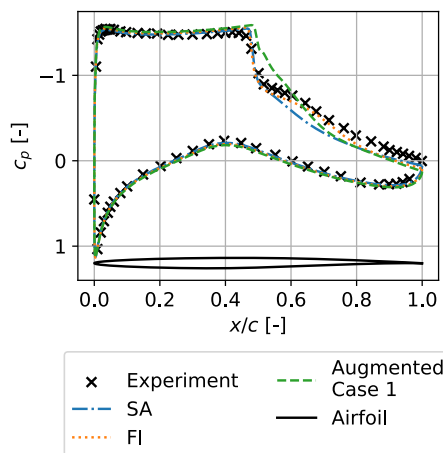
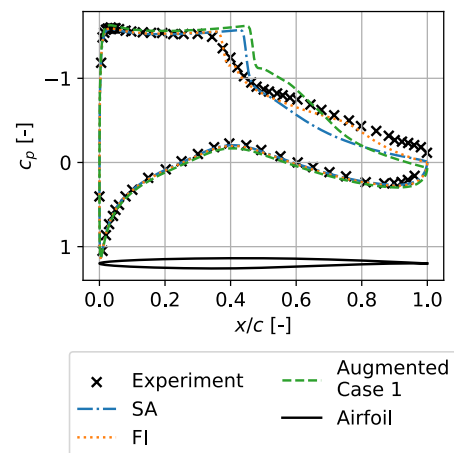
**Figure A.13:** Selection criteria of regularization at  $M = 0.72$ ,  $\alpha = 4.70^\circ$ , and  $Re = 6.36 \cdot 10^6$ .

(a)  $M = 0.74$ ,  $\alpha = 0.07^\circ$ , and  $Re = 6.49 \cdot 10^6$ .(b)  $M = 0.72$ ,  $\alpha = 3.29^\circ$ , and  $Re = 6.42 \cdot 10^6$ .(c)  $M = 0.72$ ,  $\alpha = 4.70^\circ$ , and  $Re = 6.36 \cdot 10^6$ .(d)  $M = 0.72$ ,  $\alpha = 5.20^\circ$ , and  $Re = 6.33 \cdot 10^6$ .

**Figure A.14:** Comparison of  $c_p$ -distributions of experimental data, SA simulation, and FI.

(a)  $M = 0.74$ ,  $\alpha = 0.07^\circ$ , and  $Re = 6.49 \cdot 10^6$ .(b)  $M = 0.72$ ,  $\alpha = 3.29^\circ$ , and  $Re = 6.42 \cdot 10^6$ .(c)  $M = 0.72$ ,  $\alpha = 4.70^\circ$ , and  $Re = 6.36 \cdot 10^6$ .(d)  $M = 0.72$ ,  $\alpha = 5.20^\circ$ , and  $Re = 6.33 \cdot 10^6$ .

**Figure A.15:** Comparison of  $c_p$ -distributions of experimental data, SA simulation, FI, and ML model from the numerical test case.

(a)  $M = 0.74$ ,  $\alpha = 0.07^\circ$ , and  $Re = 6.49 \cdot 10^6$ .(b)  $M = 0.72$ ,  $\alpha = 3.29^\circ$ , and  $Re = 6.42 \cdot 10^6$ .(c)  $M = 0.72$ ,  $\alpha = 4.70^\circ$ , and  $Re = 6.36 \cdot 10^6$ .(d)  $M = 0.72$ ,  $\alpha = 5.20^\circ$ , and  $Re = 6.33 \cdot 10^6$ .

**Figure A.16:** Comparison of  $c_p$ -distributions of experimental data, SA simulation, FI, and ML model case 1.

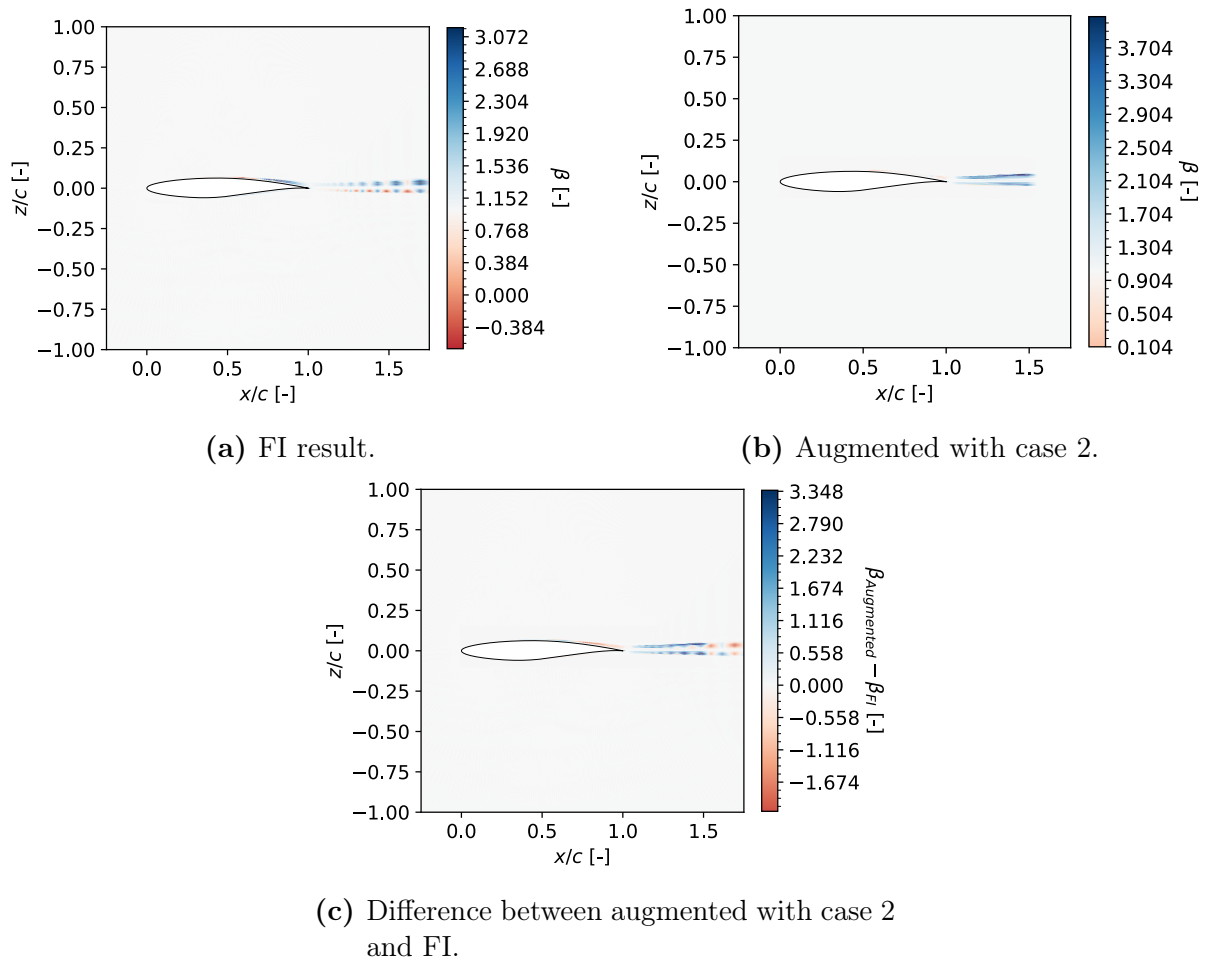


**Figure A.17:**  $\beta$ -fields at  $M = 0.72$ ,  $\alpha = 3.29^\circ$ , and  $Re = 6.42 \cdot 10^6$ .